Waveguide Integrated Optoelectronics Using Two-Dimensional Materials

A DISSERTATION
SUBMITTED TO THE FACULTY OF THE GRADUATE SCHOOL
OF THE UNIVERSITY OF MINNESOTA
BY

NATHAN YOUNGBLOOD

IN PARTIAL FULFILLMENT OF THE REQUIREMENTS
FOR THE DEGREE OF
DOCTOR OF PHILOSOPHY

MO LI

November, 2016

© NATHAN YOUNGBLOOD 2016
ALL RIGHTS RESERVED

Acknowledgements

While I am able to claim the work presented in this dissertation as my own, I am quick to acknowledge that none of it would exist without the support of my friends, family, and colleagues. This section is written in gratitude to the many people that have taught and encouraged me over the last five years.

First of all, it has been a pleasure to work under the guidance and mentorship of Dr. Mo Li. He has been very influential during my formative years as a graduate student and has invested much time and energy into my journey from a student to an independent researcher. I have learned which questions to ask and what problems are worth pursuing due to his expert guidance. I am truly thankful to have had him as an advisor.

I would also like to thank my group members for their help and collaboration. It has been a great experience to learn from all of them and exchange knowledge and ideas. Specifically, I'd like to thank Dr. Huan Li and Li He for helping me understand various experimental techniques and theory. Their kindness and patience has been an example that I strive for (and often fail at!) in my interactions with others. I owe much to them.

I would like to thank Dr. Steven Koester, Dr. Joseph Talghader, and Dr. Russell Holmes for taking time to review this dissertation and serve on my committee. I would like to give extra thanks to Dr. Koester for all the wisdom and

understanding I have gained from my interactions with him (especially in regards to semiconductor devices of which I had very little knowledge prior).

I would be remiss if I did not thank the NFC cleanroom staff for their amazing advice and assistance during my time at UMN. I have never worked with more responsive and helpful support staff and I owe most of my success to their fabrication expertise. I would specifically like to thank Bryan Cord, Kevin Roberts, Lage von Dissen, Robert Amundson, Terry Brough, Mark Fisher, Bashir Jama, Glenn Kuschke, and Tony Whipple all of whom have given help and advice in various forms which has meant the difference between a failed and a successful device.

I cannot thank my mother and father enough for providing a high quality education and upbringing which has carried me thus far. I would never have had the ambition to finish a PhD without their love and support all the years prior.

Finally, I'd like to thank my wife for her support throughout this lengthy (and sometimes stressful) portion of my life. She has always understood me better than I understand myself and has been a great companion through the joys and trials of life.

Dedication

To April, best of wives and best of women.

Abstract

The focus of this dissertation is the integration of 2D materials on a silicon photonics platform for optoelectronic applications. The current state of waveguide integrated photodetectors and modulators is reviewed and provides a context for the work detailed in the following chapters. The first dual-function graphene photodetector and modulator is demonstrated in a simple geometry that allows simultaneous use of both functionalities. Next, the first waveguide integrated black phosphorus photodetector is demonstrated with superior dark current to its graphene counterparts. Operation speeds six orders of magnitude higher than any previous black phosphorus detector is demonstrated together with a clear understanding of the photocurrent mechanisms that dominate the device. Finally, the nonlinear response of black phosphorus was used to investigate the intrinsic speed of a photodetector. Subsequent observation of third-harmonic generation led to characterization of $\chi^{(3)}$ in black phosphorus for the first time.

Contents

Acknowledgements **i**

Dedication **iii**

Abstract **iv**

List of Tables **ix**

List of Figures **x**

1 Introduction **1**

1.1 Motivation 1

1.1.1 The Growing Need for Silicon Photonics 1

1.1.2 Motivation for Two-Dimensional Materials 3

1.2 Photodetection 5

1.2.1 Graphene Photodetectors 5

1.2.2 Black Phosphorus Photodetectors 9

1.3 Modulation 13

1.3.1 Graphene Modulators 13

1.3.2 Black Phosphorus Modulators 17

1.4 Dissertation Outline 18

2 Dual-Function Graphene Photodetector and Modulator 20

2.1 Photocurrent mechanisms in graphene 20

2.1.1 Photovoltaic effect 21

2.1.2 Bolometric effect 22

2.1.3 Photo-thermoelectric effect 24

2.2 Optical modulation in graphene 27

2.2.1 Electrostatically tuning graphene's Fermi level 27

2.2.2 Theory of optical absorption in graphene 32

2.3 Motivation 37

2.4 Device design 38

2.4.1 Photonics layer 38

2.4.2 Electronics layer 43

2.5 Results 46

2.5.1 Modulation 46

2.5.2 Photodetection 49

2.5.3 Simultaneous Operation 53

2.6 Conclusion 55

3 Black Phosphorus Photodetector 57

3.1 Introduction 58

3.2 Device fabrication 60

3.3 Results 67

3.4 Discussion 75

3.5 Conclusion 77

4 Nonlinear Optical Response of Black Phosphorus 79

4.1 Introduction 80

4.2 Device design 80
4.3 Methodology and experimental setup 82
4.4 Results 84
4.5 Third-harmonic generation in black phosphorus thin films 89
4.6 Theory of Third-Harmonic Generation in Thin Films 91
4.7 Derivation of third-harmonic generation in a lossy medium 92
4.8 Sample Preparation and Experimental Setup 97
4.9 Results 98
4.10 Discussion 106
4.11 Conclusion 110

5 Concluding Remarks 111
5.1 Summary 111
5.2 Future directions for 2D optoelectronics 112

References 115

Appendix A. Fabrication Techniques 140
A.1 Waveguide planarization 140
A.2 CVD graphene transfer with PMMA 143
A.3 Aligned exfoliation of 2D materials 145
A.3.1 Scotch tape exfoliation 145
A.3.2 Wet transfer method 146
A.3.3 Dry transfer method 150

Appendix B. Experimental Techniques 152
B.1 Phase Scrambler for Ultrafast Setup 152
B.1.1 Introduction 152

B.1.2 Theory 155
B.1.3 Results 160
B.1.4 Conclusion 161

Appendix C. Classical Derivation of the Nonlinear Susceptibility for a Centrosymmetric Material 162

List of Tables

3.1 Figures of merit for various BP photodectors 77
4.1 Reported values of $\chi^{(3)}$ for various 2D materials 109
A.1 Recipe for annealing evaporated oxides with RTA 141

List of Figures

1.1 Light-matter interaction with 2D materials 4
1.2 Graphene photodetectors 7
1.3 Black phosphorus photodetectors 10
1.4 Graphene modulators 16
2.1 Photovoltaic illustration 22
2.2 Bolometric illustration 23
2.3 Photo-thermoelectric illustration 26
2.4 Optical modulation in graphene 28
2.5 Electrostatic gating illustration 29
2.6 Effect of quantum capacitance in graphene 32
2.7 Graphene optical conductivity 34
2.8 Modulating graphene with V_G 36
2.9 Simulated waveguide mode profiles 39
2.10 Mach-Zenhder interferometer spectra and illustration 41
2.11 SEM and optical microscope images of graphene modulator/detector 44
2.12 Band diagram at zero bias 46
2.13 Gate tuned optical absorption and optical modulation 47
2.14 Gate tuned photodetection 51
2.15 Gate and bias map of photoresponse 52

2.16 Simultaneous optical modulation and photodetection 54
3.1 3D illustration of BP photodetector 58
3.2 Dark current in graphene photodetector 59
3.3 Polarization-dependent Raman spectra 62
3.4 Optical and AFM images of BP photodetector 63
3.5 Absorption per layer of BP photodetector 65
3.6 Simulated absorption vs BP thickness 66
3.7 Electrical transport properties of BP 68
3.8 Bias and gate dependent photocurrent 69
3.9 Photocurrent map, responsivity, and quantum efficiency 71
3.10 Broadband frequency response of BP photodetector 73
4.1 Optical image of BN-BP-BN photodetector 81
4.2 Setup for ultrafast photocurrent spectroscopy 82
4.3 Illustration of saturation in BP photodetector 83
4.4 Nonlinear and anisotropic response of BP photodetector 85
4.5 Saturation ratio verses optical power 86
4.6 Bias dependent carrier lifetime in BP 88
4.7 THG observed from a BP device 90
4.8 SHG and THG diagram 92
4.9 THG experimental setup 97
4.10 Exfoliated BP for THG 99
4.11 THG Spectrum and Power Dependence 100
4.12 THG Angular Dependence 101
4.13 THG Spatial Map 104
4.14 Autocorrelation measurement using THG from BP 105
4.15 THG thickness dependence 108

A.1 Process for waveguide planarization 142
A.2 Image of large area graphene transferred with PMMA support layer 144
A.3 Wet transfer method 147
A.4 Dry transfer method 150
B.1 Interference artifact from autocorrelation 153
B.2 Phase scrambler experimental diagram 154
B.3 Intensity modulation with sine wave 156
B.4 Phase dependent intensity 158
B.5 Maximum error for three driving waveforms 159
B.6 Reduction of interference fringes using phase scrambler 160

Chapter 1

Introduction

1.1 Motivation

1.1.1 The Growing Need for Silicon Photonics

In the past decade, we have observed an unprecedented growth in both the consumption and creation of data. Digital information created in the last two years alone now accounts for 90% of the total data currently in exsistence [1]. Relatedly, the demand for data storage and high performance computing continues to grow at an exponential rate [2], keeping in step with Moore's Law. While the number of transistors has continued to scale, the clock speed of CPUs has plateaued due to limits set by power consumption and heat dissipation [3]. The solution to this in recent years has been to fix the clock speed while increasing the number of cores per CPU. This parallel architecture increases processing power, but also introduces new scaling issues concerning data handling between multiple CPUs [1, 2]. Additionally, the trend towards "3D chips," such as the hybrid memory cube [4], will require a much higher bandwidth density for inter-chip communication than

their 2D counterparts.

Traditional electrical interconnects are not up to the challenge largely due to limited bandwidth, electrical cross-talk, and low input/output pin density. While the inter-chip bandwidth continues to grow, the metal interconnect pitch is expected to remain fixed around 100 μm, which translates to an interconnect bandwidth surpassing 40 Gbps by 2020 [1]. Such bandwidth density is not possible with current electrical interconnects, especially with the high losses and large interfacial reflections that accompany long-distance transmission lines on PCBs.

Silicon photonics, the use of silicon nanowires to guide light, is a promising solution to route information on- and off-chip. It is possible to exploit the benefits of optical networks (such as high bandwidth, low propagation loss, and low cross-talk) while using a platform compatible with current electronics. With wavelength division multiplexing (WDM), very high bandwidth density is also possible in a highly compact, sub-micron waveguide geometry [5]. The large refractive index contrast that exists between a silicon waveguide and its silicon oxide cladding has the highly desirable property of strongly confining light to the core of the waveguide. This minimizes unwanted coupling between two closely spaced waveguides, allows for compact photonic devices, and enables strong light-matter interaction for non-linear optical applications [6]. From an economics perspective, silicon photonics has the added benefits of low material cost, large wafer size, and many decades of CMOS processing experience [7].

While silicon photonics is highly promising for optical routing, a complete optical network also requires the generation, modulation, and detection of light—something difficult to achieve in an entirely monolithic platform. The growth of germanium for photodetection and III–V materials for light generation is technologically challenging on a silicon substrate due to mismatched lattice constants

and thermal expansion coefficients [8]. Defects arising from imperfections during crystal growth also tend to limit the optical and electrical performance of such devices [9].

1.1.2 Motivation for Two-Dimensional Materials

One solution to this problem is to grow materials on a compatible substrate and then transfer them onto silicon. In this way, it is not necessary to match lattice constants or thermal coefficients as required in direct growth processes. Two-dimensional (2D) materials are a class of crystals that naturally lend themselves to this type of transfer process. Because these materials are covalently bonded in-plane and held together out-of-plane by van der Waals forces, individual atomic planes can be mechanically separated from the bulk crystal and placed onto arbitrary substrates. Additionally, an entire family of 2D materials have been discovered with properties which span from metallic to semiconductors and insulators, providing the same building blocks as three-dimensional materials.

Owing to strong quantum confinement out-of-plane, 2D materials have many unique properties that are uncommon in their three-dimensional counterparts which make them particularly attractive for optoelectronic applications. For example, graphene exhibits very high mobility [10] and uniform optical conductivity [11, 12] due to its linear energy-momentum dispersion. Quantum confinement also plays a role in black phosphorus whose bandgap is highly tunable with the number of layers—from 0.3 eV in bulk to around 2 eV in an isolated monolayer [13–15]. Other highly unique properties are also present in transition metal dichalcogenides (TMDCs) which possess a valley degree of freedom that can be accessed optically [16–18] and has been used to create an LED that emits circularly polarized light [19]. Additionally, since the "bulk" and the surface are one

and the same for 2D materials, strong control of the chemical potential can be achieved by simply applying an electric field out of plane [12, 20].

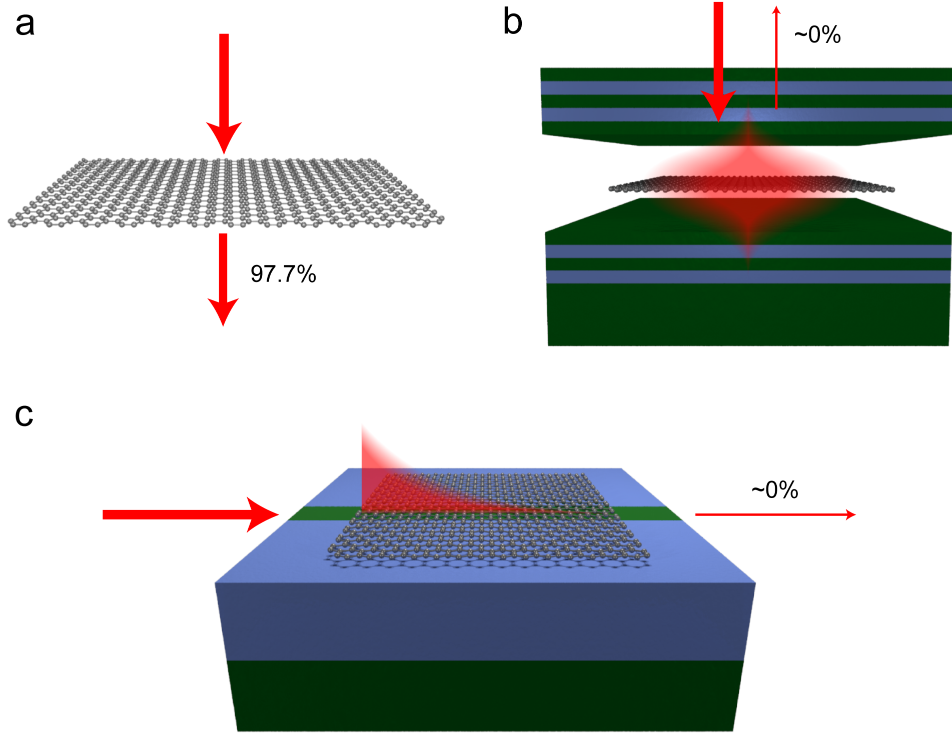

Figure 1.1: Various configurations for light-matter interaction in 2D materials. (a) Normal incident light has the advantage of broadband absorption, but very small total absorption. (b) Absorption can be enhanced by placing a 2D material inside an optical resonator to enhance light-mater interaction. This enhances absorption but limits the optical bandwidth of the device. (c) Waveguide integration of 2D materials overcomes both limitations by providing a platform that increases the interaction length while maintaining broad optical bandwidth.

While 2D materials have many desirable properties, their innate thinness greatly limits light-matter interaction in free space. Graphene, for instance, is able to absorb 2.3% of normal incident light per monolayer [11, 21]. This is a considerable amount in terms of a material that is only one atom thick, but very little in terms of total absorption as shown in Figure 1.1a. One approach has been

to insert 2D materials into optical cavities, such as a Fabry-Prot cavity [22, 23], to enhance the optical interaction with the material (see Figure 1.1b), but this limits the optical bandwidth to the linewidth of the cavity resonance. A solution to circumvent such a limitation is to place the 2D material onto a planar waveguide and couple to the optical mode via the evanescent field [13]. In this manner, one is able to decouple the interaction length from the material thickness since the material lies in the same plane as light propagation (Figure 1.1c).

In this introductory chapter, we review recent progress toward integrating 2D materials with silicon photonics for optoelectronic applications. We began by motivating silicon photonics and the benefits of planar integration of 2D materials. In the next two sections, we will discuss progress in photodetection (section 1.2) and modulation (section 1.3) using 2D materials on silicon photonics. Section 1.4 describes our contributions to the field and provides an outline for this dissertation.

1.2 Photodetection

1.2.1 Graphene Photodetectors

In terms of optical bandwidth, graphene's gapless nature enables absorption from the ultraviolet to the terahertz regime [24]. This extremely broad optical sensitivity is unrivaled by any other known material and is especially attractive for on-chip optical communication where information can multiplexed over a wide range of wavelengths. In 2009, Xia *et al.* demonstrated one of the first graphene photodetectors for normal incident light, which showed near-IR photoresponsivity of 0.5 mA/W at up to 40 GHz without signal degradation [25] (Figure 1.2a). However, the responsivity of this initial device was low (the corresponding quantum efficiency of only 4×10^{-4}). This was limited partially by the symmetry

of the electric field which was later improved in a subsequent device [26], but mainly by graphene's fixed 2.3% absorption. In late 2013, three groups independently demonstrated the first waveguide-integrated graphene photodetectors with significantly improved responsivities [27–29]. Through evanescent coupling, over 60% absorption was achieved in a 53 µm long device [27]. Careful asymmetric placement of the electrical contacts with respect to the waveguide (shown in Figure 1.2b) also aided to improve responsivity by exploiting the difference in work-function between the graphene and the metal [27, 29]. Additionally, these devices show flat responsivity over a wide selection of wavelengths in the telecommunications band [27, 30]. Based on the measured optical response [11, 12], this trend is expected to extend to the mid-IR.

The flexibility of using a planar waveguide geometry opens the possibility for novel device designs. By stacking two graphene monolayers separated by a thin dielectric, in early 2014 we demonstrated a dual-function graphene photodetector and modulator in a single device geometry [31] (Figure 1.2c). The top graphene sheet served as a transparent gate electrode which tuned the Fermi level and therefore the optical absorption in the bottom graphene layer. To measure the optical absorption in the bottom layer with high precision, we placed the device onto one arm of an unbalanced Mach-Zehnder interferometer. These results are discussed in detail in chapter 2 of this dissertation. Other designs have used photonic crystal waveguides to guide light [32] and enhance optical absorption through cavity resonance [33]. While this can improve optical absorption and allow for devices with smaller footprints, incorporating resonant enhancement will of course limit the usable optical bandwidth of the device.

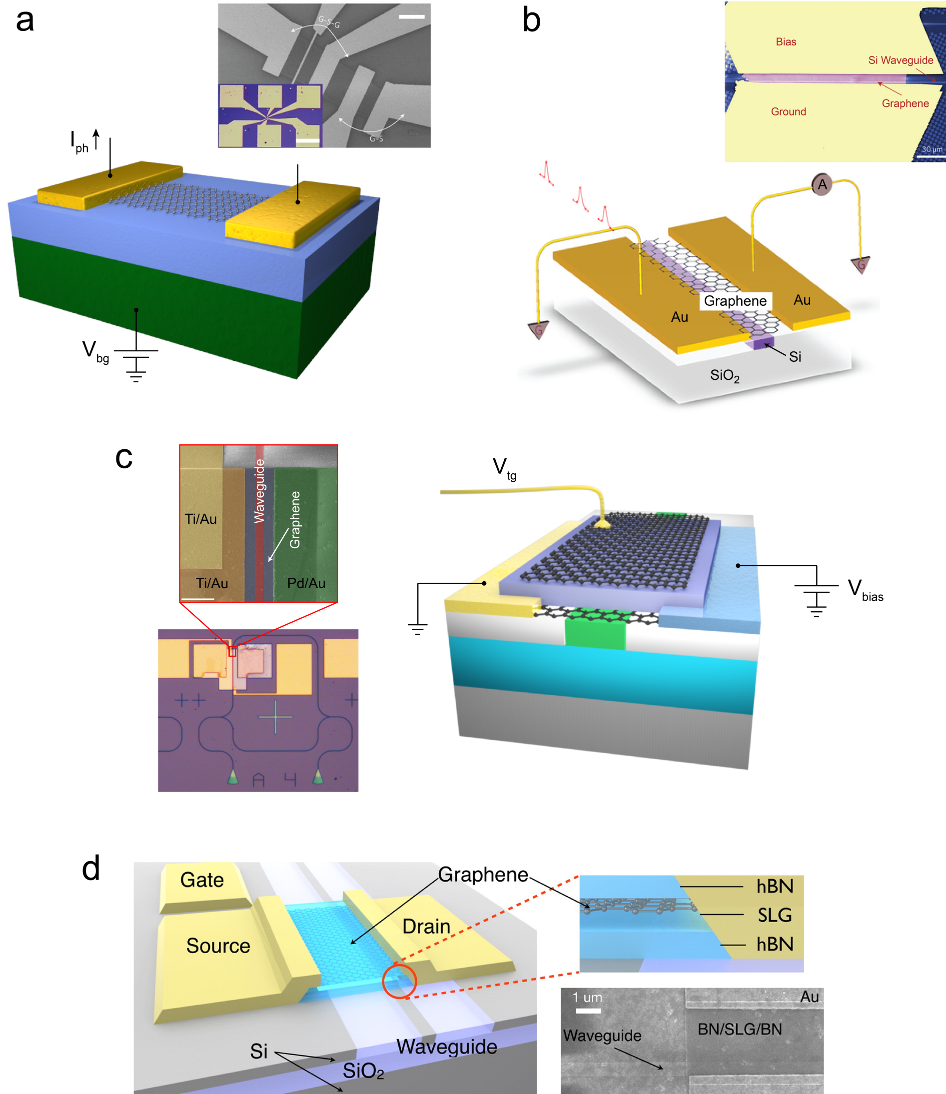

Figure 1.2: Graphene photodetectors. (a) The first graphene photodetector was illuminated with normal incidence light and gated with the substrate. Inset: SEM and optical microscope images of device (scale bars 2 µm and 80 µm respectively). (b) Waveguide integrated graphene photodetector demonstrated by Gan *et al.* An asymmetric placement of electrodes enabled zero-bias responsivity. (c) Multifunctional graphene photodetector and modulator using two different metal contacts to create a built-in potential. An integrated Mach-Zehnder is used to measure the graphene absorption with high precision. (d) High speed graphene photodetector with van der Waals passivation and one-dimensional edge contacts. Autocorrelation measurements with a resolution of 3 ps were demonstrated with this device. Reproduced with permission from (a) [25], (b) [27], (c) [31], and (d) [30].

Another attractive feature of using graphene is the potential for very high-speed photodetection. This is enabled by its extremely high carrier mobility and speeds greater than 500 GHz have been predicted [25]. Ultrafast autocorrelation measurements have experimentally measured the intrinsic frequency response of graphene photodetectors [34, 35]. This revealed that after initial excitation and rapid carrier-carrier scattering (on the order of tens of femtoseconds), the photo-excited carriers undergo a fast cooling process (*i.e.* the recombination time) mediated by phonon scattering and are collected at the contacts on a time scale (*i.e.* the transit time) that depends on the mobility, transit length, and field potential in the channel. While a fast recombination time can improve the overall speed of the photodetector, a faster transit time is always more desirable since fast carrier collection is required to achieve high quantum efficiency. It was shown that both these processes occur on the order of a few picoseconds in graphene which corresponded to an intrinsic frequency response of 262 GHz and an internal quantum efficiency of 16–37% in relatively low mobility devices [34].

Improved high-frequency design of electrical contacts [36] and the use of van der Waals heterostructures to improve mobility [30] have resulted in graphene waveguide-integrated detectors able to detect data rates up to 50 Gbps. In the latter case, Shiue *et al.* encapsulated single layer graphene between two sheets of boron-nitride (BN) and fabricated one-dimensional contacts [30] (see Figure 1.2d). The BN encapsulation has been shown to dramatically improve mobility by reducing Coulomb scattering found in SiO_2 supported graphene in addition to providing an atomically smooth substrate [37]. Reduced contact resistance has also been demonstrated in BN/graphene/BN heterostructures by exposing the graphene edge through a dry etch process before depositing a metal layer [10]. These improvements increased the 3 dB bandwidth to 42 GHz and a maximum

responsivity of 0.36 A/W was observed. It was also demonstrated that in the nonlinear regime, the photodetector operated as an on-chip autocorrelator with a timing resolution of 3 ps.

1.2.2 Black Phosphorus Photodetectors

While graphene is very attractive from the perspective of speed and broad optical sensitivity, it is fundamentally limited by its zero band gap. In photodetectors, this manifests itself as dark current which can be much larger than the measured photocurrent when the photodetector is operated in the photoconductive mode [26] (*i.e.* a bias voltage is applied to improve the responsivity). The inability to turn off the conductance of graphene devices leads to continuous energy consumption and high shot noise associated with the dark current, which significantly limit their use in real-world applications. One solution is to operate graphene photodetectors in the photovoltaic mode at zero bias and rely on a built-in asymmetric field profile to sweep photo-excited carriers to the metal contacts [26,27,30,31,36]. However, this approach is limited by the relatively weak responsivity at zero bias.

In contrast to graphene, TMDCs have bandgaps in the range of 1–2 eV which allow for very large field-effect on-off ratios, but their frequency response is typically limited to several kHz due to mid-level trap states and low mobility [38,39]. Picosecond response times in few-layer WSe_2 have been observed with autocorrelation measurements where the photo-excited carriers were extracted vertically using a van der Waals heterostructure [40]. In this design, the channel length is limited by the thickness of the WSe_2 rather than the spacing between two lateral electrodes. Since the response time scales as the channel length squared for transit-limited devices, these vertical heterostructures can significantly improve the frequency response of 2D materials with low mobility. However, the bandgap

of TMDCs corresponds to the visible spectral range and thus is unsuitable for applications in the near- and mid-IR range.

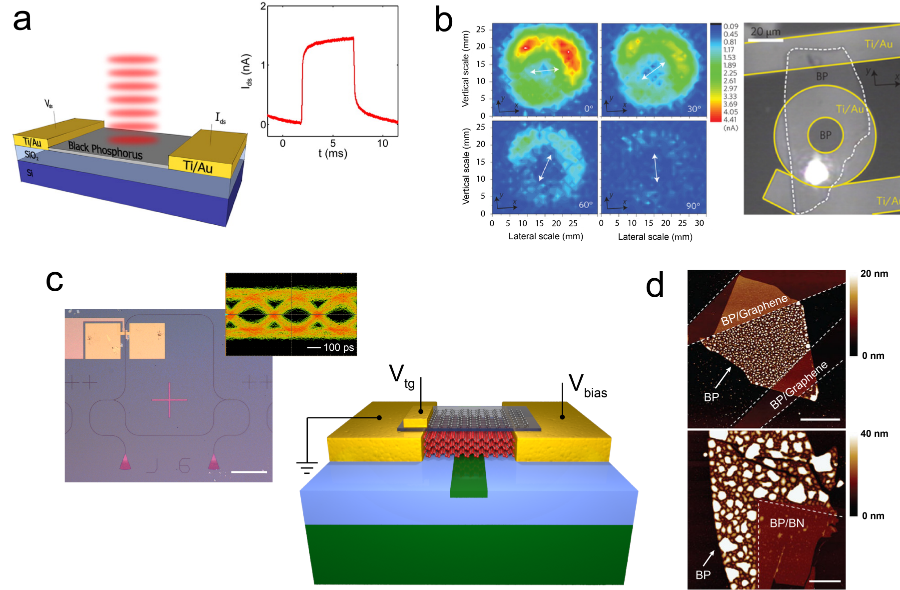

Figure 1.3: Black phosphorus photodetectors. (a) Normal incidence black phosphorus photodetector. Slow detection speeds were observed in this device with a rise and fall time on the order of a few milliseconds. (b) Polarization dependent photocurrent in BP. Anisotropic optical absorption along the x- verses y-direction accounts for the difference in measured photocurrent. (c) BP waveguide integrated photodetector. A top gate is used to dope the channel intrinsic for high speed detection. The device shows an open eye diagram for data rates as high as 3 Gbps. (Scale bar for optical image is 100 µm.) (d) Methods for passivating BP using van der Waals heterostructures. Both graphene and BN provide high quality passivation as can be seen in AFM profiles of partially covered BP allowed to oxidize (scale bars are 4 µm). Reproduced with permission from (a) [41], (b) [42], (c) [43], and (d) [44].

Black phosphorus (BP) was rediscovered as a van der Waals material a couple of years ago [45] and is already showing great promise for the near- and mid-IR [43, 46–49]. With a direct bandgap that scales with the number of layers from the visible to mid-IR [14, 15, 50], BP is an exciting new addition to the family

of 2D materials. Recent work has shown that when alloyed with arsenic, the bandgap can be pushed even further to 150 meV (∼8 µm) [51]. Unlike TMDCs, the mobility of BP is measured to be around 1350 cm^2/V·s at room temperature in thin samples [52] and greater than 10,000 cm^2/V·s in bulk samples at low temperatures [53]. Additionally, the buckled structure of BP causes it to have unique anisotropy in optical absorption [50, 54], carrier mobility [54], and thermal conductivity [55–57]. Due to this anisotropy, polarization-sensitive photodetectors have been demonstrated with BP [42] as shown in Figure 1.3b.

Shortly after the first demonstration of BP field effect transistors [45], several groups demonstrated normal incidence photodetectors using BP [41, 47–49]. Like normal incident graphene photodetectors, however, these devices were limited to responsivities of tens of mA/W due to small absorption. Additionally, the frequency response of these initial BP photodetectors was poor and it was unclear if they could be operated at speeds higher than a few kHz. Figure 1.3a shows one such photodetector which has a rise and fall time on the order of a few milliseconds [41]. In 2015, we demonstrated the first waveguide-integrated BP photodetector (Figure 1.3c) which showed an intrinsic responsivity of 135 mA/W and 657 mA/W in 11.5-nm- and 100-nm-thick devices respectively [43]. By adding a transparent graphene gate to the thinner device and measuring the photoresponse at various gate voltages, we were able to observe two unique photocurrent mechanisms at play. At large doping levels, the slower bolometric effect dominated which has thermal origins (f_{3dB} = 200 kHz). Low doping levels, on the other hand, revealed an RC-limited photovoltaic effect (f_{3dB} =3 GHz) where the photocurrent had the same sign as the applied bias. Additionally, the dark current was greatly reduced for low doping levels giving results comparable to waveguide-integrated germanium photodetectors with a similar configuration [58]. Again by

using an integrated Mach-Zehnder interferometer, we accurately determined the absorption in the BP layer and found that the internal quantum efficiency could be as high as 50% for large bias voltages. The details of this work are described in chapter 3 of this dissertation and in chapter 4 we use ultrafast pump-probe techniques to measure the intrinsic speed of a BP photodetector.

Recent work by Guo *et al.* revealed that trap states arising from impurities and surface states in the BP can provide a gain mechanism through the photogating effect [46]. This effect was most pronounced at the maximum of the trans-conductance (*i.e.* $\Delta I_{\mathrm{DS}}/\Delta V_{\mathrm{G}}$) where the hole transit time was shortest, but the number of available trap states for the electrons was large. According to Guo *et al.*, the ability to trap photo-excited electrons leads to a large photoconductive gain, which is the ratio of the electron trap lifetime to the hole transit time ($G = \tau_0/\tau_{tr}$). For a mid-IR wavelength of 3.39 µm, responsivity as high as 82 A/W was achieved at 500 mV bias and 1.6 nW incident power. However, this gain drastically reduces with increasing optical power as the available trap states are saturated and operates at low frequencies ($f_{\mathrm{3dB}} = 1.1\,\mathrm{kHz} \approx 1/2\pi\tau_0$). As the power increases, the effect of these trap states reduces and the dominant photocurrent mechanism at low doping levels is the high-speed photovoltaic effect [43].

While BP photodetectors have superior dark current performance compared to graphene detectors, there are also a few drawbacks. First of all, the best room temperature mobility in few-layer BP is two orders of magnitude less than that achievable in graphene [52]. This limits the ultimate speed of BP photodetectors, but using a vertical van der Waals heterostructure might be one way to overcome this. Secondly, the absorption per layer of BP is less than graphene (about one-eighth) at near- and mid-IR wavelengths [50]. This is not a significant issue when

using multi-layer BP, but it could lead to longer integrated devices as the thickness of BP is reduced. Finally, BP suffers from oxidation and degradation when exposed to humidity and light [59]. This has been solved by either passivating the surface with an ALD-grown dielectric [60] or sandwiching BP between other 2D materials such as graphene or BN [44] as shown in Figure 1.3d. Since there are approaches to overcome these drawbacks, BP photodetectors are very promising for IR applications.

1.3 Modulation

1.3.1 Graphene Modulators

While the lack of a bandgap limits graphene's practical applications for photodetectors, strong, broadband optical absorption, combined with a low density of states, makes graphene very promising for optical modulation. The principle behind optical modulation in graphene relies on the ability to tune the magnitude of its Fermi level to greater than (or less than) half the incident photon energy. At this point, graphene is no longer able to absorb incoming photons through an inter-band transition since there are either no available carriers or excited states [20]. Although it is true that this approach should work from infrared to visible wavelengths due to graphene's linear dispersion relation (intra-band absorption begins to play a significant role in the far infrared and terahertz region), it becomes increasingly difficult to achieve chemical potentials much larger than 0.4 eV. This is because the Fermi level scales as the square root of the gate voltage which is in turn limited by the breakdown field of the gate dielectric. Polymer electrolytes, on the other hand, have much higher gate capacitance than traditional

gate dielectrics [61], but operate at slow speeds since the doping mechanism requires physical movement of ions through the electrolyte. Therefore, most optical modulator studies have focused on near-IR wavelengths.

The first functional graphene modulator was demonstrated by Liu *et al.* in 2011 [62]. In this device, a sheet of CVD graphene was draped over a doped silicon waveguide, separated by a 7-nm-thick Al_2O_3 cladding as illustrated in Figure 1.4a. The doped silicon waveguide was used as a back gate and controlled the Fermi level in the graphene. A modulation depth of around 4 dB and an RC time-limited bandwidth of 1 GHz was observed. This design suffers from a trade-off between free carrier absorption if the silicon waveguide is heavily doped and a large RC time constant if it is lightly doped. A solution that was both suggested [63] and demonstrated [64] a year later was the use of two graphene monolayers separated by a thin dielectric (Figure 1.4b). In this design, the bottom graphene layer is gated by the top which can act either as a transparent gate electrode or additional absorber depending on the chemical potential [63]. This improved design showed a modulation depth of 6.5 dB and 3 dB bandwidth of 3 GHz [64]. Later groups reported improved results on a waveguide geometry including our dual-function photodetector and modulator [31] (see Chapter 2), a modulator with 3.3 dB insertion loss and 16 dB modulation depth [65], and a device capable of 10 Gbps modulation speeds [66].

Although integrating graphene onto a waveguide has the benefit of a very broad optical bandwidth, there is a fundamental tradeoff between modulation depth and energy consumption. A longer device will provide greater modulation depth, but will result in a higher capacitance and therefore consume more energy per bit flip [67]. One solution to this problem is to integrate a smaller graphene absorber into an optical resonator. This will reduce power consumption at the expense

of optical bandwidth. Two groups independently demonstrated using graphene on a photonic crystal cavity (PCC) to modulate the resonance conditions [68, 69]. While both groups used ion gel (which cannot be used for high speed applications) to control the Fermi level in graphene, the device area was greatly reduced which could lead to significant energy savings. A graphene/BN/graphene van der Waals heterostructure combined with a PCC was later demonstrated which was not limited by the use of ion gel [70] (Figure 1.4c). This device was suffered from excess capacitance, however, which reduced the 3 dB bandwidth to 1.2 GHz.

Ring resonators have also been used to increase the efficiency of graphene modulators and have been much more successful in experimental demonstrations. While PCCs have the advantage of a much smaller mode volume, ring resonators are easier to fabricate and usually have a higher Q which compensates for the larger size. The first graphene modulators integrated on a ring resonator were optimized for low voltage applications and overall efficiency rather than speed [71, 72]. The highest 3 dB bandwidth demonstrated in a graphene modulator is 30 GHz with a modulation depth of 15 dB [73]. This was achieved by Phare *et al.* who designed a ring resonator (see Figure 1.4d) that was under coupled for high loss and critically coupled for low loss. By changing the loss due to graphene in the resonator, the coupling between the ring and bus waveguide was modulated with an efficiency of 1.5 dB/V.

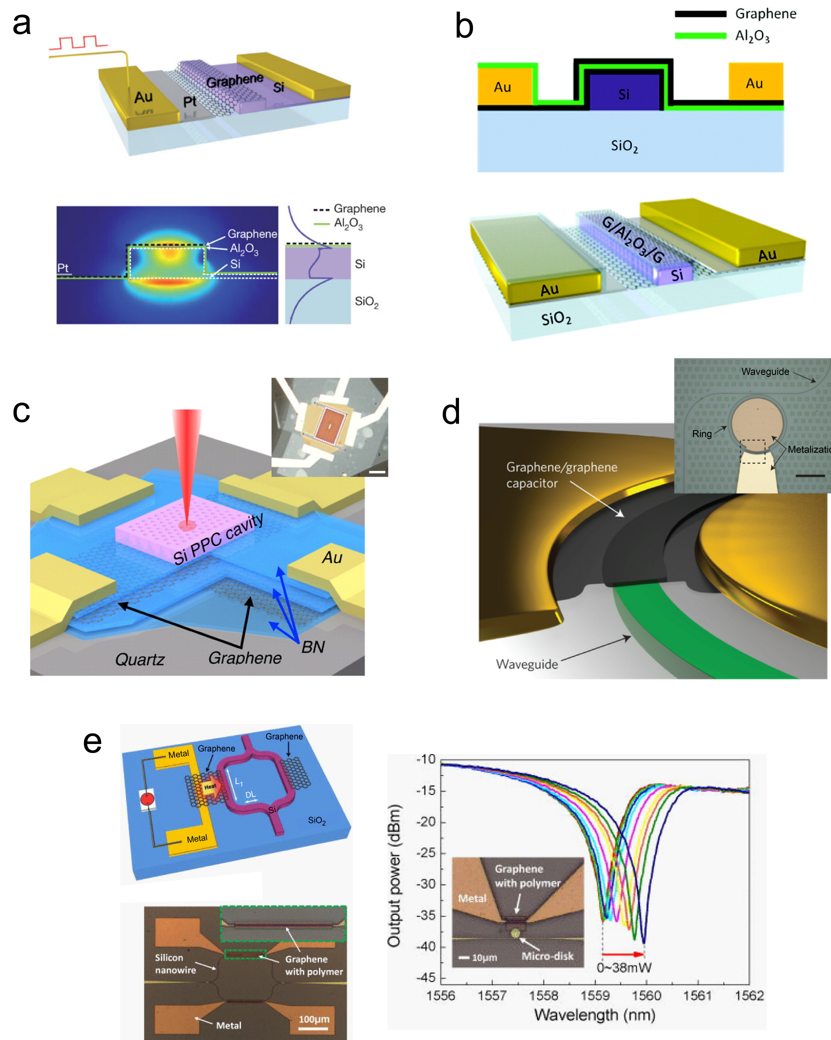

Figure 1.4: Graphene modulators. (a) First integrated graphene modulator using a doped silicon waveguide to gate the graphene layer. (b) An improved design that uses two graphene sheets to mutually gate the other. This design mitigates free carrier absorption in the waveguide while enhancing the modulation depth by a factor of two for optimally doped graphene sheets. (c) A van der Waals graphene modulator which uses BN as a gate dielectric. A PPC cavity was transferred onto the heterostructure which enhances optical absorption at the optical resonance. (d) Graphene modulator integrated in a ring resonator to improve modulation efficiency (inset scale bar 40 µm). High speed modulation was achieved with $f_{3\text{dB}} =$ 30 GHz. (e) Thermal modulation using graphene as a thermal conductor. High thermal conductivity of graphene allows faster modulation speeds over other conventional thermal heaters. Reproduced with permission from (a) [62], (b) [64], (c) [70], (d) [73], and (e) [74].

In applications not requiring high speed modulation, graphene's excellent thermal conductivity [75] could be useful for thermal tuning of silicon photonics. Yu *et al.* demonstrated thermal tuning in both a Mach-Zehnder interferometer and a micro-disk resonator using graphene to conduct heat from a non-local metal heater [74] (Figure 1.4e). Graphene itself can also be used in place of a traditional metal heater as demonstrated by Gan *et al.* [76]. This has the advantage of a higher modulation speed compared with traditional silicon thermo-optic modulators and sub-microsecond rise and fall times have been observed.

1.3.2 Black Phosphorus Modulators

While an integrated optical modulator has yet to be demonstrated using BP, a few theory papers have suggested that an out-of-plane electric field could be used to change the optical absorption of multilayer BP [50, 77]. For several nm-thick BP, two competing mechanisms affect the optical absorption. The first is the Pauli-blocked Burstein-Moss shift (BMS), similar to graphene, which prevents optical absorption for photons with energies less than twice the Fermi level. This tends to increase the optical band gap. On the other hand, the quantum-confined Franz-Keldysh (QCFK) effect cause the wavefunctions of a quantum well to extend into the bandgap in the presence of an electric field. This decreases the optical band gap and fights the BMS effect at high doping levels. Lin *et al.* calculated these combined effects for the case of a BP quantum well integrated on a silicon waveguide and demonstrated that a 62% reduction in the required voltage swing could be obtained in 20-nm-thick BP quantum well compared with graphene for an equivalent change in absorption [77]. The improvement comes from the QCFK effect which is not limited by temperature-induced smearing of the optical transition edge which is present in graphene at room temperatures (see section 2.2.2 for

a more detailed discussion). However, this improvement in efficiency only occurs for wavelengths near the band edge of the BP quantum well where the QCFK effect is strongest. Very recently, modulation due to both the BMS and QCFK effects have been experimentally observed at low temperatures for BP flakes on a SiO_2/Si substrate [78], but an integrated BP modulator has yet to be realized.

1.4 Dissertation Outline

The work comprising this dissertation is arranged as follows:

- Chapter 1 motivated the integration of 2D materials with silicon photonics and placed the contributions of this dissertation in the context of the current state of the field.

- Chapter 2 discusses the theory of graphene photodetectors and optical modulators and presents the experimental results of our dual functional graphene photodetector and modulator integrated on a silicon photonics platform.

- Chapter 3 presents the experimental results of our waveguide integrated black phosphorus photodetector and discusses the physical mechanisms revealed through our measurements.

- Chapter 4 discusses ultrafast pump-probe techniques used to probe BP's nonlinear electrical and optical response. Here, we present our experimental measurements of the photo-carrier lifetime in a BP photodetector and $\chi^{(3)}$ in black phosphorus flakes.

- Chapter 5 gives a summary of the work presented in this dissertation along with a discussion of future perspectives.

- Appendix A and B provide details on the fabrication and experimental techniques developed during the course of this work. Appendix C provides a theoretical understanding of optical nonlinearity in BP.

Chapter 2

Dual-Function Graphene Photodetector and Modulator

Graphene's unique optoelectronic properties have been exploited for many photonic applications. Here, we demonstrate a single graphene-based device that simultaneously provides optical modulation and photodetection. The graphene device is integrated on a silicon waveguide and is tunable with a graphene gate to achieve a near-infrared photodetection responsivity of 57 mA/W and modulation depth of 64% with GHz bandwidth. Simultaneous modulation of photocurrent and optical transmission has been achieved, which may lead to unprecedented optoelectronic applications.

2.1 Photocurrent mechanisms in graphene

When analyzing photocurrent from graphene devices, it is important to first understand the various mechanisms that play a role in generating a current. Often the photocurrent observed experimentally is actually the combination of multiple

effects. Here we provide an overview of the various photocurrent mechanisms in graphene and how to identify these effects experimentally. While we have chosen to focus on graphene in this chapter, the photocurrent mechanisms discussed here are directly applicable to the black phosphorus photodetectors presented in chapter 3.

2.1.1 Photovoltaic effect

The photovoltaic effect is the most familiar and straight-forward photocurrent mechanism in graphene photodetectors. In this case, electron-hole pairs are generated through the absorption of incident photons and swept to the contacts where they are collected and generate a current. A signature of the photovoltaic effect is the sign of the photocurrent. Since the electric field in the channel is dependent on the bias voltage applied to the source and drain contacts, the photocurrent will have the same sign as the bias voltage and will have a linear dependence on the electric field for small bias voltages (figure 2.1a). In graphene, the photovoltaic effect is strongest when the channel is intrinsic (*i.e.* the Fermi energy is at the Dirac point) since carrier-carrier scattering reduces the carrier lifetime at high doping levels [79].

One can model the photocurrent from the photovoltaic effect by considering the spatial distribution of the photoexcited carriers $n^*(\mathbf{r})$ and the electric field profile in the channel $-\nabla V(\mathbf{r})$:

$$j_{\mathrm{PV}}(x) = -q\mu n^*(x)\frac{dV(x)}{dx} \tag{2.1}$$

where q is the unit charge, μ is the carrier mobility, and $V(x)$ is the potential profile in the channel. In this case, we have assumed that the channel potential is uniform in the y direction so equation 2.1 depends only on x.

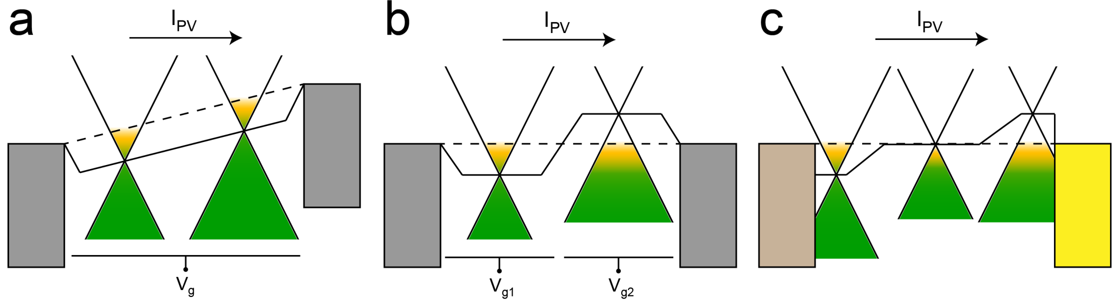

Figure 2.1: Illustration of photovoltaic photocurrent in three possible device configurations. (a) When a bias is applied, the electric field in the channel will sweep photocarriers to the contacts. Even under zero-bias, the photovoltaic effect can be non-zero with a non-symmetric doping profile (b) or contacts with different work functions (c).

It is often possible to have a contribution from the photovoltaic effect at zero-bias for non-uniformly doped graphene or near the source-drain contacts due to a difference in work function between the metal and graphene like in figure 2.1b and c. This causes local band-bending and net photocurrent can be observed for a device with either non-symmetric illumination or metal contacts with different work functions. In studies that make use of photocurrent mapping, this effect is easy to see at zero bias [26, 27, 79]. It is important to note that the photo-thermoelectric effect can also play a significant role at zero bias and care must be taken when trying to separate the effects of these mechanisms.

2.1.2 Bolometric effect

The bolometric effect arises from temperature-dependent transport which changes the resistance of the channel. In this case, optical excitation heats the channel and surrounding material which increases the electron-phonon scattering in graphene and reduces the channel conductance [79]. This photocurrent can only be observed

in devices which are under an applied biased and appears as a decrease in the dark current with increasing optical power. Since the rise in temperature leads to an increase in the channel resistance and therefore a decrease in the magnitude of the dark current, the bolometric effect always appears as a photocurrent with a sign opposite to the applied bias (figure 2.2). This allows easy distinction from the photovoltaic current which follows the sign of the applied bias.

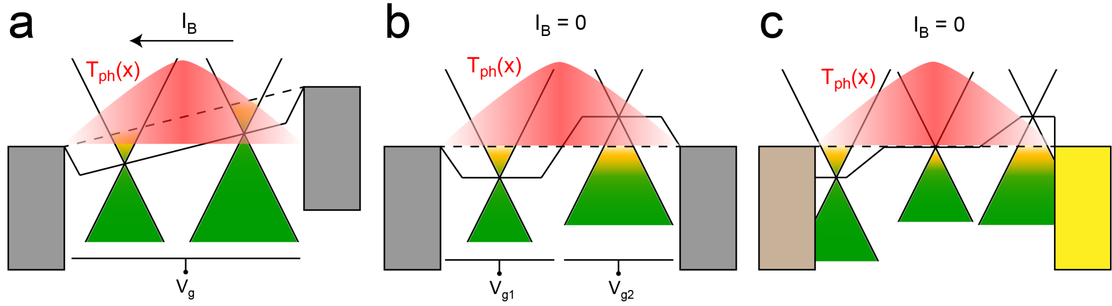

Figure 2.2: Illustration of bolometric photocurrent in three possible device configurations. Only under an applied bias (a) will the bolometric effect contribute to the net photocurrent. $I_\mathrm{B} = 0$ for (b) and (c) where no bias is applied.

The bolometric current can be modeled as follows:

$$j_\mathrm{B}(x) = \beta[T_\mathrm{ph}(x) - T_0]\frac{dV(x)}{dx} \tag{2.2}$$

where $\beta \equiv d\sigma/dT$ is the bolometric coefficient which can be determined by temperature-dependent transport measurements, T_ph is the phononic temperature, and T_0 is the ambient temperature. The phononic temperature is related to the electronic temperature T_e by the following coupled equations [48]:

$$-t\kappa_e\frac{\partial^2 T_e}{\partial x^2} + \gamma_{e-\mathrm{ph}}[T_e - T_\mathrm{ph}] = P(x) \tag{2.3}$$

$$-t\kappa_\mathrm{ph}\frac{\partial^2 T_\mathrm{ph}}{\partial x^2} + \gamma_0[T_\mathrm{ph} - T_0] = \gamma_{e-\mathrm{ph}}[T_e - T_\mathrm{ph}] \tag{2.4}$$

where t is the sample thickness, $P(x)$ is the absorbed power as a function of position along the channel, κ_e and κ_{ph} are the electronic and lattice thermal conductivities, and $\gamma_{e-\mathrm{ph}}$ and γ_0 are the energy loss rates of electrons to phonons and the lattice to the substrate respectively. κ_e is related to the electrical conductivity σ of the channel (in Ω^{-1}/m) through the Wiedemann-Franz law [80]:

$$\kappa_e = \frac{\pi^2}{3}\left(\frac{k_B}{q}\right)^2 \sigma T \tag{2.5}$$

The bolometric contribution to the current is most significant when the graphene channel is heavily doped [79]. The bolometric effect also plays a role in black phosphorus photodetectors and in chapter 3 we show that it is the dominant effect at high-doping levels. We also show that it has a much slower response than the photovoltaic current (since it is related to the thermal conductivity of the channel and surrounding materials) making it less useful for high-speed applications.

2.1.3 Photo-thermoelectric effect

The final contribution to photocurrent in graphene devices is the photo-thermoelectric effect. In this effect, electrons gain energy from absorbed photons which can be described by an elevated electron temperature T_e. When this happens (*i.e.* $T_e > T_0$), the electrons are called "hot electrons" and move with an energy greater than the thermal energy of the lattice. In conventional bulk materials, T_e reaches equilibrium with the lattice temperature T_0 very quickly through the emission of phonons. In graphene, however, this energy loss pathway is greatly limited for energies less than 200 meV leading to a "phonon bottleneck" [81]. These energetic carriers follow the electron temperature gradient and diffuse away from their point of origin to areas in the device where T_e is less. Net current is observed if carriers flow more in one direction than another and this can only occur at the junction of two

materials (see figure 2.3). The current generated due to the thermoelectric effect can be written:

$$j_{\text{PTE}}(x) = \sigma \frac{dV(x)}{dx} + \sigma S(x) \frac{dT_e(x)}{dx} \tag{2.6}$$

where $S(x)$ is the Seebeck coefficient of the material at position x. The Seebeck coefficient is characterized by the change in voltage per change in temperature for a given material and has units of V/K. The Seebeck coefficient can be found using the Mott formula [81–83]:

$$S = -\frac{\pi^2 k_B^2 T_0}{3q} \frac{1}{\sigma} \frac{d\sigma}{dV_G} \frac{dV_G}{dE}\bigg|_{\text{E}=\text{E}_f} \tag{2.7}$$

where k_B is the Boltzmann constant, V_G is the gate voltage, and E_f is the Fermi energy. The differential $\frac{d\sigma}{dV_G}$ can be measured experimentally from gated transport measurements and the differential $\frac{dV_G}{dE}$ can be calculated by considering the density of states in graphene (see section 2.2). Since the Seebeck effect arises from the thermal transport of charge carriers, we expect the Seebeck coefficient to be positive when the channel is p-doped and negative when the channel is n-doped.

It is worth mentioning that it is possible to achieve carrier multiplication in graphene through Auger-like processes. This occurs when electrons are excited to high energies by incident photons and rather than losing energy to phonons, lose energy to electron-electron collisions. In this process, the excited electron can impart some of its energy to unexcited electrons multiple times until a quasi-equilibrium[1] is reached. This multiplication process has been observed experimentally using terahertz transmission spectroscopy [84]. In this experiment, an energy-tunable pump beam was used to excite electrons and the transmission of a terahertz probe was used to measure the change in conductivity of a graphene

[1] The carriers created through this process contribute to the elevated electron temperature T_e which relaxes to T_0 on a time scale much longer than the time scale in which carrier multiplication occurs and therefore we say "quasi-equilibrium."

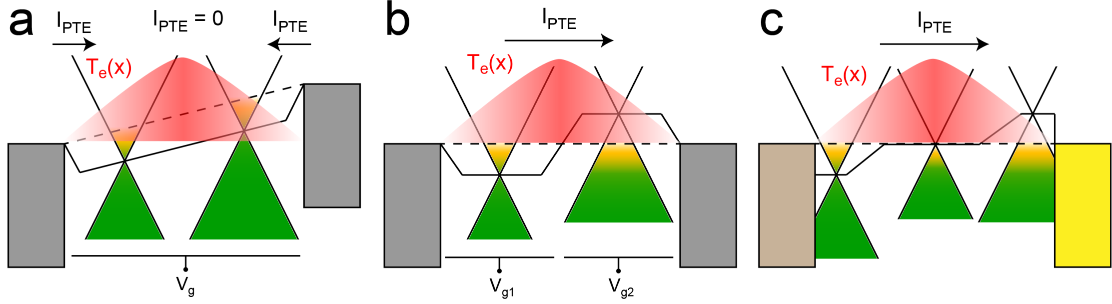

Figure 2.3: Illustration of photo-thermoelectric photocurrent in three possible device configurations. (a) Under bias condition, but with symmetric contacts, doping, and illumination, the photo-thermoelectric current will cancel. (b) With zero-bias and a non-symmetric doping profile, the hot electrons and holes flow in opposite directions, leading to net photocurrent. (c) For non-symmetric contacts the difference in work function between the metal and graphene will dope the graphene non-uniformly, leading to net photocurrent.

sheet. It was observed that for a given photon density, the conductivity increased linearly with photon energy, since higher energy photons excited more carriers though electron-electron collisions than lower energy photons. This carrier multiplication can play a role in the photo-thermoelectric effect since more excited carriers at the phonon bottleneck will lead to more thermoelectric current. Interestingly, this carrier multiplication is intrinsic to graphene and occurs regardless of the applied bias unlike avalanche photodiodes which require a high electric field before multiplication occurs.

The total current for a graphene photodetector under an applied bias can therefore be determined by adding all the individual components together [48]:

$$I = \sigma(V_d - V_s) - \int_0^L q\mu n^*(x)\frac{dV(x)}{dx}dx + \int_0^L \beta[T_{\text{ph}}(x) - T_0]\frac{dV(x)}{dx}dx + \int_0^L \sigma S(x)\frac{dT_e(x)}{dx}dx \tag{2.8}$$

Here we have included the contributions due to dark current and the photovoltaic,

bolometric, and photo-thermoelectric effects respectively. Note that the photo-thermoelectric component is independent of the applied electric potential $V(x)$ and therefore is often the dominant effect in devices at zero bias [81, 85].

2.2 Optical modulation in graphene

By modulating the carrier concentration in graphene, it is possible to modulate the absorption as well. This is due to the Pauli exclusion principle where a transition to a state of a given energy is either allowed or prohibited depending on whether or not the state is occupied as illustrated in figure 2.4. This effect is not unique to graphene, but is rarely observed in three-dimensional materials since it becomes very difficult to shift the Fermi level much above the conduction band or below the valence band due to the relatively high density of states. In graphene and other 2D materials, the density of states is significantly reduced and the Fermi level can be easily modulated *via* electrostatic doping which we discuss in the following section.

2.2.1 Electrostatically tuning graphene's Fermi level

In order to tune the Fermi level in graphene, one can employ chemical doping, ion gel, or electrostatic doping. Chemical doping is difficult to control precisely and is not dynamically tunable after the initial chemical treatment. Using ion gel is quite effective, but slow since the doping mechanism requires ions to physically diffuse through a polymer gel. Electrostatic doping, on the other hand, is a simple method which uses a parallel plate capacitor geometry to control the Fermi level. The modulation speed is limited by the RC time constant of the device which can be on the order of tens of GHz for optimally designed devices. Figure 2.5a

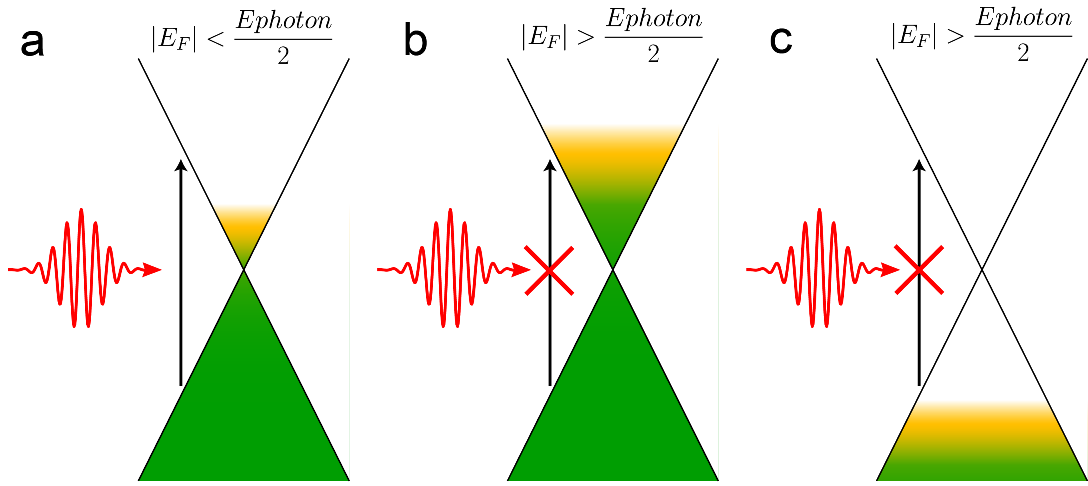

Figure 2.4: Optical modulation *via* the Pauli exclusion principle. (a) When the Fermi energy E_F is less than half the photon energy, electrons can absorb a photon and populate a higher energy state in the conduction band. (b) When $+E_F$ is greater than half the photon energy, there are no available states in the conduction band and absorption is prohibited. (c) When $-E_F$ is greater than half the photon energy, there are no available electrons in the valence band to absorb a photon and absorption is again prohibited.

illustrates the basic principle of this doping method.

A parallel plate capacitor has a capacitance per unit area of $C = \epsilon/t$ where ϵ is the dielectric constant of the material (in F/m) between the two plates and t is the separation. Since the capacitance is equal to the total charge divided by the voltage across the capacitor, we can write the charge per unit area on the top plate as follows:

$$n(V_G) = \frac{CV_G}{q} \tag{2.9}$$

where n is the carrier concentration in cm^{-2} and V_G is the applied gate voltage. When we make an actual device, we replace one of the metal plates with graphene so that by applying a voltage, we can change carrier concentration linearly. Now that we have an expression for the number of carriers in the graphene sheet, we

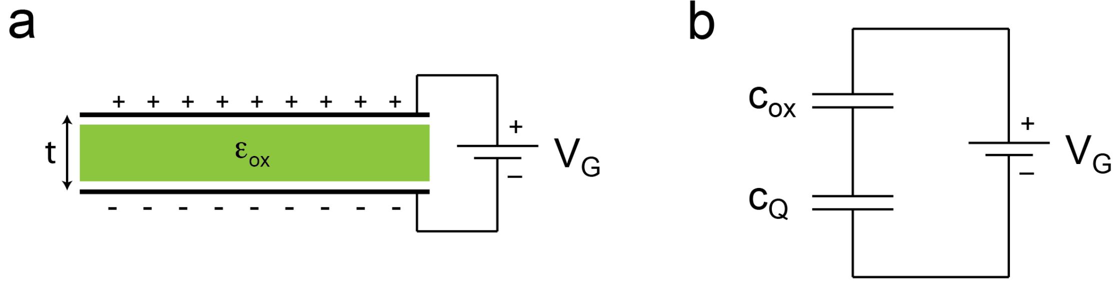

Figure 2.5: (a) Illustration of parallel plate capacitor geometry used to tune the Fermi energy of graphene. (b) Circuit diagram of oxide and quantum capacitance in series.

can calculate the Fermi energy as a function of gate voltage. This will be related to the number of states at a given energy (*i.e.* the density of states $g(E)$). In order to change the Fermi energy to a particular value in the conduction band, we will need to fill all the available states below that energy with electrons. To calculate this, we can use the energy dispersion for graphene:

$$E(k) = \pm\hbar v_F \sqrt{k_x^2 + k_y^2} = \pm\hbar v_F |k| \tag{2.10}$$

where $v_F \approx 10^6$ m/s is the "Fermi velocity." The density of states for graphene is calculated in the following way:

$$dN = 2g_v \frac{A}{\pi^2} \frac{2\pi k dk}{4}, \quad dk = \frac{dE}{\hbar v_F} \tag{2.11a}$$

$$\frac{dN}{dE} = \frac{dN}{dk}\frac{dk}{dE} = g_v \frac{A}{\pi} \frac{|E|}{(\hbar v_F)^2} \tag{2.11b}$$

$$g(E) = \frac{1}{A}\frac{dN}{dE} = \frac{2|E|}{\pi(\hbar v_F)^2} \tag{2.11c}$$

where dN is the differential number of states, A is the unit area and g_v is the valley degeneracy ($g_v = 2$ for graphene). Looking at the left equation in 2.11a, $2g_v$ accounts for the up and down spin of the electrons and the valley degeneracy, π^2/A is the area of k-space that a single state occupies (approximated by an

infinite square well), and $2\pi k dk$ is the differential area in k-space for a given value of k (dividing by 4 gives solutions in only the first quadrant since we only care about the magnitude of k). This gives us the change in the number of states N for a given change in k. The right equation in 2.11a is simply the derivative of equation 2.10. Combining these two equations in 2.11a, we can find the differential change in the number of states per change in energy (equation 2.11b). Finally, the density of states $g(E)$ is the number of states per energy per unit area. We can now relate the number of carriers to the Fermi energy using the following relationship:

$$n = \int_0^\infty g(E)f(E)dE = \int_0^\infty \frac{g(E)}{e^{(E-E_F)/k_BT}+1}dE \tag{2.12}$$

where $f(E) = 1/(e^{(E-E_F)/k_BT}+1)$ is the Fermi distribution. In the simple case of $T = 0\,\text{K}$, the Fermi distribution becomes a step function, and equation 2.12 becomes:

$$n = \int_0^{E_F} g(E)dE = \int_0^{E_F} \frac{2|E|}{\pi(\hbar v_F)^2}dE = \frac{E_F^2}{\pi(\hbar v_F)^2} \tag{2.13}$$

Substituting this into equation 2.9, we can solve for the Fermi energy as a function of gate voltage:

$$E_F = \hbar v_F \sqrt{\pi \frac{C|V_G|}{q}} \tag{2.14}$$

While this solution is valid only at low temperatures, it is a fairly good approximation even at room temperature and allows us to have an analytical solution. We can see from equation 2.14 that the Fermi energy[2] is proportional to $\sqrt{V_G}$ which makes it increasingly more difficult to change the Fermi energy at high gate voltages. For example, the breakdown voltage of Al_2O_3 is around $1\,\text{V/nm}$ [86] with a dielectric constant of $\epsilon_{\text{ox}} = 8$. If we have Al_2O_3, the highest Fermi energy we can hope to achieve is $0.78\,\text{eV}$ before the oxide breaks down regardless of the

[2] Note: The sign of E_F will depend on the sign of V_G.

oxide thickness. In reality, imperfect oxides will have trap states at the interfaces that will rob the graphene of carriers, lowering the Fermi energy. Additionally, the total capacitance is not simply the oxide capacitance, but also includes the quantum capacitance [87]:

$$
\begin{aligned}
C &= \left(\frac{1}{c_{\text{ox}}} + \frac{1}{c_{\text{Q}}}\right)^{-1} \\
c_{\text{Q}} &= \frac{2q^2 k_B T}{\pi(\hbar v_F)^2} \ln\left[2\left(1 + \cosh\left(\frac{E_F}{k_B T}\right)\right)\right] \\
c_{\text{ox}} &= \frac{\epsilon_{\text{ox}}\epsilon_0}{t_{\text{ox}}}
\end{aligned}
$$

When we have two metal parallel plates in a capacitor, we assume that the potential on the plates varies linearly with the number of carriers induced by the applied voltage across the plates. For a a material with a low density of states like graphene, however, the additional carriers will fill up empty states as the potential changes which in turn reduces the potential in the graphene. This can be thought of as an additional capacitor in series with c_{ox} which reduces the total capacitance (figure 2.5b). Based on equation 2.13, we expect the potential in the graphene to be proportional to the $\sqrt{n}$. We indeed see this for $E_F \gg k_B T$ where c_{Q} can be written as:

$$c_{\text{Q}} \approx \frac{2q^2 E_F}{\pi(\hbar v_F)^2} = \frac{2q^2}{\hbar v_F \sqrt{\pi}}\sqrt{n} \tag{2.15}$$

Figure 2.6 shows the effect quantum capacitance can have on the Fermi energy for two oxide thicknesses. We can see that when the oxide thickness increases, the oxide capacitance dominates and we can safely ignore the quantum capacitance effects. In the devices throughout this dissertation, we have used relatively thick gate oxides ($\geq 20\,\text{nm}$), but to optimize devices for low voltage applications *via* reducing the gate oxide, quantum capacitance should be considered.

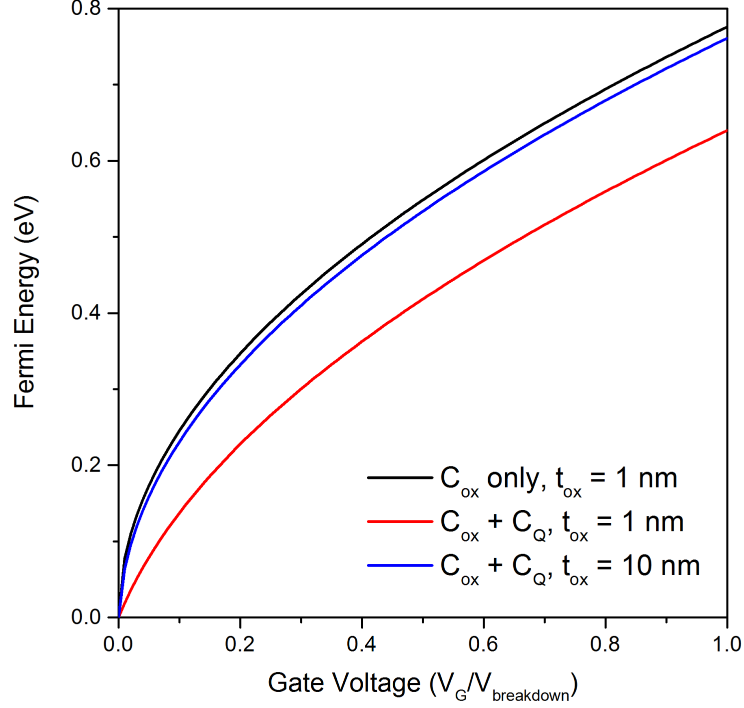

Figure 2.6: Effect of quantum capacitance on modulating the Fermi energy electrostatically. Figure shows Fermi energy of graphene verses gate voltage (normalized by the breakdown voltage) without quantum capacitance (black line) and with quantum capacitance for two oxide thicknesses (red and blue lines). Al_2O_3 was used as the gate oxide for these simulations ($\epsilon_{ox} = 8$, $V_{breakdown} = 1\,V/nm$).

2.2.2 Theory of optical absorption in graphene

Now that we have a way to modulate the Fermi energy with a gate voltage, we have a way modulate the optical absorption as well. In this section, we will derive optical absorption in graphene as a function of gate voltage. We can calculate the absorption by looking at the real part of the optical conductivity. In electromagnetic theory, the real part of the conductivity is related to the energy lost through

Ohm's law and Joule heating in the following equations:

$$\mathbf{J}(\mathbf{r},t) = \sigma\mathbf{E}(\mathbf{r},t) \tag{2.16}$$

$$Q(\mathbf{r},t) = \mathbf{J}(\mathbf{r},t)\cdot\mathbf{E}(\mathbf{r},t) \tag{2.17}$$

where $\mathbf{J}$ is the current density and Q is the resistive heating power. For a 2D conductive sheet, $\mathbf{J} = \mathbf{J}_s$ is the surface current (in A/m), $Q = Q_s$ is the surface heating power (in W/m^2), and $\mathbf{E} = \mathbf{E}_t$ is the electric field in the plane of the conductive sheet. We can calculate the time averaged surface resistive heating power as follows:

$$\langle Q_s(\mathbf{r})\rangle = \frac{1}{2}\mathrm{Re}\left[\mathbf{J}_s(\mathbf{r})\cdot\mathbf{E}_t^*(\mathbf{r})\right] = \frac{1}{2}\mathrm{Re}[\sigma]|\mathbf{E}_t(\mathbf{r})|^2 \tag{2.18}$$

So the loss due to resistive heating is due to the real part of the conductivity. (The imaginary part is related to the phase of electric field in the conductor.) We can apply the same principle to optical frequencies to calculate the absorption due to a graphene monolayer. According to theory, the real part of the optical conductivity $\sigma(\omega)$ for an ideal graphene sheet can be written as follows [88]:

$$\mathrm{Re}\left[\sigma(\omega)\right] = \mathrm{Re}\left[\sigma^{intra}(\omega)\right] + \mathrm{Re}\left[\sigma^{inter}(\omega)\right] \tag{2.19}$$

$$\mathrm{Re}\left[\sigma^{intra}(\omega)\right] = \frac{4e^2}{h}\frac{2k_BT\Gamma}{\omega^2+4\Gamma^2}\ln\left(2\cosh\frac{E_F}{2k_BT}\right) \tag{2.20}$$

$$\mathrm{Re}\left[\sigma^{inter}(\omega)\right] = \frac{e^2}{4\hbar}\left[f\left(-\frac{\omega}{2}\right) - f\left(\frac{\omega}{2}\right)\right] \tag{2.21}$$

where σ^{intra} and σ^{inter} are the intraband and interband contributions to the optical conductivity, ω is the photon energy, and Γ is the impurity scattering rate. For telecom photon energies in our devices ($\approx$0.8 eV), the intraband contribution is minimal (but non-zero!) and the interband contribution dominates the optical conductivity. Equation 2.21 can be written in a more convenient form using the

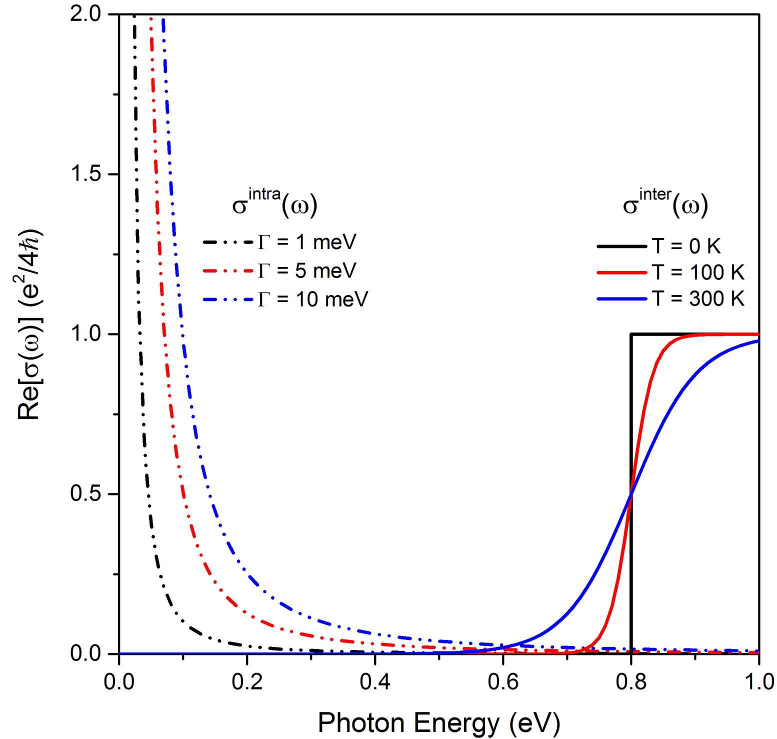

Figure 2.7: Plots of equation 2.20 (dashed lines) and 2.21 (solid lines) for various temperature and impurity scattering rates. The Fermi energy was kept fixed at $E_F = 0.4\,\text{eV}$.

hyperbolic sine and cosine:

$$\text{Re}\left[\sigma^{inter}(\omega)\right] = \frac{e^2}{4\hbar}\left[\frac{\sinh\left(\frac{\omega}{2k_BT}\right)}{\cosh\left(\frac{E_F}{k_BT}\right) + \cosh\left(\frac{\omega}{2k_BT}\right)}\right] \tag{2.22}$$

To visualize the intraband and interband contributions to the optical conductivity, we plot equations 2.20 and 2.21 for different Γ and T ($E_F = 0.4\,\text{eV}$) in figure 2.7. At the photon energies that are of interest to us, it is clear that σ^{intra} and σ^{inter} have very little overlap. We also see that for room temperature, σ^{inter} no longer resembles a step function which has a negative effect on the required voltage

needed to achieve a large modulation depth.

One can see that σ^{inter} saturates at $e^2/4\hbar$ for photon energies above $2E_F$. This is known as graphene's universal conductivity which is frequency independent from the visible to near-IR. If we consider a plane wave that is incident normal to the graphene sheet, we can calculate the power absorbed from the ratio of resistive heating $\langle Q_s \rangle$ to the time averaged Poynting vector of the incident field $\langle S_{in} \rangle$:

$$\frac{\langle Q_s \rangle}{\langle S_{in} \rangle} = \frac{\frac{1}{2}\mathrm{Re}[\sigma(\omega > 2E_F)]|\mathbf{E}_t|^2}{\frac{1}{2}\epsilon_0 c|\mathbf{E}_t|^2} = \frac{\frac{e^2}{4\hbar}}{\epsilon_0 c} = \pi\left(\frac{e^2}{4\pi\epsilon_0\hbar c}\right) = \pi\alpha \approx 2.3\% \qquad (2.23)$$

where α is the fine structure constant. This means that as long as $\omega > 2E_F$, the graphene sheet will absorb a fixed 2.3% of the incident light (ignoring effects of temperature on the absorption edge as seen in figure 2.7). In general, the fractional power absorbed by graphene can be written as:

$$\langle P_{abs}(\omega) \rangle = \frac{1}{\epsilon_0 c}\mathrm{Re}[\sigma(\omega)] \qquad (2.24)$$

Combining equations 2.14, 2.19, and 2.24, we can plot the absorption as a function of gate voltage.

From figures 2.8a and b, we can see that temperature plays a large role in how efficiently one can modulate graphene's absorption. For low temperatures, the absorption resembles a step function which significantly reduces the gate voltage swing needed to turn on and off the absorption. As the temperature increases, the required gate voltage to achieve a similar modulation depth increases by almost two orders of magnitude. Figure 2.8b illustrates this more clearly. Here we have plotted the absorption ratio verses gate voltage swing.[3] Even at low temperatures,

[3] Note: We have plotted the absorption ratio rather than the extinction ratio of the transmitted beam which would be much smaller for normal incident light. This is because the absorption of the transmitted beam can be significantly enhanced by integration with photonic circuits as we will illustrate later in this chapter.

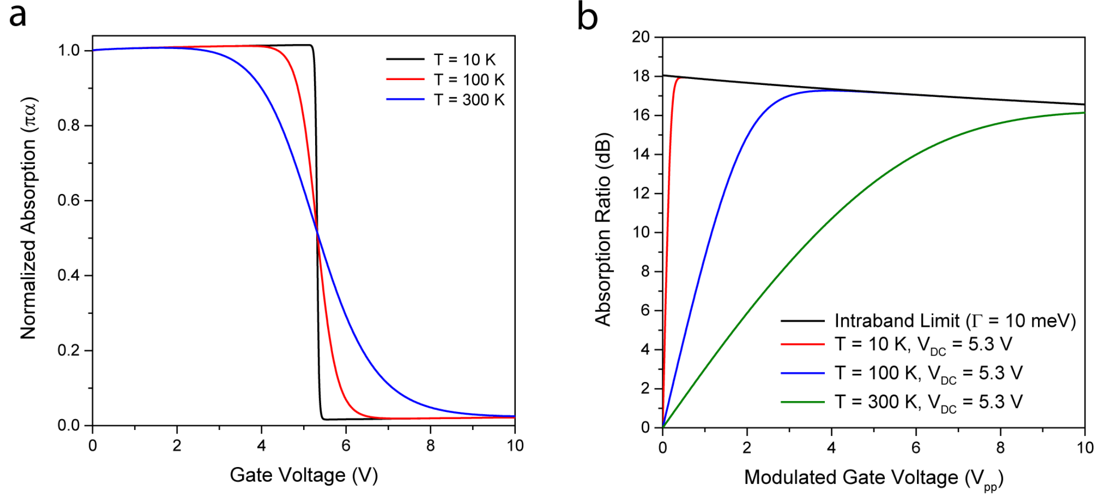

Figure 2.8: Optical modulation in uniform, undoped graphene monolayer ($\Gamma = 10\,\text{meV}$, $\omega = 0.8\,\text{eV}$, Al_2O_3 gate oxide, $t_o x = 20\,\text{nm}$). (a) Absorption (in units of $\pi\alpha$) of graphene verses applied gate voltage for various temperatures. (b) Absorption ratio verses gate voltage swing defined by $\text{Re}[\sigma(V_{\text{DC}} - V_{\text{pp}}/2)]/\text{Re}[\sigma(V_{\text{DC}} + V_{\text{pp}}/2)]$. A DC bias (5.3 V) was placed on the gate for most efficient modulation. In the absence of intraband absorption, it would be possible to completely turn off the absorption of the graphene and thus the absorption ratio would approach infinity for an ideal graphene sheet.

impurity scattering will give a finite value to σ^{intra} which will place an upper limit how well one can turn off the absorption at large gate voltages.

Now that we have provided a theoretical framework, we present the motivation, design, and experimental results of our multi-functional graphene photodetector and modulator.

2.3 Motivation

As outlined in Chapter 1, optical communication systems are constantly being miniaturized to incorporate a large number of previously discrete optoelectronic devices, together with silicon-based integrated circuits, onto a single substrate. The integration of silicon photonics demands that multiple optoelectronic functionalities be achieved with fewer complementary metal-oxide-semiconductor (CMOS) compatible materials in order to lower the cost without sacrificing performance. Chief among the building blocks of photonic systems are optical modulators and photodetectors [89–91]. These two types of devices operate based on very different mechanisms and consequently utilize different device geometries. They often have to be made of different materials that are difficult and costly to integrate with silicon photonics. Optical modulators are based on electro-optic or electro-absorptive effects in materials such as $LiNbO_3$, germanium, and compound semiconductor heterostructures. In silicon photonics, the dispersion effect induced by carrier injection or depletion is the most common method used to achieve integrated optical modulation [92, 93].

At the receiving end of optical links, photodetectors convert light back into electrical signals by absorbing photons and generating charges through photoelectric effects. Therefore, strong absorption and effective collection of photoexcited carriers are desired for efficient photodetection. Because of these distinctive requirements, no device that can function as both a photodetector and a modulator, and whose role can be switched through external control, had been made with a single type of material prior to this work. Such a simple yet multifunctional device not only can make integrated optical systems programmable and adaptable, but also could lead to novel applications such as optoelectronic oscillators and new

schemes of optical computation and signal processing.

With its remarkable optical and electrical properties, graphene has been exploited as a multifunctional optoelectronic material to achieve a plethora of optoelectronic devices with high performance [94–96], including photodetectors [23,25–29], optical modulators [62, 64], a polarizer [97], and saturable absorbers [98, 99]. All these devices, however, exploit one property or another to create a device with a single function. In this work, we fully utilize graphene's extraordinary and tunable optoelectronic properties to demonstrate the first integrated device that acts as both a modulator and a photodetector, where the functionality of the device can be controlled with an electrostatic gate also made of graphene.

2.4 Device design

2.4.1 Photonics layer

As a 2D material, it is natural to integrate graphene on a waveguide to decouple the interaction length from the material thickness. In this geometry, graphene absorbs optical power *via* the waveguide's evanescent field. In order to provide strong absorption and reduce the overall length of the device, it is desirable to maximize the evanescent field strength at the graphene layer. To do this, we use a thinned SOI wafer (110 nm silicon on 3 µm SiO_2) to fabricate single-mode TE silicon waveguides. The thin waveguides squeeze the optical mode in the vertical direction which provides less confinement and a larger evanescent field as can be seen in figure 2.9a. It is important to note that since the absorption is dependent on the in-plane electric field E_t (see equation 2.23), only E_x and E_z will contribute to the absorption. E_y as seen in figure 2.9b does not interact with the graphene sheet.

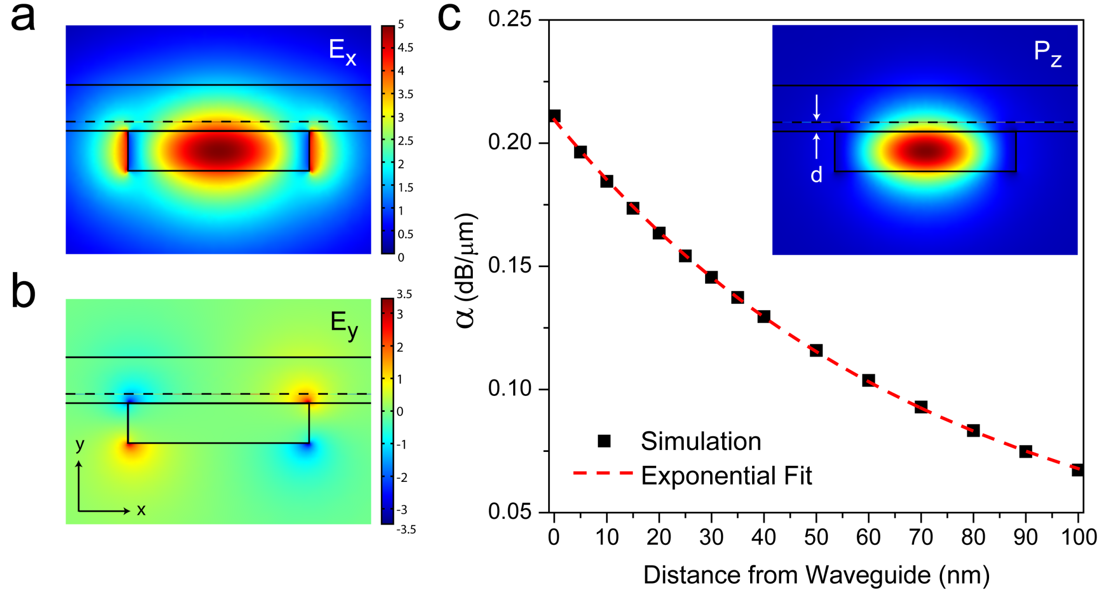

Figure 2.9: Simulated mode profiles of electric field (a) E_x and (b) E_y for a 110 nm×500 nm silicon waveguide on SiO_2 with an integrated graphene monolayer (dashed line) and an Al_2O_3 top cladding layer. (c) Optical absorption as a function of distance from the top surface of the waveguide. α decreases exponentially with distance from the waveguide as does the evanescent field. Inset is the time averaged power flow in the z-direction.

As optical power propagates along the waveguide, absorption due to graphene will cause the power to exponentially decay. If we define the z-axis as the propagation direction and P_0 as the initial optical power at $z = 0$, we can write the optical power at point z as:

$$
\begin{aligned}
P(z) &= P_0 e^{-\alpha z} \\
\alpha &= -\frac{1}{P(z)}\frac{dP(z)}{dz} = \frac{1}{P(z)}\int_L \langle Q_s \rangle \, dl
\end{aligned}
$$

where α is the power absorbed by graphene per unit length (in m^{-1}), normalized to the power in the waveguide. The absorption by the graphene layer can be calculated numerically by finding the complex effective index of the waveguide mode

using COMSOL. In these simulations, graphene was set as a conductive boundary between dielectric domains with a surface impedance of $\left(\frac{e^2}{4\hbar}\right)^{-1} = 16{,}440\,\Omega$. From the complex effective index n_{eff}, we can calculate the propagation loss α:

$$\alpha = -\frac{4\pi \text{Im}[n_{\text{eff}}]}{\lambda} \tag{2.25}$$

If we multiply α by $10\log_{10}(e)$, we can convert to dB/m. In figure 2.9c, the propagation loss (in dB/µm) is plotted for graphene at various distances from the waveguide. This distance can be precisely controlled through a planarization process (see Appendix A.1 for details) and subsequent growth of a dielectric layer such as Al_2O_3 or HfO_2 with atomic layer deposition (ALD). The evanescent field decays exponentially with increasing distance from the waveguide which is also seen in the simulated α. For our devices, graphene was placed directly onto the planarized waveguide without any dielectric spacer so the expected absorption is $\sim$0.2 dB/µm. This means we can absorb 90% of the optical power in a 50 µm long device. To measure the optical absorption precisely, we fabricated an unbalanced Mach-Zenhder interferometer (MZI) and placed the graphene absorber in one of the arms (figure 2.10). Grating couplers are used to couple light into and out of the waveguide through a fiber array. Without absorption, the output power P_{out} will be a sinusoidal function of wavelength (since the arms have difference optical lengths) with perfectly constructive and destructive interference as in figure 2.10a. The presence of absorption in one of the arms will cause partial interference at the output (figure 2.10b) and by measuring the extinction ratio of the interference fringes, the absorption in the lossy arm can be extracted.

In order to calculate the grating coupler efficiency for a given device, we need to derive a general formula for the transmission spectrum. For a simple waveguide loop with an input and output grating coupler, the grating coupler efficiency can

be calculated as follows:

$$P_{out} = \eta_{GC}^2 P_{in} \quad \Rightarrow \quad \eta_{GC} = \sqrt{\frac{P_{out}}{P_{in}}} \tag{2.26}$$

where P_{out} is taken to be the maximum of the transmission spectrum and P_{in} is the laser power. We are assuming that both grating couplers have the same coupling efficiency η_{GC}. However, this equation does not hold for a MZI if there is absorption in one arm because the maximum power transmitted by the grating couplers is not well known.

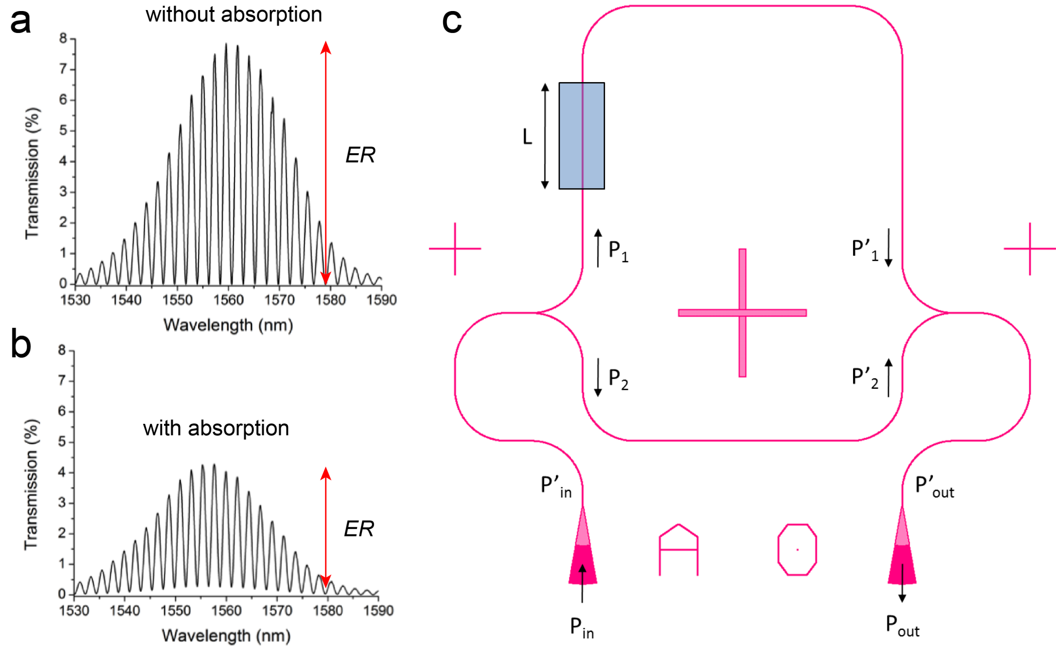

Figure 2.10: (a) Experimental spectrum of MZI without loss showing a high extinction ratio. (b) Spectrum of MZI with loss in one of the arms. The extinction ratio decreases providing a way to quantify the absorption. (c) Diagram of MZI with absorption in one arm.

Figure 2.10c shows the structure of interest with an absorbing material of length L on the upper arm (arm 1) and a shorter reference arm (arm 2). We define P'_{in} to be $\eta_{GC} P_{in}$, the power in the waveguide after the grating coupler.

There is an equal power split at both Y-junctions so the power in arm 1 and 2 before the second Y-junction can be written as follows:

$$P_1' = \frac{P_{in}'}{2} e^{-\alpha_1 l_1} = |E_1'|^2 \qquad P_2' = \frac{P_{in}'}{2} e^{-\alpha_2 l_2} = |E_2'|^2 \tag{2.27}$$

where $e^{-\alpha_1 l_1}$ and $e^{-\alpha_2 l_2}$ is the absorption in arms 1 and 2 respectively.

To take interference effects into account, we need to work with the E-fields in both arms. The E-fields can be written in the following way:

$$E_1' = \sqrt{\frac{P_{in}'}{2}} e^{-\alpha_1 l_1/2} e^{ikl_1} \qquad E_2' = \sqrt{\frac{P_{in}'}{2}} e^{-\alpha_2 l_2/2} e^{ikl_2} \tag{2.28}$$

Accounting for the 3 dB loss at the second Y-junction, P_{out}' is simply the absolute value of the sum of the E-fields squared.

$$P_{out}' = \frac{1}{2}|E_1' + E_2'|^2 = \frac{|E_1'|^2}{2} + \frac{|E_2'|^2}{2} + \frac{E_1' E_2'^*}{2} + \frac{E_2' E_1'^*}{2} \tag{2.29}$$

Substituting equations 2.27 and 2.28 into 2.29 and simplifying the result, we get the following:

$$\begin{aligned} P_{out}' &= \frac{P_1'}{2} + \frac{P_2'}{2} + \frac{P_{in}'}{4} e^{-(\alpha_1 l_1 + \alpha_2 l_2)/2} \left[2\cos(k(l_2 - l_1))\right] \\ P_{out}' &= \frac{1}{2}\left[P_1' + P_2' + 2\sqrt{P_1' P_2'} \cos(k(l_2 - l_1))\right] \end{aligned} \tag{2.30}$$

We can define the extinction ratio as the ratio of the maximum P_{out}' to the minimum P_{out}'. Since $\cos(k(l_2 - l_1))$ is limited to ± 1, the extinction ratio is:

$$ER = \frac{P_1' + P_2' + 2\sqrt{P_1' P_2'}}{P_1' + P_2' - 2\sqrt{P_1' P_2'}} \tag{2.31}$$

Combining equations 2.30 and 2.31, we can eliminate P_1' and solve for P_2':

$$P_2' = \frac{\max(P_{out}')(1 + 2\sqrt{ER} + ER)}{2ER} = \frac{\eta_{GC} \max(P_{out})(1 + 2\sqrt{ER} + ER)}{2ER} \tag{2.32}$$

Note: this equation is valid only when $P_2' \geq P_1'$ which is a reasonable assumption since the absorption in arm 1 is greater than arm 2. Now that we have P_2' in terms

of the extinction ratio and output power, both of which are measurable quantities using a photodetector, we can begin to solve for η_{GC}. Note that P_1 and P_2 are equal right after the first Y-junction. We can then write:

$$P_1 = P_2 = P_2' e^{-\alpha_2 l_2} = \frac{P_{in}'}{2} = \frac{\eta_{GC} P_{in}}{2} \tag{2.33}$$

Comparing equations 2.32 and 2.33 and assuming α_2 (the waveguide loss in arm 2) is relatively small, we can solve for η_{GC} to get an equation for the grating coupler efficiency:

$$\eta_{GC} = \sqrt{\frac{\max(P_{out})(1 + 2\sqrt{ER} + ER)}{P_{in} ER}} \tag{2.34}$$

where $\max(P_{out})$ is the peak power of the transmission spectrum and P_{in} is the input laser power.

If we substitute 2.27 into equation 2.31, we can write the extinction ratio in terms of the absorption in arm 1:

$$ER = \frac{P_{max}}{P_{min}} = \frac{1 + 2e^{-\alpha L/2} + e^{-\alpha L}}{1 - 2e^{-\alpha L/2} + e^{-\alpha L}} = \left(\frac{1 + e^{-\alpha L/2}}{1 - e^{-\alpha L/2}}\right)^2 \tag{2.35}$$

where we have assumed the absorption in arm 2 is negligible ($i.e.$ $e^{-\alpha_2 l_2} \approx 1$) and have set $\alpha_1 l_1 = \alpha L$. This provides a direct relation between a measurable quantity ER and the absorption coefficient and does not depend on the input power or the grating coupler efficiency. This is a great advantage over other methods where the coupling efficiency is often assumed from measurements on a reference waveguide which can vary significantly from the actual device under test.

2.4.2 Electronics layer

Figure 2.11a illustrates the configuration of the device which consists of two layers of graphene, separated by a dielectric layer, and integrated on a planarized

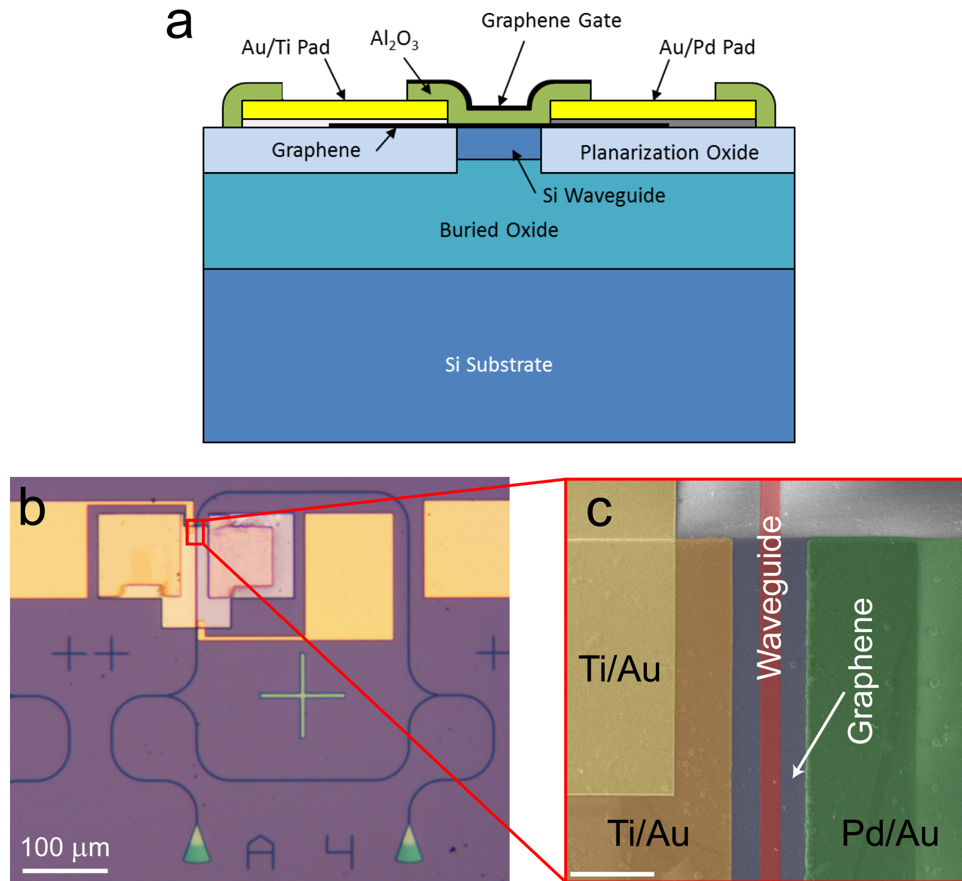

Figure 2.11: (a) Cross-sectional view of the device geometry (not drawn to scale). (b) Optical microscope image of the device. A Mach-Zehnder interferometer made of silicon waveguides is employed to accurately determine the optical absorption in graphene. Grating couplers (green triangles at the bottom) are used to couple light in and out of the device. (c) Scanning electron microscope image of the device (3 µm scale bar). Two asymmetric source and drain contacts made of titanium/gold (dark yellow) and palladium/gold (green) dope the graphene (light purple) to be n- and p-type, respectively. Contact (light yellow) to the top graphene gate is made of titanium/gold.

silicon photonic waveguide. The device is in the configuration of a simple field effect transistor (FET): the bottom layer (the channel) acts as an optical absorber and can collect photogenerated carriers, while the top layer acts as a transparent gate electrode which can tune the electrical and optical properties of the bottom graphene layer. The graphene (purchased from *Graphene Square Inc.*) is grown by chemical vapor deposition (CVD) on copper foil and transferred onto the photonic waveguide substrate using a PMMA polymer support (see Appendix A.2). The dielectric layer between the gate and the channel is 100 nm thick Al_2O_3 deposited by ALD. In order to grow relatively thick Al_2O_3, three ALD depositions of 33 nm thick Al_2O_3 were performed with cooling between depositions to prevent cracking due to accumulated film stress. The source and drain contacts on the channel are made of titanium/gold and palladium/gold, which have different work functions and dope graphene n-type and p-type, [100–103] respectively. The differential metal-graphene contacts induce a lateral p-i-n junction, if the middle of the graphene channel is tuned to charge neutral as shown in Figure 2.12b, with a built-in electrical field in the channel. This field facilitates the separation and drift of the photogenerated electrons and holes. This allows the device to generate a net photocurrent without the application of a bias voltage and with a higher efficiency than with a single-sided configuration [26, 27].

Figure 2.11b and c shows the optical and scanning electron microscope images of a typical device. To most accurately measure the net optical absorption of graphene and determine the performance, the device is embedded in one arm of an unbalanced Mach-Zehnder interferometer so that the absorption coefficient of graphene can be unambiguously determined [13]. A pair of grating couplers with efficiency of $\sim$20% each are integrated with the interferometer to couple light in and out with optical fibers.

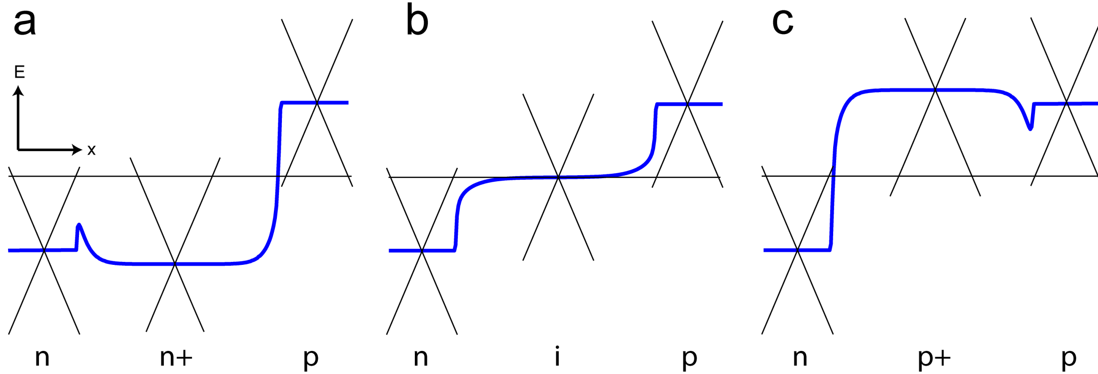

Figure 2.12: Illustration of the field profile across the graphene channel with zero applied bias voltage highlighting the built-in electric field at (a) n+, (b) intrinsic, and (c) p+ doping levels.

2.5 Results

2.5.1 Modulation

The FET configuration allows us to characterize the electrical properties of the graphene channel. Figure 2.13a shows the resistance of the channel when the gate voltage is scanned. The results show that the charge neutrality point (CNP) is reached when a gate voltage of $V_G = +33\,\text{V}$ is applied, indicating that the graphene channel is heavily p-doped with a hole concentration of $p = 1.4 \times 10^{13}\,\text{cm}^{-2}$ and a corresponding Fermi level of $E_F = -0.45\,\text{eV}$. This level of doping is relatively high for graphene grown by CVD method and can be attributed to the trapped positive charges at the dielectric interface. Fitting the resistance vs V_G results in an extracted carrier mobility in the graphene of $1150\,\text{cm}^2/\text{V}{\cdot}\text{s}$, which is relatively low and attributed to disorder introduced by Al_2O_3 deposition and charge trapping in the dielectric. Recent results of room temperature mobility up to $1.4 \times 10^5\,\text{cm}^2/\text{V}{\cdot}\text{s}$ obtained from graphene on boron nitride [10] are very encouraging to improve the device performance demonstrated here.

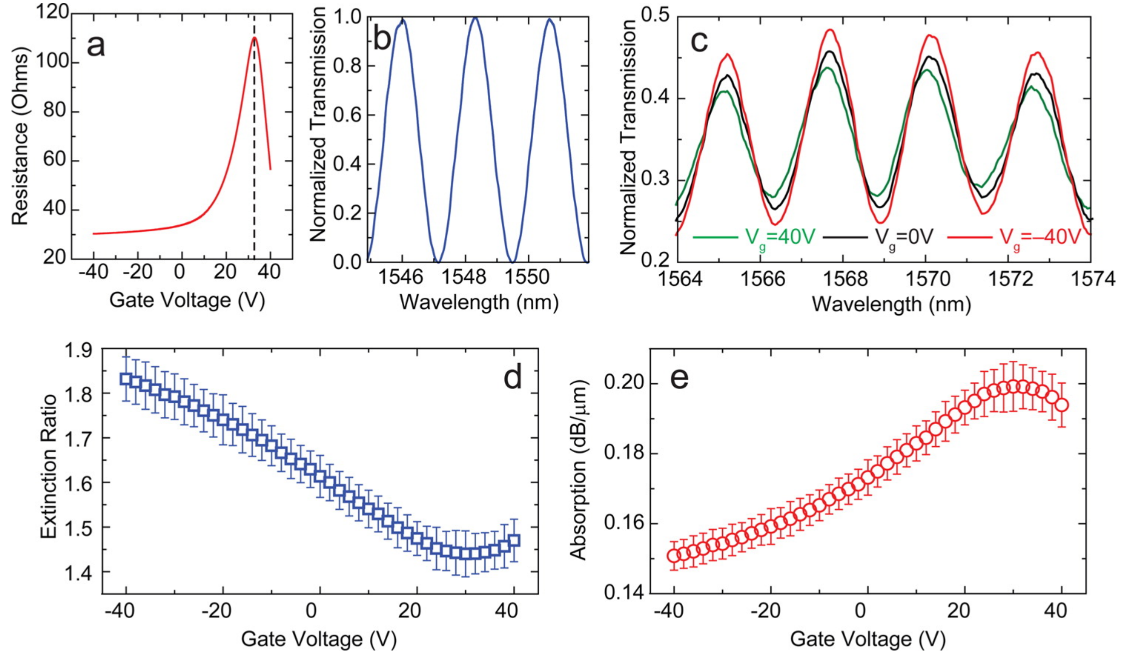

Figure 2.13: Gate tuned optical absorption and optical modulation. (a) Source-drain resistance of the graphene channel versus the voltage applied to the top graphene gate. The charge neutral point (CNP) is reached at +33 V, indicating the graphene as-transferred is highly p-type. (b) Interference fringes measured from the silicon waveguide Mach-Zehnder interferometer just before the graphene layers were transferred. A very high extinction ratio (> 40 dB) indicates very low optical loss (< 0.1 dB) in the waveguide. (c) Interference fringes measured after the graphene device was completed and different gate voltages were applied. The extinction ratio decreased (increased) when +(−)40 V was applied. (d) Measured interference extinction ratio at various gate voltages. (e) The absorption coefficient in the graphene channel calculated from the extinction ratio at various gate voltages and excluding absorption in other parts (top graphene gate and metal contacts) of the devices. The absorption coefficient can be modulated from 0.2 dB/μm at $V_G = +33$ V to 0.15 dB/μm at $V_G = -40$ V. The corresponding modulation depth of the transmission in the waveguide is 64%.

Figure 2.13b shows the transmission spectrum of the Mach-Zehnder interferometer before the graphene layers were integrated on the waveguide. The interference fringes show an extinction ratio higher than 40 dB ($ER = T_{max}/T_{min}$, T_{max} and T_{min} are the transmission at the peaks and valleys, respectively), confirming that there is negligible excess optical loss (less than 0.1 dB) in the interferometer arms. During the fabrication of the device, the ER of the interferometer was measured after every step so that the optical loss contributed by each of the layers in the device can be accounted for. When the device was completed, the ER decreased to 1.6 when zero gate voltage was applied, corresponding to an added loss of 18 dB in the device arm. The major contribution to the optical loss is from the bottom layer of graphene that is directly above the waveguide, rather than from the top layer of graphene or the metal contact pads which are 1 µm away from the sides of the waveguide. When voltage was applied to the top graphene gate, the extinction ratio of the interference fringes was modulated, as shown in Figure 2.13c. We observed that the ER increased (decreased) when negative (positive) gate voltage was applied, indicating reduced (enhanced) absorption in the graphene. We measured the ER at every step of the applied gate voltage and calculated the linear absorption coefficient in the bottom graphene layer, as shown in Figure 2.13d and e. The results show that the absorption coefficient can be modulated from a peak value of 0.2 dB/µm near CNP to 0.15 dB/µm, i.e., 25% of modulation, when $V_G = -40\,\text{V}$ is applied. If the device is used as a modulator, the corresponding modulation depth of the optical intensity in the 90 µm long waveguide is 64%.

The change of absorption in graphene can be explained by the modulated Fermi level and the interband transition rate [20, 21, 104]. At $V_G = -40\,\text{V}$, the Fermi level in the channel graphene is expected to be $E_F = -0.69\,\text{eV}$. Thus, for

photon energy of 0.8 eV ($\lambda = 1.55\,\mu$m), interband absorption decreases as shown in Figure 2.13e.

Based on our theoretical analysis in section 2.4.1 which takes into account intraband absorption, we expect that the absorption coefficient should able to be tuned to a few percent of the peak value. However, in our devices, the measured absorption coefficient at room temperature remains at 75% of the value at CNP, leading to a high insertion loss of the modulator. One possible source of the higher-than-expected absorption could be charge trapping in the Al_2O_3 dielectric that counteracts that action of gate voltage, particularly at very negative voltages. In addition, phonon-assisted midgap absorption in graphene has recently been suggested to contribute a significant amount (20-25%) of the total absorption in graphene and thus can be another source of the high residual absorption [105]. Both of these sources of absorption are expected to be significantly reduced by using boron nitride cladding layers for the graphene. Our results of gate-modulated optical absorption in graphene also agree well with that of previous waveguide integrated graphene modulators [62, 64]. We note that the interferometer configuration employed in this work unambiguously rules out the unvaried optical losses contributed from other parts of the device so that the tunable and residual parts of the absorption in the graphene can be determined and analyzed in more detail.

2.5.2 Photodetection

The strongly tunable optical absorption demonstrated above stems from the interband transition in graphene which at the same time generates photocarriers able to be collected so that both photodetection and optical modulation can be achieved with the same device. This type of dual-functionality has not been realized with any other optoelectronic material to our knowledge. To characterize

the photoresponse, we measured the source-drain current with optical input while the gate voltage was varied. As shown in Figure 2.12b, the differential metal contacts induce a built-in internal field in the graphene channel, especially when the graphene is at the CNP, which facilitates the separation of photocarriers and generates a net photocurrent. Figure 2.14a plots the measured photocurrent with zero source-drain bias and input optical power of 12 dBm ($\approx 1\,\mathrm{mW}$ in the waveguide) while the gate voltage was scanned. As expected, peak photocurrent was obtained very close to the CNP (the actual CNP drifts because of the slowly time-varying trapped charges at the graphene-dielectric interface). For comparison, the gate tuned absorption coefficient is also plotted in Figure 2.14a. It appears that the peak of the photocurrent is much sharper than the absorption, indicating that in addition to modulating the absorption, the gate voltage also modulates the collecting efficiency of photocarriers by changing the field distribution in the channel. At the CNP, the built-in field can penetrate across the channel and the electron-electron scattering of the photocarriers is at a minimum. The sign of the photocurrent changes twice when the graphene is tuned from n-doped to heavily p-doped. This is consistent with the results from graphene photodetectors for normal incident light and can be explained by the contribution of photocurrent from both photovoltaic and photothermoelectric effects [35, 79, 83, 85]. The photo-voltaic current dominates when the doping in the graphene is low, while the photothermoelectric current dominates at high doping regimes and has an opposite sign to the photovoltaic current, consistent with our theoretical discussion in section 2.1.

Knowing graphene's absorption coefficient α and thus the actual optical power absorbed in the graphene, the internal quantum efficiency η of the photodetector can be determined by $\eta = I_p h\nu / eP_0(1 - e^{-\alpha L})$, where I_p is the photocurrent,

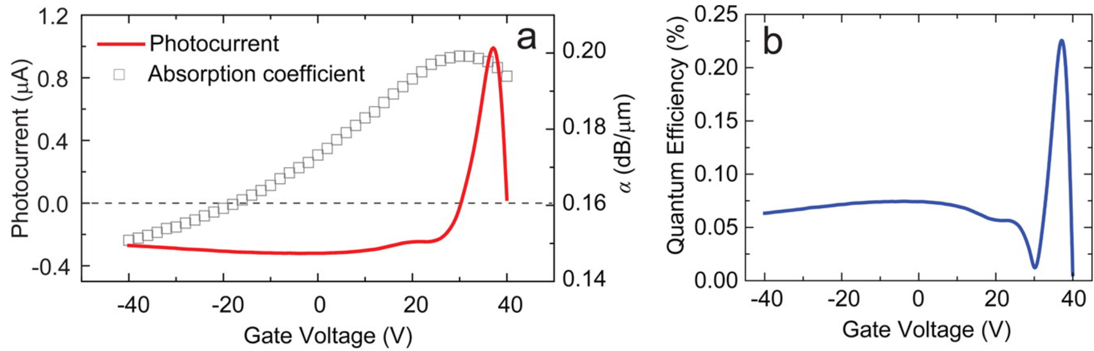

Figure 2.14: Gate tuned photodetection with graphene. (a) Measured zero-bias photocurrent and graphene absorption coefficient at various gate voltages. The photocurrent peaks at the charge neutral point and changes sign twice when the gate voltage is scanned from negative to positive, indicating both photovoltaic and photothermoelectric contributions. (b) Calculated quantum efficiency of the graphene photodetector. A maximum efficiency of 0.25% was reached at CNP.

$h\nu$ is the photon energy, e is the electron charge, P_0 is the input optical power, and L is the length of the graphene detector. The result is plotted in Figure 2.14b. A maximal total quantum efficiency of 0.25% and detector responsivity of 3.6 mA/W was obtained at the CNP. This photodetection responsivity was among the highest value achieved at the time with single-layer, CVD-grown graphene. We note that although an internal efficiency of 6-16% was estimated in graphene under a high internal field which exists in the region very close to the metal contacts, the efficiency measured here is an averaged value across the 2.5 μm long graphene channel where the field is nonuniform and thus has a more practical meaning.

To improve the quantum efficiency, it is essential to improve the efficiency of separating photocarriers which requires a higher carrier mobility and a stronger internal field. The former can be obtained with high quality graphene like what has been realized in 2D heterostructures of boron nitride and graphene [10] with reduced phonon-assisted scattering. Although zero-bias operation has zero dark

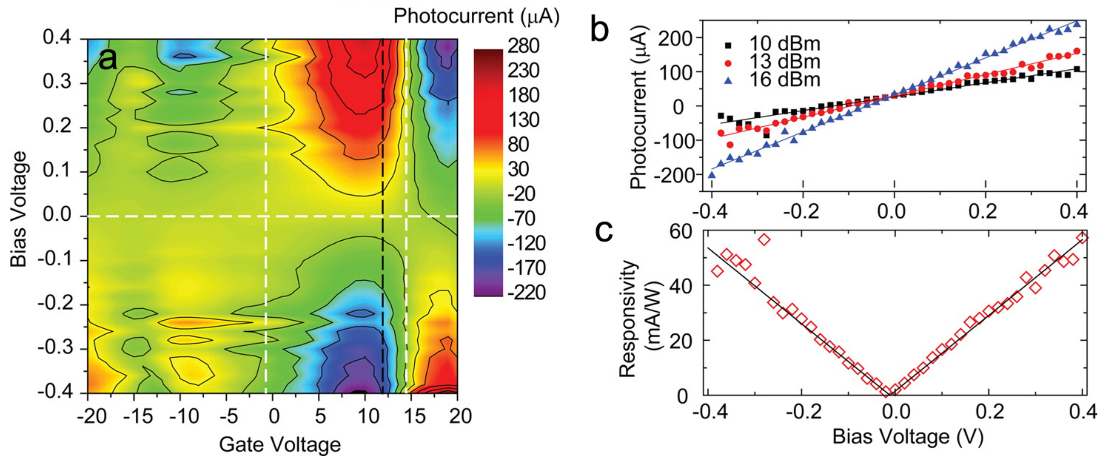

Figure 2.15: (a) Two-dimensional plot of photocurrent measured from a different device when both gate and bias voltages are scanned. A 6-fold change of the photocurrent direction can be observed. This can be explained by the dominance of bolometric effect in high doping regime and photovoltaic effect in the low doping regime, respectively. A black dashed line marks the CNP, and white dashed lines are guides to the eyes demarcating the regions of positive and negative photocurrent. (b) Photocurrent versus bias voltage at various input optical power and (c) detector responsivity versus bias voltage measured with the gate voltage at +9 V near CNP. A maximal responsivity of 57 mA/W was measured at a moderate bias voltage of 0.4 V.

current and is advantageous for low noise detection, application of a bias voltage between source and drain provides a stronger field in the channel which can significantly improve detection efficiency. Figure 2.15c shows a 2D plot of the photocurrent measured with a different device (with the CNP closer to $V_G = 0\,\mathrm{V}$) when both gate and bias voltages were scanned. A 6-fold sign change of the photocurrent is observed, consistent with previous results obtained in normal incidence devices [79]. At high doping and large bias, the photocurrent is dominated by the bolometric effect which has an opposite sign to the photovoltaic current which dominates at the low doping, low bias regime. In this device, the responsivity, dominated by photovoltaic current, reaches 57 mA/W at a moderate

bias voltage of 0.4 V and near CNP with a gate voltage of 9 V, as shown in Figure 2.15d and e. This external responsivity was determined from measured photocurrent and the optical power in the waveguide under the graphene photodetector after accounting for the loss at the grating coupler and the first splitter of the interferometer.

2.5.3 Simultaneous Operation

We have demonstrated a novel multifunctional optoelectronic device based on graphene and integrated on a photonic waveguide that can be operated as both an optical modulator and a photodetector and can be tuned with a gate voltage. Further observation of figure 2.14a reveals that the optical absorption and the photocurrent are simultaneously modulated by the gate voltage. While the photocurrent should be proportional to the absorbed optical power and thus approximately the absorption coefficient, it is also sensitive to the field distribution in the graphene channel which is modulated by the gate. Thus, the device can be operated in an unprecedented mode of simultaneous optical modulation and photodetection: the transmitted optical signal will be modulated by the gate voltage, while the photocurrent measured at the same time is proportional to the absorbed optical power; thereby its phase is opposite to the modulated optical signal. Thus, this novel modulator–detector provides an in situ feedback of the optical modulation which can, for example, be utilized to build an optoelectronic oscillator [106] with both electrical and optical outputs. In Figure 2.16a, both the transmitted optical intensity and the photocurrent are modulated by a 100 kHz sinusoidal signal of 2 V peak-to-peak amplitude applied to the gate. The optical transmission is clearly modulated out-of-phase with the simultaneously measured photocurrent. The speeds of graphene-based modulators and photodetectors are expected

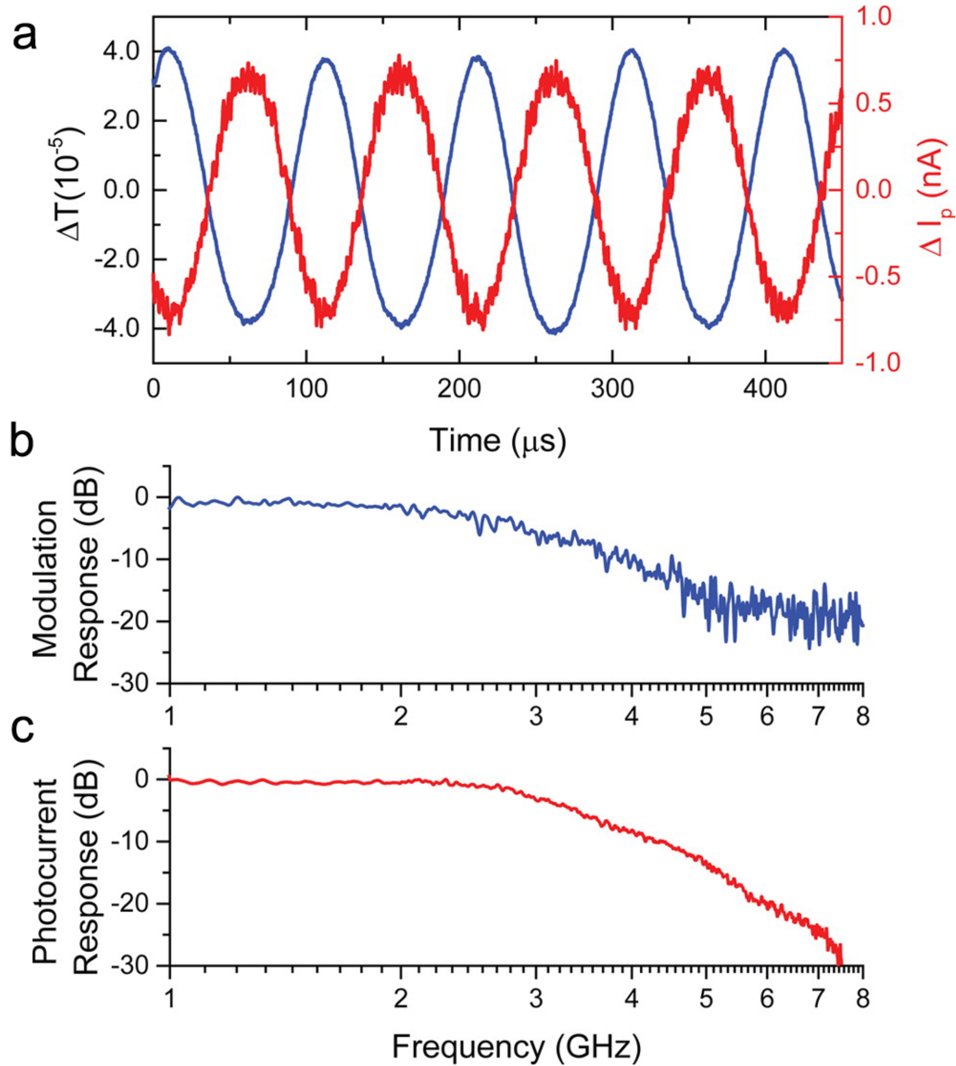

Figure 2.16: Simultaneous optical modulation and photodetection. (a) Transmitted optical signal (blue trace) and photocurrent (red) measured simultaneously when a 100 kHz sinusoidal voltage of 2 V peak-to-peak was applied to the gate. It is clear the photocurrent modulation, which should be proportional to optical absorption in graphene, is out-of-phase with the optical transmission. (b and c) Frequency response of optical modulation (b) and photocurrent (c). The 3 dB bandwidth of the device is determined to be 3 GHz for photodetection and 2.5 GHz for modulation. Both are limited by the RC time constants of the contact pads and gate capacitance in the device.

to be very high with an intrinsic bandwidth estimated to approach 500 GHz [25] and 120 GHz [63], respectively. Figure 2.16b and c shows the measured frequency response of optical modulation and photodetection, respectively. The 3 dB bandwidth of the device was measured to be 3 GHz for photodetection and 2.5 GHz for modulation. The experimental modulator and detector bandwidths are expected to be RC limited due to a large contact resistance and capacitance in our device. If we take into account the extra overlapping area seen in figure 2.11c (about 5 µm), we get an estimated RC limited bandwidth of ~7 GHz and 3.5 GHz for the photodetector and modulator respectively. The higher detector bandwidth compared to the modulator is expected since the modulator has a higher RC time constant due to the added resistance of the top graphene layer. Previous work has shown that using an optimized device geometry, and with improved, but still achievable, graphene mobility and contact resistance, modulator bandwidths as high as ~100 GHz are possible [63].

2.6 Conclusion

In conclusion, a multifunctional, waveguide integrated, and gate tunable graphene optical modulator and photodetector has been demonstrated. Using CVD grown monolayer graphene, high modulation depth and detector responsivity have been achieved in a device with a compact footprint. The performance is limited by the relatively low quality of the graphene that is used in the device and can be expected to improve dramatically by leveraging the latest research on heterostructures of graphene and other two-dimensional materials. Nevertheless, the demonstration that multiple optoelectronic functionalities can be obtained in a single device of one material is unprecedented and could open the door to many future applications

in integrated optoelectronics. In particular, the simplicity and the compatibility of the process to integrate graphene is very promising for large-scale integrated silicon photonics.

Chapter 3

Black Phosphorus Photodetector

In the previous chapter, we showed how graphene could be utilized for both photodetection and modulation in the near-IR when integrated on a silicon waveguide. However, because graphene lacks a bandgap, graphene photodetectors suffer from very high dark current. In contrast, layered black phosphorous, a recent addition to the family of two-dimensional materials, is ideal for photodetector applications due to its narrow but finite bandgap. Here, we demonstrate a gated multilayer black phosphorus photodetector integrated on a silicon photonic waveguide operating in the near-infrared telecom band. In a significant advantage over graphene devices, our black phosphorus photodetectors can operate under bias with very low dark current and attain an intrinsic responsivity up to 135 mA/W and 657 mA/W in 11.5-nm- and 100-nm-thick devices, respectively, at room temperature. The photocurrent is dominated by the photovoltaic effect with a high response bandwidth exceeding 3 GHz.

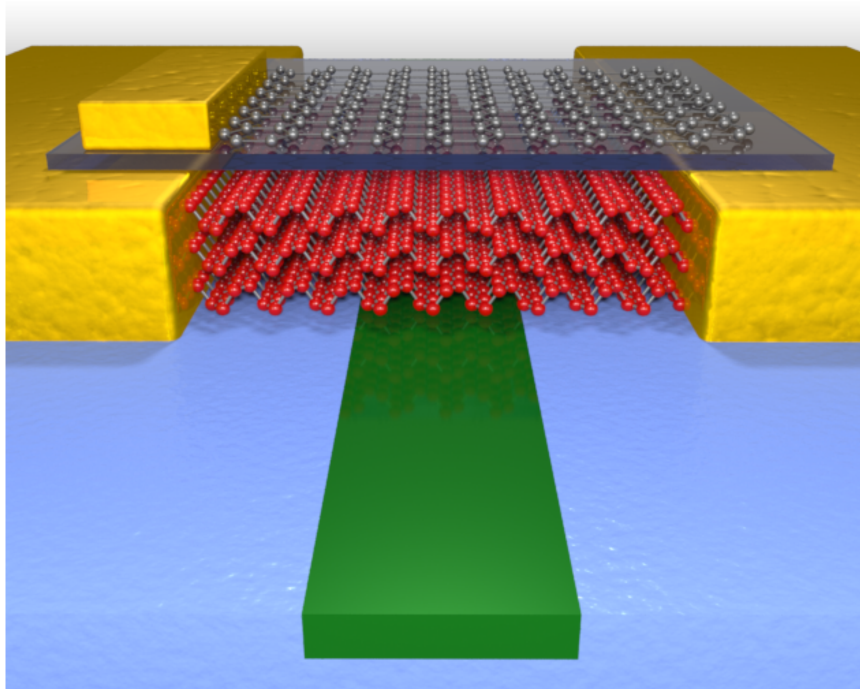

Figure 3.1: 3D illustration of BP photodetector integrated on a silicon waveguide. The top graphene layer serves as a transparent gate electrode.

3.1 Introduction

Graphene, the most extensively investigated two-dimensional material, has many novel optical properties, including a tunable interband transition and saturable absorption, and has potential for a wide range of optoelectronic applications [94,95]. However, one important optoelectronic device application where graphene is severely limited is in photodetection. Although graphene has demonstrated broadband optical absorption, an ultrafast photoresponse and reasonable responsivity [25–27, 29], graphene photodetectors have a very high dark current when they are operated in photoconductive mode where a bias voltage is applied to attain high responsivity [27, 79]. This is a direct result of the lack of a bandgap in graphene and is illustrated in figure 3.2. This high dark current leads to high

shot noise, the dominant noise source at low levels of light, and thus sets the noise floor of the photodetector at a high level. Other two-dimensional materials such as layered transition-metal dichalcogenides (TMDCs) have relatively large bandgaps, so they do not absorb at the important telecom wavelengths [107–110].

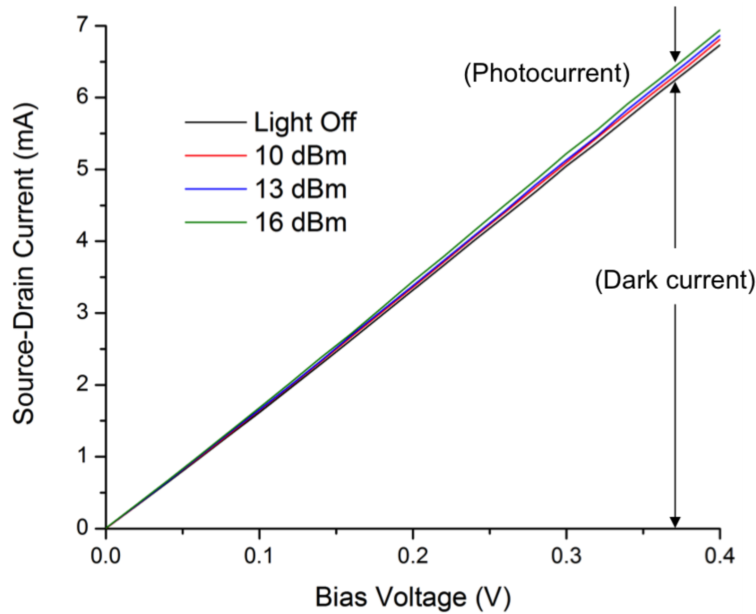

Figure 3.2: Dark current in graphene device from chapter 2. In this case, the dark current is many times greater than the observable photocurrent.

Black phosphorus (BP) is a layered crystal of phosphorus that is stable at room temperature. It has recently been the subject of interest after experiments showed that few-layer and monolayer flakes can be exfoliated in a similar manner to graphene [45, 54, 111]. In contrast to graphene, however, BP has a direct bandgap that is predicted to be 1.8–2 eV for the monolayer. As the number of layers increases, the bandgap reduces and eventually reaches ∼0.3 eV in bulk [14, 112]. Such a layer-tunable bandgap covering the visible to mid-infrared spectral range suggests that BP is a very promising two-dimensional material for

broadband optoelectronic applications [41, 47–49]. BP has also shown excellent electrical properties, including a high hole mobility up to $1350\,\mathrm{cm^2/V{\cdot}s}$ at room temperature, an on-off ratio up to 10^5 , and good current saturation in field-effect devices [45, 54, 111, 113]. In this chapter we integrate a few-layer BP photodetector into a silicon photonic circuit, which also enables quantitative measurement of the absorption and quantum efficiency of BP in the telecom band (∼1.55 µm). Operated in the photoconductive mode, high responsivity, high internal quantum efficiency, and operation at bit rates above 3 Gbit/s are achieved with very low dark currents.

3.2 Device fabrication

To most efficiently utilize the optoelectronic properties of two-dimensional materials, it is necessary to integrate them on planar photonic devices so that the optical interaction length is not bound by the thickness of the materials [27, 29, 31, 114–116]. Similar to the previous chapter, BP photodetectors were fabricated using SOI wafers (SOITEC) with a 110 nm top silicon layer and 3 µm buried oxide layer. The underlying photonics layer was patterned using electron-beam lithography (Vistec EBPG 5000+) with maN-2403 resist and etched with a standard silicon Bosch process to define the photonics layer. Electron-beam evaporation was then used to deposit 140 nm SiO_2 on the sample using the remaining electron-beam resist as a mask. After removing the resist in N-methylpyrrolidone (NMP) with an ultrasonic bath, the planarized substrate was annealed using rapid thermal annealing (RTA) at 1100 °C for 1 minute to improve the quality of the evaporated oxide (see Appendix A.1 for details). A 10 nm layer of HfO_2 was grown with ALD to protect the photonics layer from subsequent etching processes.

Exfoliated BP (purchased from Smart Elements GmbH) was transferred to the planarized photonics layer with the wet transfer method described in [117] (see Appendix A.3 for transfer recipe). Care was taken to prevent the BP from making contact with the water. Photolithography and a dry etch step were used to remove unwanted material from the waveguides. Shipley S1800 series photoresist was used to protect the BP channel material during the dry etch. Source and drain contacts were defined with electron-beam lithography using poly(methyl methacrylate) (PMMA), and 5 nm Ti/50 nm Au was deposited using electron-beam evaporation at 100 °C. A 20 nm ALD Al_2O_3 gate dielectric/passivation layer was then grown at 250 °C. The top few-layer graphene gate was transferred using the same wet transfer method and patterned with electron-beam lithography and oxygen plasma etching. Finally, top-gate contacts were patterned using Poly(methyl methacrylate) (PMMA), and 5 nm Ti/30 nm Au was deposited with electron-beam evaporation.

The crystal orientation of the BP flakes were determined with polarization-dependent Raman spectroscopy after transfer. Due to the nature of the fabrication process, the orientation could not be determined until after the transfer, leading to less than optimal crystal orientations. Figure 3.3 shows the polarization dependent Raman spectra we observed for the devices presented. The spectra are normalized to the out-of-plane A_g^1 peaks since they should be independent of in-plane polarization. We can determine the crystal orientation based on the relative ratio of the B_{2g} peak (zigzag direction) to the A_{2g} peak (armchair direction). The polarization angle is relative to the flow of carriers in the channel. Therefore, we can see that the BP for the 100 nm device is oriented with the armchair axis parallel to the flow of carriers in the channel, while for the 11.5 nm device, the armchair axis is perpendicular to the direction of carrier flow. According to [54]

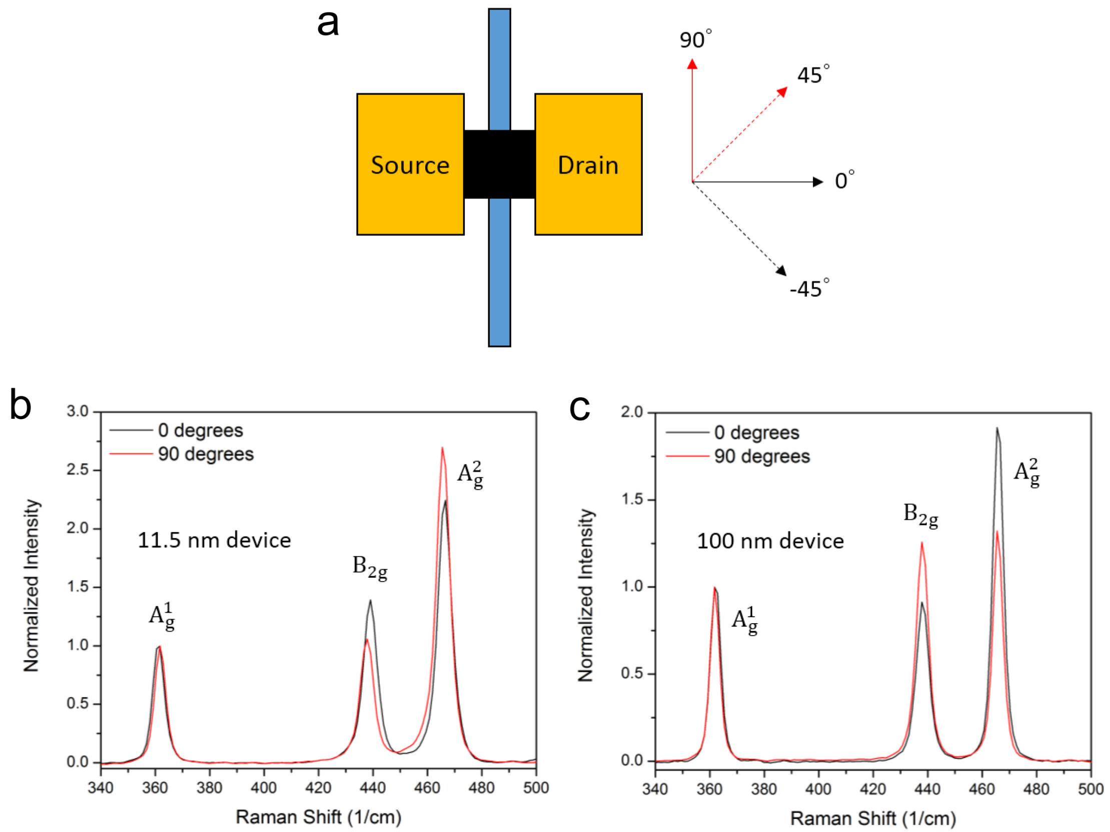

Figure 3.3: Polarization-dependent Raman spectra used to determine the crystal orientation of the transferred flakes with respect to the waveguide. (a) Geometry used to determine crystal orientation (0 degrees corresponds to Raman excitation polarized along the direction of carrier flow in the channel). Spectra of (b) 11.5 nm and (c) 100 nm devices are normalized to the out-of-plane A_g^1 peaks which should be polarization independent.

and [48], the armchair direction has the greatest optical absorption and highest carrier mobility. Therefore, the crystal orientation of the 100 nm device is optimally aligned for maximal mobility and absorption while the 11.5 nm device is not.

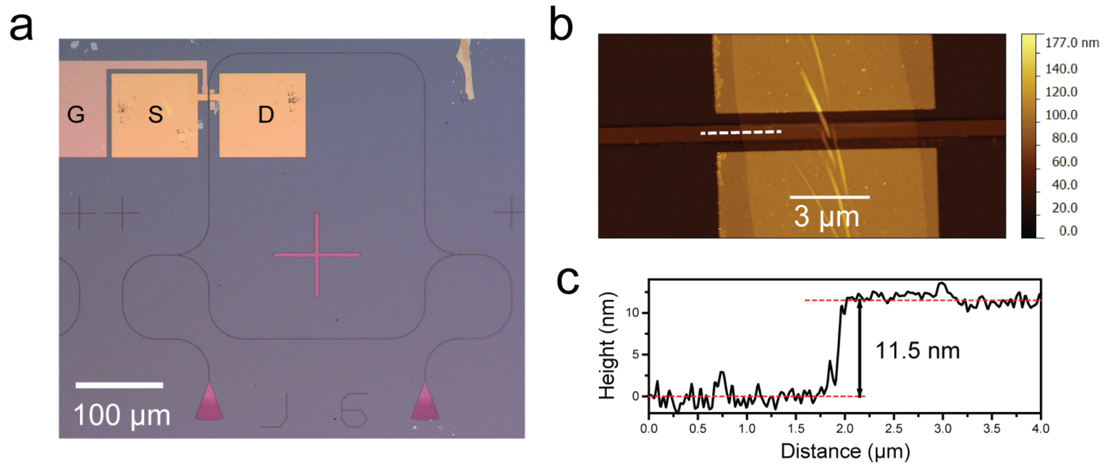

Figure 3.4: Optical and AFM images of completed BP photodetector. (a) Microscope image of BP photodetector integrated in a Mach-Zehnder interferometer. The gate, source, and drain which make up the three terminal device are labeled in the figure. (b) AFM image of the BP flake before the top gate is added. The BP can be clearly seen intact across the waveguide with a few wrinkles remaining from the transfer process. White dashed line corresponds to the height profile in (c) where the flake is measured to be 11.5 nm (*i.e.* 23 layers) thick.

We integrated a BP FET on a silicon photonic waveguide using few-layer graphene as the top-gate. In this way, the carrier type and concentration in the BP layer can be electrostatically tuned, allowing the mechanism of photocurrent generation to be investigated and the performance of the device to be optimized. Figure 3.4a shows an optical image of the complete device. The silicon photonic circuit patterned on the SOI substrate includes a Mach-Zehnder interferometer (MZI), which allows the absorption in the BP to be quantitatively measured in order to unequivocally determine the intrinsic responsivity and internal quantum

efficiency [31, 114], which are more useful than the extrinsic values in revealing BP's true potential for optoelectronic applications. Figure 3.4b presents an atomic force microscope image of the BP layer transferred onto the waveguide after deposition of source and drain contacts made of Ti (5 nm) and Au (50 nm). The width of the BP is 6.5 µm and the thickness was determined to be 11.5 nm from the profile in figure 3.4c, indicating it is composed of about 23 layers.

During each step of fabrication the transmission spectrum of the MZI was measured (figure 3.5). From the extinction ratio (ER) measured from the interference fringes in the spectra, the absorption loss in the measurement arm of the MZI can be determined using the relation $\mathrm{ER} = (1 + e^{-\alpha L/2})^2/(1 - e^{-\alpha L/2})^2$, where α is the absorption coefficient and L is the width of the BP FET (see section 2.4.1 for details). The results are shown in figure 3.5. From measurements taken after transfer of the BP and deposition of the top-gate dielectric, we determined that the absorption coefficient in the BP in the device is 0.182 dB/µm. This result confirms that few-layer BP has strong absorption in the near-infrared, as expected from its narrow bandgap [41]. The 6.5-µm-long device absorbs 78.7% of the optical power in the waveguide, of which 17.5% is absorbed by the BP and the rest by the graphene top-gate, which is the main cause of loss. However, such a top-gate is unnecessary in practical devices if the initial doping in the BP can be optimized, for example, by chemical doping.

To compare the measured optical absorption of BP with the expected theoretical absorption, we performed cross-section analysis using the FEM software COMSOL (see section 2.4.1 for discussion on calculating loss due to 2D material integrated on a waveguide). The waveguide supports a single, quasi-TE mode as expected, with the maximum electric field in x-direction. According to [50], the optical conductance is anisotropic in multilayer black phosphorus, so the relative

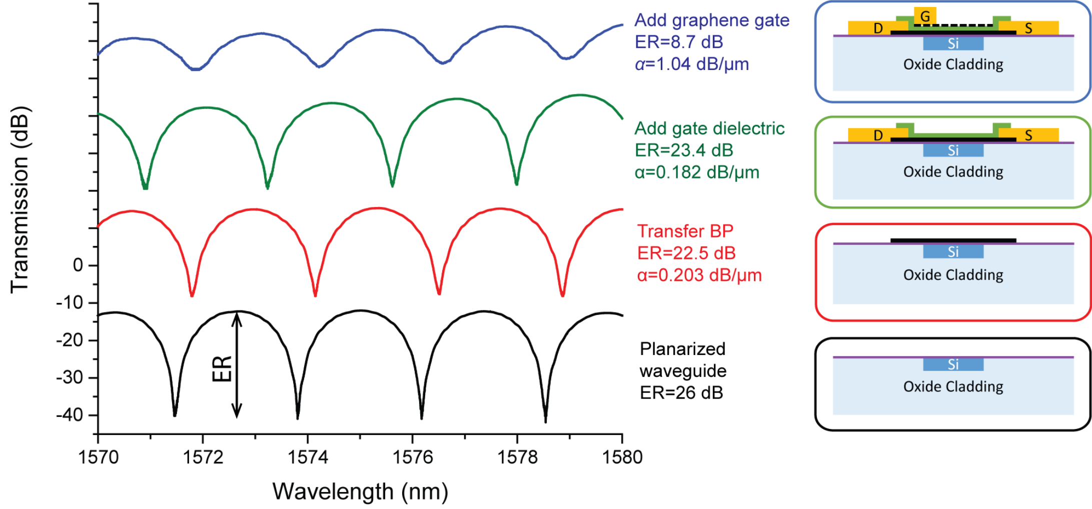

Figure 3.5: Evolution of transmission spectrum of Mach-Zehnder interferometer during the fabrication process. Traces on the left correspond to fabrication steps on the right. From the extinction ratio, the absorption coefficient of each added layer can be determined. With this method, the absorption coefficient in the BP in the completed device is determined to be 0.182 dB/µm.

orientation between maximum absorption and the strongest electric field needs to be considered in this simulation.

When simulating 11.5 nm thick black phosphorus, we used the complex refractive index ($n_{xx} = 3.16+0.0623i$, $n_{yy} = 2.83$, $n_{zz} = 3.54+0.135i$) which corresponds to the predicted optical conductivity of a 10 nm thick flake [50, 118] ($\sigma_{xx} = 0.7\sigma_0$, $\sigma_{yy} = 0$, $\sigma_{zz} = 1.7\sigma_0$, where σ_0 is the universal conductivity of graphene). This orientation means we have the weakest absorption since the electric field maxima and the material absorption maxima are orthogonal. The mode profile is shown in figure 3.6a and the calculated absorption is 0.198 dB/µm which is quite close to our experimental result of 0.182 dB/µm. This configuration matches our predicted crystal orientation from the Raman data presented.

As the thickness of black phosphorus approaches bulk, the optical conductivity

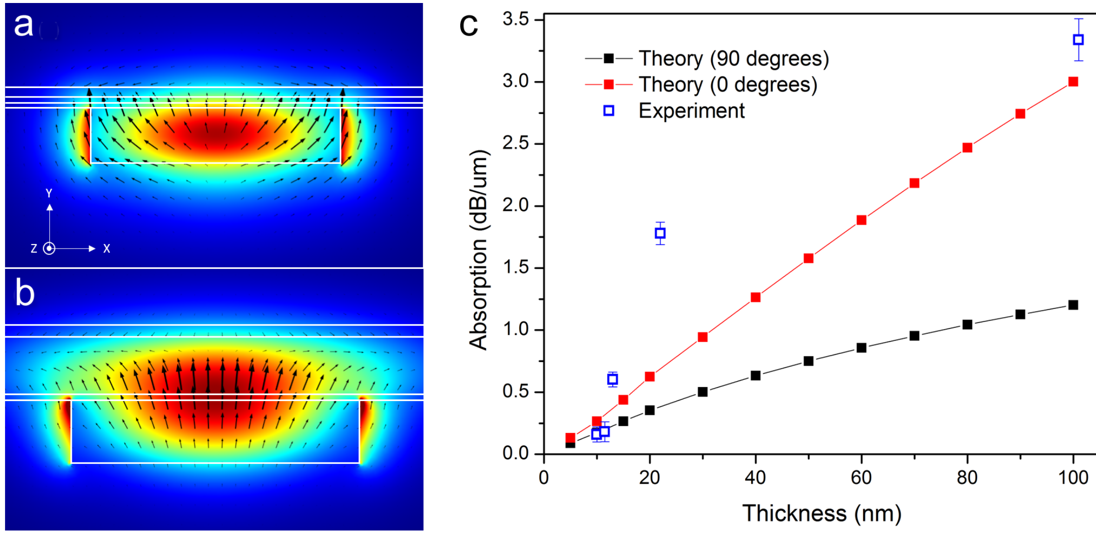

Figure 3.6: Waveguide cross-section of electric field intensity distribution and power flow represented by arrows (not to scale) for: (a) 11.5 nm thick BP and (b) 100 nm thick BP. Layers from top to bottom: ALD deposited Al_2O_3, black phosphorus, HfO_2, Silicon waveguide. (c) The calculated upper and lower limit of absorption in black phosphorus of different thickness in two different orientations (0 degrees = armchair axis along the x-direction) with data from five fabricated devices. Closer examination of the 22 nm device revealed other BP debris touching the waveguide, thus contributing additional absorption loss.

changes slightly for 1.55 µm wavelengths. When simulating black phosphorus flakes with 20 nm to 100 nm thicknesses, we used a fixed complex refractive index ($n_{xx} = 3.54+0.159i$, $n_{yy} = 2.83$, $n_{zz} = 3.16+0.0623i$) which corresponds to optical conductivity of a 20 nm flake [50] ($\sigma_{xx} = 4.1\sigma_0$, $\sigma_{yy} = 0$, $\sigma_{zz} = 1.4\sigma_0$). We also rotated the crystal orientation by 90 degrees to match the Raman results for the 100 nm thick device. This orientation should produce the maximum absorption. Shown in figure 3.6b, the absorption of a 100 nm flake was found to be 3.15 dB/µm which is comparable to our experimental result of 3.34 dB/µm. When solving for the waveguide mode, we see that the mode actually begins to be guided in the bulk black phosphorus layer when its thickness is comparable to 120 nm thick silicon

waveguide. This leads to a significant enhancement of absorption. The absorption per unit length for the 100 nm device is double that which is achievable (around 1.7 dB/µm) in a typical germanium waveguide photodetector [119].

To account for both orientations, we calculated the theoretical upper and lower limit of the optical absorption coefficient as a function of thickness as shown in figure 3.6c. We also included the absorption data of 5 devices with various thicknesses. It is worth noting that on closer inspection the 22 nm device was found to have extra debris touching the waveguide which contributes additional absorption loss to the waveguide mode.

3.3 Results

We first performed field-effect transport measurements of the device to characterize its electrical properties. Two Keithley 2400 series source meters were used for electrical measurements, one to control the gate voltage and the other to bias the device while measuring the source-drain current. The source-drain current I_{DS}, measured while sweeping the gate voltage V_{G} at various fixed bias voltages V_{DS}, is shown in figure 3.7a. The minimum conductance point at $V_{\mathrm{G}} = -7\,\mathrm{V}$ reveals that the BP is n-doped with an electron concentration estimated to be $1.6 \times 10^{13}\,\mathrm{cm}^{-2}$. We have consistently found that in devices using top-gates with an Al_2O_3 gate dielectric grown by atomic layer deposition (ALD), the BP is n-doped. This contrasts with the p-doped BP observed in most back-gated devices reported in the literature to date [45, 54, 111], and in devices that we have made using HfO_2 as the top-gate dielectric. We therefore speculate that the doping type and level in BP are sensitive to the types of dielectric layers above and below the BP as well as the deposition conditions of those layers. This relationship will require more

systematic studies to draw meaningful conclusions but is not the focus of this work.

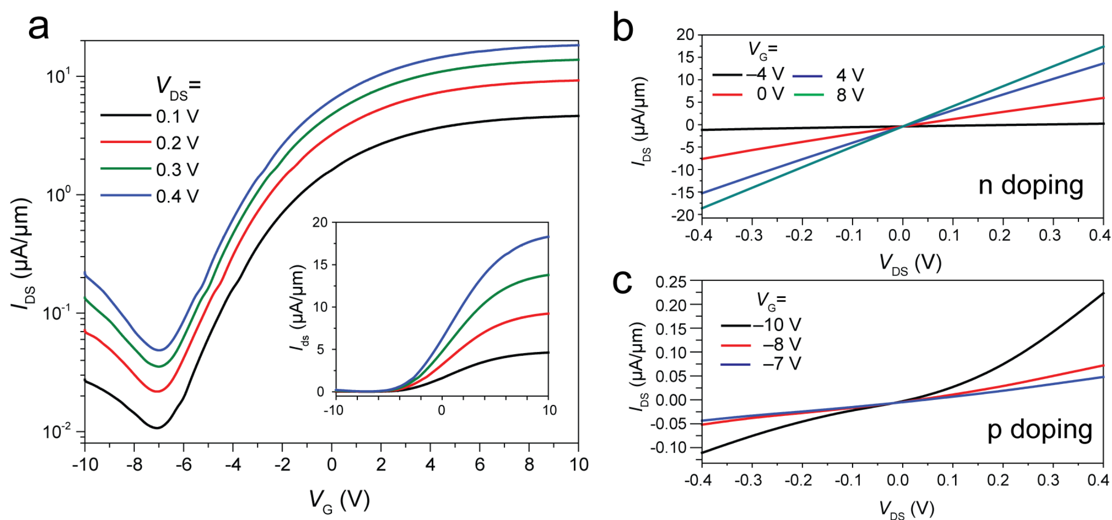

Figure 3.7: Field effect characteristics of the BP photodetector. (a) Source-drain current (I_{DS}) of the device at various fixed bias voltages (V_{DS}) as the gate voltage (V_{G}) is swept. Inset: linear scale plot of the main panel. (b) and (c) I-V characteristics of the device when the BP is gated to be n-doped (b) and p-doped (c), respectively.

With the configuration of a top-gate and thin gate dielectric, the source-drain current of our device can be efficiently modulated by the gate voltage with an on-off ratio of 500, similar to other devices with comparable BP thicknesses [14, 54, 111]. However, unlike BP devices using a bottom-gate [45, 54, 111], the field-effect characteristics (figure 3.7a) of our top-gated BP FET shows much higher conductance on the electron side when a large positive gate voltage is applied than on the hole side. Also, the source-drain I-V relation is linear when the BP is n-doped but nonlinear when the BP is p-doped (figure 3.7b and c). This indicates that the Schottky barrier at the contact-BP interface is lower when the BP is n-doped than when the BP is p-doped. This can be attributed to the effects induced

by capping the BP with the Al_2O_3 gate dielectric layer [117]. Additionally, the fact that the *I*-*V* characteristics are mostly symmetric about the positive and negative source-drain voltage reflects that the two contacts are nearly identical. Therefore, excellent transport properties and efficient tuning of the carrier type and concentration in BP are achieved in our device.

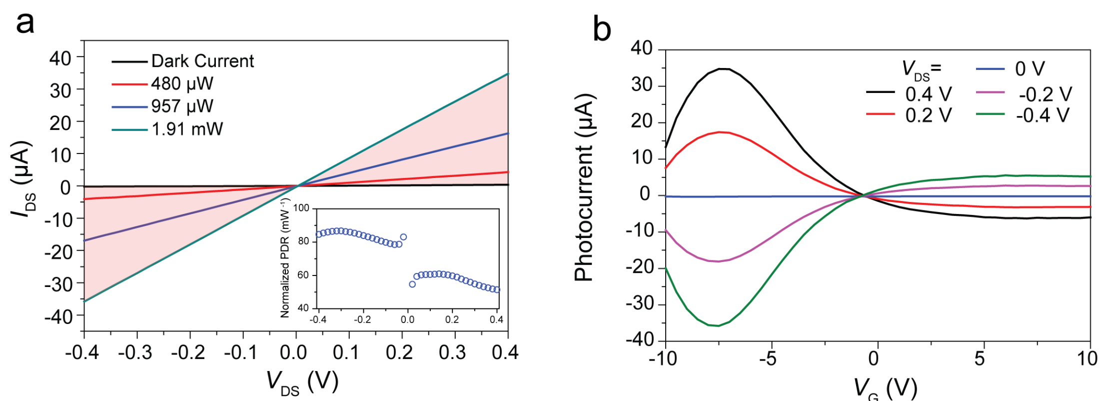

Figure 3.8: Gate and bias tuned photoresponse of the BP photodetector. (a) Source-drain current versus bias voltage when optical signal is off (black line) and at various power levels (red: 480 µW; blue: 957 µW; green: 1.91 mW). Gate voltage is −8 V. Inset: Normalized photocurrent to dark-current ratio (NPDR) for an optical power of 1.91 mW. (b) Photocurrent versus gate voltage at fixed bias voltages (1.91 mW optical power). The sign of the photocurrent changes as the gate voltage increases from negative values (where the BP has low doping) to positive (where the BP is highly n-doped).

We next measured the BP device's response to optical signals in the waveguide. A tunable diode laser was fibre-coupled to the grating couplers, which have a coupling efficiency of ∼25%. Figure 3.8a shows the *I*-*V* characteristics of the device at various optical power levels and with $V_G = -8$ V so the BP is nearly intrinsic. It can be clearly seen that significant photocurrent, positive relative to V_{DS}, is generated when the optical signal is on. The positive sign of the photocurrent suggests that the generation mechanism is photovoltaic [50, 79, 120]. The

photo-thermoelectric effect can be ruled out as the photogeneration mechanism because the device is symmetric between the source and drain contacts [48, 79, 83]. However, when V_{G} is increased to be more positive so the BP is gated to be more heavily n-doped, as shown in figure 3.8b, the sign of the photocurrent changes to negative relative to V_{DS}. The sign change suggests that the photocurrent generation mechanism is no longer photovoltaic, but is due to the bolometric effect, which stems from a decrease in conductance when the BP is heated by optical absorption. This bolometric effect is similar to that observed in biased graphene photodetectors, in which the reduction of conductance at elevated temperatures is attributed to increased phonon scattering [48, 79]. Compared with graphene, it appears that the bolometric photocurrent in BP at high doping is much weaker than the photovoltaic current at low doping. This is attributed to the higher quantum efficiency in BP than that found in graphene. (For a detailed comparison with other published works on the origin of the photoresponse in BP, see section 3.4.)

To further illustrate these two distinct regimes of photogeneration, we systematically measured the photocurrent at various gate and bias voltages with a fixed optical power of 1.91 mW. The devices were held at a fixed gate while the bias voltage was swept twice, once with no optical power and once with the laser source on. The difference between the two scans yielded gate- and bias-dependent photocurrent. Power- and bias-dependent photocurrent were extracted from these two-dimensional scans, and the responsivity was calculated after accounting for loss from the input grating coupler, the power splitting arm of the MZI structure, and the power absorbed by the channel material. The results are plotted in figure 3.9a. The change of photocurrent sign with gate voltage is clearly seen for all bias voltages. At low doping ($-10\,\mathrm{V} < V_{\mathrm{G}} < -1\,\mathrm{V}$), the photocurrent is strong

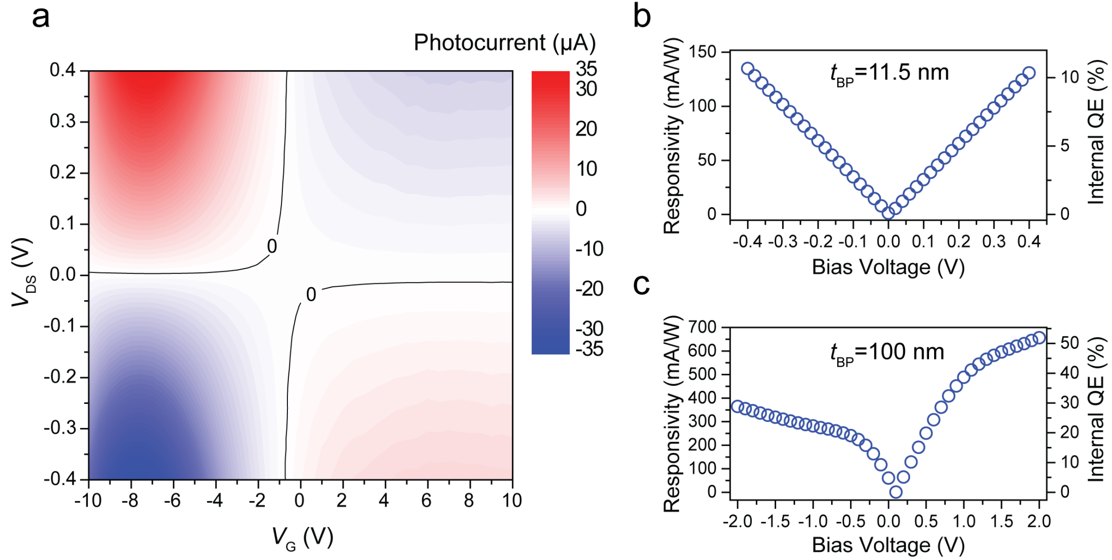

Figure 3.9: (a) 2D contour plot of the photocurrent as a function of gate and bias voltages. The photocurrent generation is dominated by the photovoltaic and bolometric effect in regions with low and high doping, respectively. (b) and (c) Intrinsic responsivity and internal quantum efficiency versus applied bias for 11.5 nm and 100 nm thick BP.

and dominated by the photovoltaic current, whereas at high n-type doping ($V_G > 0\,V$), the photocurrent is weak, opposite the bias voltage and dominated by the bolometric effect. We calculated the intrinsic responsivity and internal quantum efficiency using the actual amount of optical power absorbed by the BP (determined from interferometry results). As can be seen from figure 3.9b, optimal performance is achieved when the BP is gated to be nearly intrinsic (when $V_G = -8\,V$) and under a large bias voltage ($V_{bias} = V_{DS} = -0.4\,V$), where it achieves the best intrinsic responsivity of 135 mA/W and internal quantum efficiency of 10%. However, taking the absorption by the graphene top-gate into account, the overall extrinsic responsivity of the device is reduced to 18.8 mA/W. Higher responsivity could be achieved with a larger bias voltage, but because the applied gate voltage is high, the bias voltage was not increased beyond $\pm 0.4\,V$ to avoid the risk of

breaking down the gate dielectric. In another device with 100-nm-thick BP and no top-gate (figure 3.9c), an intrinsic responsivity up to 657 mA/W and internal quantum efficiency up to 50% are achieved at 2 V bias voltage.

Importantly, due to the finite bandgap in BP, the dark current of our device is very low. At the optimal operation condition ($V_\mathrm{G} = -8\,\mathrm{V}$, $V_\mathrm{bias} = -0.4\,\mathrm{V}$) the dark current ($I_\mathrm{dark}$) is only 220 nA, which is more than three orders of magnitude less than that of a graphene photodetector under similar bias voltage [26, 79] and four orders of magnitude less than the results shown in figure 3.2. Taking the external responsivity into account, the normalized photocurrent-to-dark-current ratio (NPDR) [121] of our BP photodetector is plotted in the inset of figure 3.8a. At $V_\mathrm{bias} = -0.4\,\mathrm{V}$, the NPDR of our BP photodetector is $85\,\mathrm{mW}^{-1}$, which is four orders of magnitude higher than that of typical graphene devices [26, 27]. This value of NPDR is also comparable to that of waveguide-integrated Ge photodetectors of a similar configuration [58] and could be improved by an order of magnitude if the top-gate absorption loss were eliminated. Although graphene photodetectors can be operated in the photovoltaic mode at zero bias, with zero dark current but with a substantially compromised responsivity [26, 27], the low resistance of graphene leads to high Johnson current noise from the shunt resistance. In comparison, the source-drain shunt resistance of our BP photodetector is very high ($R_\mathrm{SD} > 1\,\mathrm{M\Omega}$), so the noise of the photodetector is dominated by dark-current shot noise. Thus, in terms of both responsivity and noise level, the BP photodetector has significant advantages over its graphene counterparts.

The frequency response of the photocurrent can also help reveal the mechanism of photocurrent generation. Figure 3.10a shows the normalized response of the photodetector to an amplitude-modulated optical signal over a broad frequency range from 10 Hz to 10 GHz, measured using a lock-in amplifier (for less

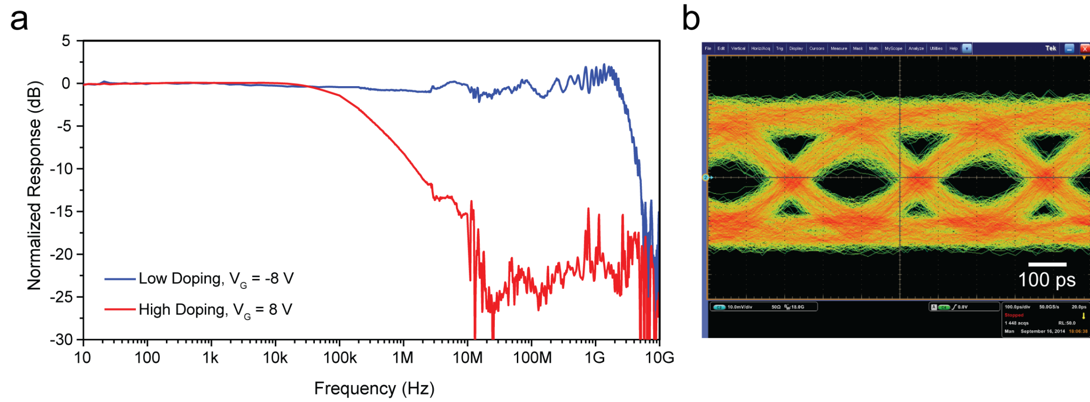

Figure 3.10: Broadband frequency response of the BP photodetector. (a) The response of the BP photodetector is measured when the BP is gated to low and high doping. At low doping, the response is broadband with a cut-off frequency of 3 GHz, which is limited by the RC bandwidth of the contact pads and the input impedance of the preamplifier. At high doping, the response rolls-off at 0.2 MHz, indicating that the photoresponse is of thermal origin as expected from the bolometric effect. (b) Receiver eye diagram at 3 Gbit/s data rate measured with the BP photodetector. Scale bar: 100 ps.

than 100 kHz) and network analysers (for 100 kHz to 10 GHz) while fixing the bias voltage ($V_{\text{bias}} = 0.4\,\text{V}$). The low-frequency photoresponse (10 Hz to 100 kHz) was measured by modulating the laser source with a high-bandwidth electro-optic modulator (EOM, Lucent 2623NA) driven by a signal generator. The photocurrent was amplified using a low-noise current preamplifier (Stanford Research Systems, SR570) and monitored with a Stanford Research Systems SR830 lock-in amplifier. The gate voltage was swept from $-10\,\text{V}$ to $10\,\text{V}$ and the amplitude of the photocurrent was recorded at various driving frequencies. Mid-range frequencies (100 kHz to 10 MHz) were measured using a radiofrequency preamplifier and a 3 GHz bandwidth network analyser (HP 3577B). High-frequency measurements (10 MHz to 10 GHz) were achieved with a 20 GHz bandwidth network analyser (Agilent E8362B PNA). A 12 GHz photoreceiver (Newport 1554-A) was used to

monitor the frequency dependence of the EOM and correct the measured frequency response. All measurements were performed at room temperature in an ambient atmosphere.

When the BP is gated with $V_G = -8\,\mathrm{V}$ to be nearly intrinsic, the photodetector shows a high-speed response with a roll-off frequency measured to be $f_{3\mathrm{dB}} = 2.8\,\mathrm{GHz}$, which is limited by the RC bandwidth of the device as well as the bandwidth of the measurement instruments (including the current amplifier and bias tee). This fast response is expected for the photovoltaic mechanism of photocurrent generation, which is fundamentally limited by the carrier recombination time in BP and is accelerated by the bias field. In stark contrast, when the BP is gated to be highly n-doped, the photocurrent response rolls off at a much lower frequency of $f_{3\mathrm{dB}} = 200\,\mathrm{kHz}$. Because the photocurrent in this regime is due to the bolometric effect, this slower frequency response can be attributed to the low in-plane lattice thermal conductivity of BP [122], as well as the thermal response of the silicon waveguide [123]. The dramatically different response speed at different doping levels in the BP thus further corroborates the distinct generation mechanisms and highlights the optimized performance of the device when BP is gated to be intrinsic. To demonstrate the feasibility of using the BP device in high-speed optical communication, we also performed an eye-diagram measurement using a pseudo-random bit series (PRBS) with a data rate of 3 Gbit/s and a low optical power of 1.2 mW (0.8 dBm). The completely open eye in figure 3.10b indicates that the BP photodetector can be readily used for practical optical communication.

3.4 Discussion

Modeling of the photothermoelectric, photobolometric, and photovoltaic contributions to the net photocurrent in black phosphorus have been discussed in detail by Low *et al.* [48]. The authors also included brief experimental verification of their model and concluded both from simulation and experiment that under a moderate bias ($V_{\mathrm{DS}} > 50$ mV), the bolometric effect dominates the net photocurrent. This bolometric photocurrent is opposite in sign relative to the dark current compared to the photovoltaic current, which has the same sign as the dark current (*i.e.* bias direction). This difference in sign provides a distinctive method for identifying whether the bolometric effect or the photovoltaic effect dominates the net photocurrent as stated on page 4 of their paper.

The conclusion drawn from this paper, while correct for the case of bulk material, is not comprehensive for all black phosphorus photodetectors as we clearly demonstrate in figures 3.8b and 3.9a. The authors use a 100 nm thick flake of black phosphorus and are not able to significantly modulate the source-drain current with a back gate due to a finite screening length (~10 nm). Therefore, when calculating the carrier density, the authors conclude that their device has a considerable hole carrier density of $2.5 \times 10^{12}\,\mathrm{cm}^{-2}$. This heavily doped device shows photocurrent dominated by the bolometric effect because their BP device has substantial p-doping, and electron-electron scattering can significantly reduce n^*, where n^* is the number of photoexcited carriers.

Our experimental results confirm the theory presented in [48], but because we are able to control the doping level and use a flake with a thickness (11.5 nm) comparable to the screening length, we are able to observe photocurrent in the intrinsically-doped regime. In this regime, the lack of carriers both suppress dark

current and drastically reduce photo-bolometric current. Therefore, we observe a flipping of the sign of the photocurrent when the doping level passes from heavily doped to lightly doped (see figures 3.8b and 3.9a) as predicted in [48]. Additionally, we see a drastic decrease in the bandwidth of our photodetector when we go from low doping to high doping (see figure 3.10a). The lower bandwidth for higher doping is due to the fact that the bolometric effect is dependent on the in-plane lattice thermal conductivity of $12.1\,\mathrm{W\ m^{-1}\ K^{-1}}$ [122] which is much smaller than in graphene ($>2000\,\mathrm{W\ m^{-1}\ K^{-1}}$ [75]). This low thermal conductivity limits the operation speed of our detector in the highly doped region and gives us yet another method for identifying the mechanism of photocurrent generation.

As for the photothermoelectric current, since our contacts are symmetrically placed relative to the waveguide and have the same work function, we do not observe any contribution to the photocurrent at zero bias. This is in perfect agreement with figure 2c of [48] where the thermoelectric photocurrent is zero when optical power is at the exact center of the channel, between two identical contacts.

Additional recent works on the mechanisms of photocurrent in black phosphorus have served to confirm our results. Hong *et al.* [120] demonstrated in thin black phosphorus flakes (8 nm) that photovoltaic current dominates in regions of low doping, while thermal effects dominate for heavily doped regions. Other works by Deng *et al.* [124] and Buscema *et al.* [47] demonstrate black phosphorus pn junctions biased at low doping levels where the photovoltaic effect dominates the photocurrent.

We have included table 3.1 as a comparison of our black phosphorus photodetectors with other state-of-the-art black phosphorus photodetectors published prior to our work. Our photodetectors show the highest responsivity for near-IR

t_{BP}	R_{ext} (mA/W)	I_{dark} (A)	f_{3dB} (Hz)	λ_0	Ref.
11.5 nm	19	2.2×10^{-7}	3×10^9	1.55 µm	this work
100 nm	631	5.6×10^{-4}	3×10^9	1.55 µm	this work
8 nm	4.8	$\approx 10^{-7}$	6.2×10^3	Visible	[41]
14.5 nm	28	$\approx 10^{-8}$	$\approx 10^3$	Visible	[47]
120 nm	20 & 5	0 bias	$>4 \times 10^3$	532 & 1550 nm	[49]
11 nm	418	$\approx 10^{-8}$	unknown	633 nm	[124]

Table 3.1: Comparison between our device and other BP photodetectors contemporary to our work.

wavelengths and were six orders of magnitude faster than any black phosphorus photodetector demonstrated at the time. Using our MZI devices, we are also able to determine the maxim achievable responsivity based on the optical power absorbed in the black phosphorus layer.

3.5 Conclusion

In conclusion, a waveguide-integrated and gate-tunable photodetector based on few-layer BP has been demonstrated for the telecom band. High responsivity, high response speed and low dark current are achieved when the BP is gated to low doping, and the photocurrent generation is dominated by the photovoltaic effect. In nearly every aspect of their performance, BP photodetectors can outperform graphene photodetectors and are more realistic for practical use. We expect the performance of BP photodetectors to be further improved when larger flakes of BP can be exfoliated or high-quality large-scale growth of BP can be achieved. If the number of layers in BP can be controlled, its bandgap can be tailored for a specific wavelength so that both the responsivity and dark current of the photodetector are optimal. In addition, BP shows strong anisotropy in both DC and optical conductivity [42, 54, 125]. If the armchair direction of BP can be aligned with the

source-drain direction (zigzag along the waveguide) using Raman spectroscopy so that both the optical absorption and carrier mobility are maximal, the responsivity and speed of the photodetector can be maximized with a reduced device footprint. These results and the potential of BP, combined with the many previous demonstrations of optoelectronic devices based on graphene and TMDCs, indicate that two-dimensional materials and their heterostructures [124, 126–128] can provide the components necessary for the realization of complete optical communications links and chart a clear path towards the commercial viability of two-dimensional materials for integrated optoelectronic applications.

Chapter 4

Nonlinear Optical Response of Black Phosphorus

While many have studied the linear optical response of black phosphorus, the non-linear response has remained relatively unexplored. This non-linearity can have applications ranging from saturable absorbers in mode-locked lasers to ultrafast pulse characterization. Here we use BP's nonlinear photoresponse to measure the intrinsic response time of a BP photodetector using ultrafast pump-probe measurements. With this technique, we are able to observe how the detection speed depends on the applied source-drain bias. We also report on the observation of third-harmonic generation in black phosphorus using an ultrafast near-IR laser and measure $\chi^{(3)}$ experimentally for the first time. It was found that the measured third-harmonic signal is highly dependent on both the incident polarization and the number of layers present. It is also demonstrated that the third-order response of black phosphorus can be used to characterize ultrafast pulses.

4.1 Introduction

As explained in chapter 3, black phosphorus (BP) is a relatively new, 2D material with highly unique optical and electrical properties, including high carrier mobility [45, 111], optical and electrical anisotropy [125, 129, 130], and importantly, a tunable, direct bandgap [14, 112, 131, 132]. Particularly, for thicknesses greater than a few nanometers, BP's bandgap bridges the technically important mid-infrared (mid-IR) spectral range that is not currently covered by other two-dimensional semiconductors [130]. These attributes of BP make it very promising for optoelectronic devices that cover a broad spectral range from near- to mid-IR for both communication and optical sensing [43, 77].

In chapter 3, we demonstrated that BP could be used as a high speed photodetector with a 3 GHz bandwidth. This bandwidth was limited by the resistance and capacitance of the device rather than the intrinsic material properties such as mobility, carrier lifetime, etc. In the first part of this chapter, we introduce a measurement scheme to experimentally determine the intrinsic response time of a BP photodetector that is passivated with boron nitride (BN). We also present preliminary results showing how the applied bias can increase the speed of the photodetector. These results provide a foundation to characterize future BP detectors made with van der Waals heterostructures.

4.2 Device design

Large area BN flakes were exfoliated onto 300 nm SiO_2/Si substrates using Scotch tape and located with a microscope. Flakes with uniform thickness were selected as the bottom supporting layer onto which BP was to be transferred. BN provides a high quality, atomically smooth substrate which is known to reduce carrier

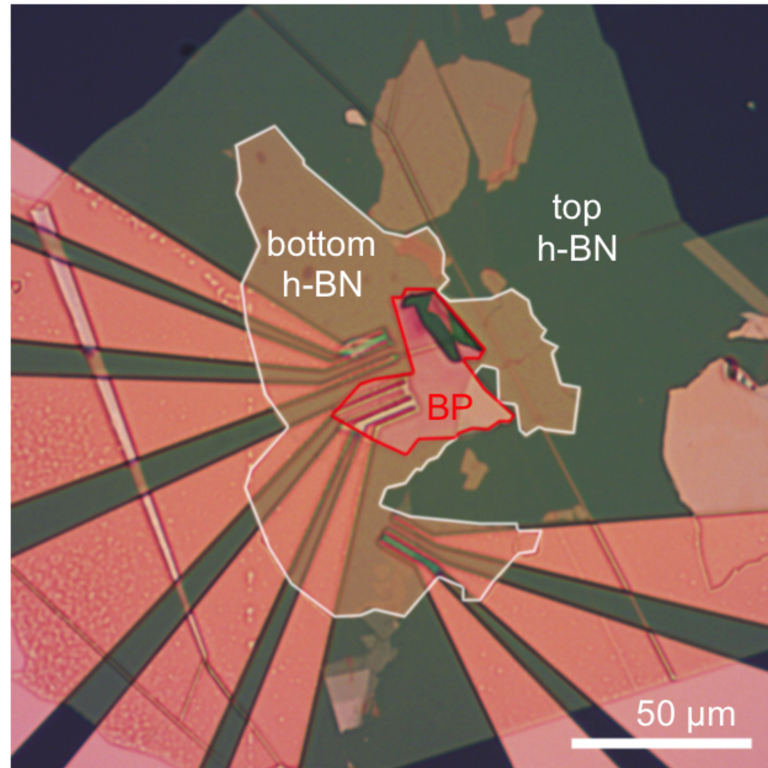

Figure 4.1: Optical image of BP photodetector encapsulated with BN. BP channel lengths are 3 µm and 1.5 µm.

scattering and improve mobility [10,37,52]. BP flakes were exfoliated onto PDMS coated glass slides and transferred onto the bottom BN support layer using the dry transfer technique described in the Appendix, section A.4. Immediately after transfer, the samples were coated with PMMA to protect the surface, and 5 nm Ti / 50 nm Au metal contacts were patterned with ebeam lithography and evaporation. Immediately after liftoff, a top BN layer was used to cover and passivate the BP [44] using the same dry transfer method. The completed device was annealed at 125 °C under vacuum for 12 hours and can be seen in figure 4.1.

4.3 Methodology and experimental setup

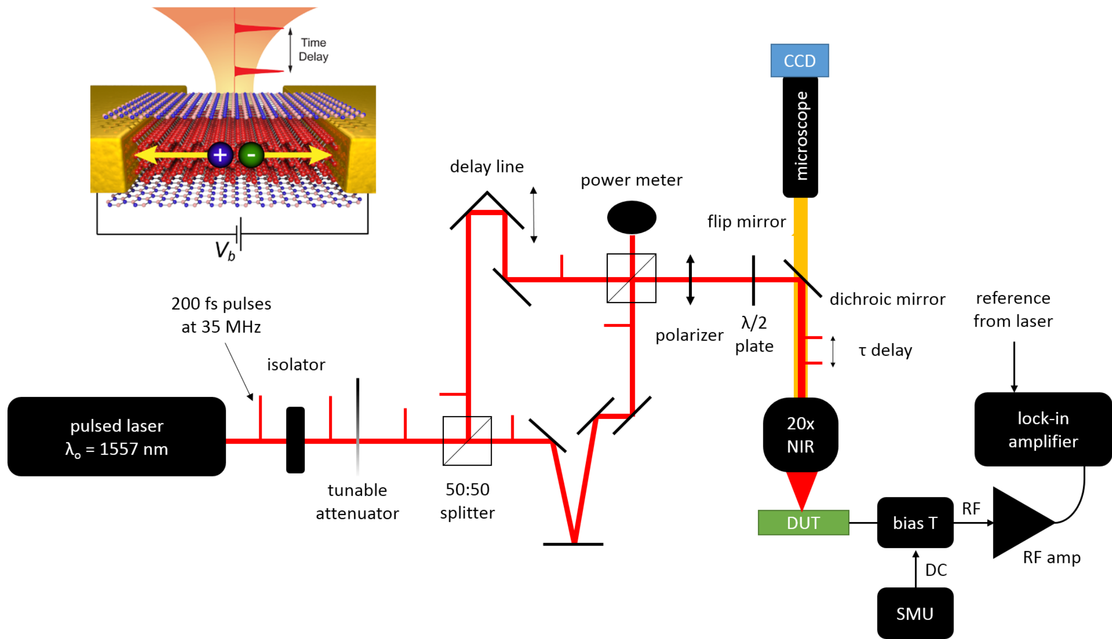

Figure 4.2: Experimental setup used to measure intrinsic speed of BP photodetector. Inset: Illustration of exciton generated in the channel, disassociated and sweep to the contacts through application of an applied bias.

In order to measure the intrinsic speed of the photodetector, we use an ultrafast laser with a pulse width of ∼200 fs which we split into two pulses (*i.e.* pump and probe) and vary the time delay between them (as shown in figure 4.2). This is accomplished using an optical delay line which can provide up to a 1 ns delay between the pump and probe pulses. During the measurement, the time delay is varied and the photoresponse of the device is recorded as a function of time delay. A bias tee and Keithley 2400 SMU is used to provide an adjustable source-drain bias to the photodetector. The output of the bias tee is connected to a high frequency amplifier which connects to an RF lock-in with 80 MHz bandwidth. The lock-in is referenced to the pulse train from the laser and is used to

monitor the magnitude of the photocurrent. In our initial measurements, a low frequency lock-in and optical chopper were used to measure the photoresponse at ∼1 kHz. However, it was found that by referencing the lock-in to the pulse train at ∼35 MHz, the nonlinearity due to the thermal response of the channel (around 200 kHz in our devices from chapter 3) could be removed from delay-dependent photoresponse. Due to the nonlinear response of the photodetector, the signal reduces for small delays and recovers with a time constant characteristic of the process which limits the intrinsic speed of BP. This time-dependent effect is illustrated in figure 4.3 which includes an example experimental trace.

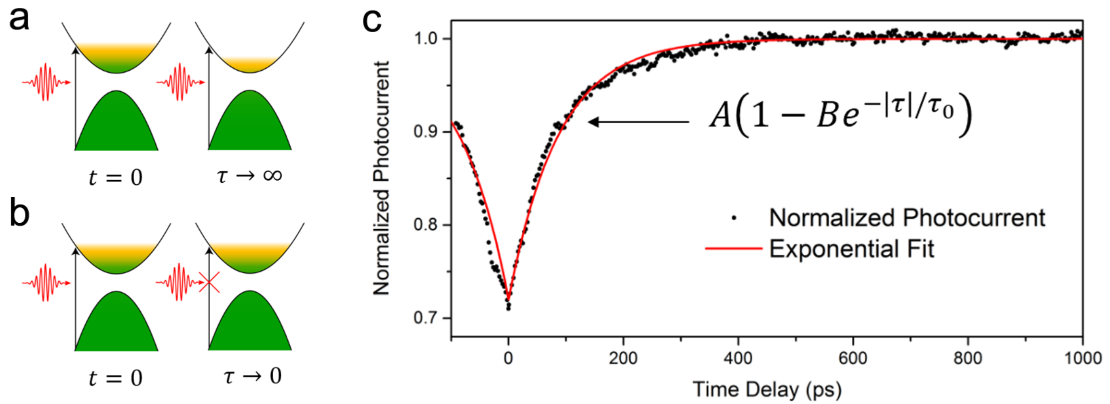

Figure 4.3: Illustration of saturation in photoresponse of BP photodetector. (a) At long time delays, the material has enough time to recover after the initial pulse at $t = 0$ and the signal does not vary with time delay. (b) As the time delay approaches zero, the material does not have enough time to recover from the first pulse and the photoresponse decreases. In this illustration, saturable absorption is used, but this is not necessarily the mechanism in our case. (c) Experimental trace of the photoresponse verses time delay with a fit to the data.

The nonlinear process illustrated in figure 4.3a and b corresponds to saturable absorption, where the absorption of a photon is reduced due to Pauli blocking when the material has a large number of photo-excited carriers. This is one possibility for the nonlinear response we see in the photocurrent, but this could also

be due to other effects such as electron-hole recombination, exciton-exciton annihilation, or carrier-carrier scattering [40]. Further work is needed to understand the nonlinear mechanism at play. The delay-dependent photoresponse shown in figure 4.3c is a direct result of the sub-linear response of the photodetector with increasing optical power (thus the dip at zero delay). We fit the experimental data with the following equation:

$$I_{PC}(\tau) = A(1 - Be^{-|\tau|/\tau_0}) \tag{4.1}$$

where A is the photocurrent as $\tau \to \infty$, B is what we call the "saturation ratio," and τ_0 is the lifetime of the photoexcited carriers in the device.

4.4 Results

As we mentioned, the photodetector must be operated at an optical power that provides a nonlinear response in order to measure the intrinsic response time. We first characterized the photocurrent as a function of optical power (figure 4.4a) and found that $I_{PC} \propto P^{0.49} \approx \sqrt{P}$. Interestingly, the power dependence follows a power law fit rather than the typical saturable absorption equation: $\alpha/(1+P/P_{\text{sat}})$. It is worth noting that this same $\sqrt{P}$ dependence has been observed before in the cooling dynamics of hot electrons in graphene photodetectors [133], but it remains to be seen if this applies to BP as well.

Using a polarizer and half wave plate, we measured the how the photocurrent depends on the incident polarization angle. Here we have set zero degrees to be along the x-axis (or armchair direction) and 90 degrees to be along the y-axis of the crystal. One can see from figure 4.4b, that we observe strong anisotropy in the photocurrent which confirms both the quality of the black phosphorus flake and the successful passivation from the top and bottom boron-nitride. This anisotropy

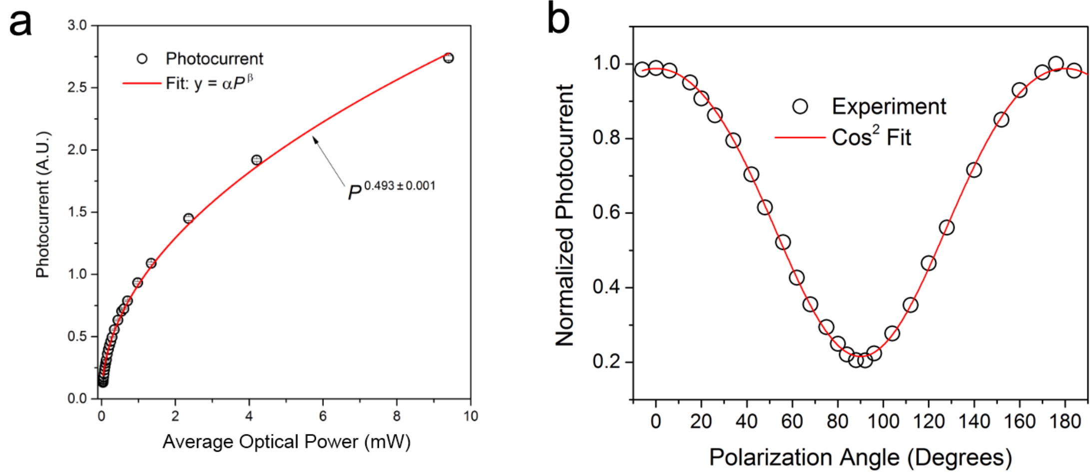

Figure 4.4: Nonlinear and anisotropic optical response of BP photodetector. (a) Photocurrent showing sub-linear response to the average optical power. (b) Polarization dependent photocurrent arising from anisotropic absorption in the armchair and zigzag directions.

can be attributed to the difference in absorption between light polarized along the x- verses y-axis of the crystal [42, 129].

After characterizing the photodetector's power and polarization response, we studied how the optical power and bias voltage effects the parameters in equation 4.1. If we look at B in equation 4.1, we see that it will have a value between 0 and 0.5 which characterizes the amount that the first pulse will saturate the BP channel (linear response if $B = 0$ and complete saturation if $B = 0.5$). We can write B in terms of $I_{PC}(\tau)$:

$$B = \frac{I_{PC}(\tau \to \infty) - I_{PC}(\tau = 0)}{I_{PC}(\tau \to \infty)} \tag{4.2}$$

In the case where $I_{PC} = \beta\sqrt{P}$ (where β is some constant of proportionality), $I_{PC}(\tau \to \infty) = 2\beta\sqrt{P}$ since the BP will see two pulses at power P when there is enough time for the material recover from the first pulse and $I_{PC}(\tau = 0) = \beta\sqrt{2P}$ since the material cannot resolve two independent pulses at power P. With this

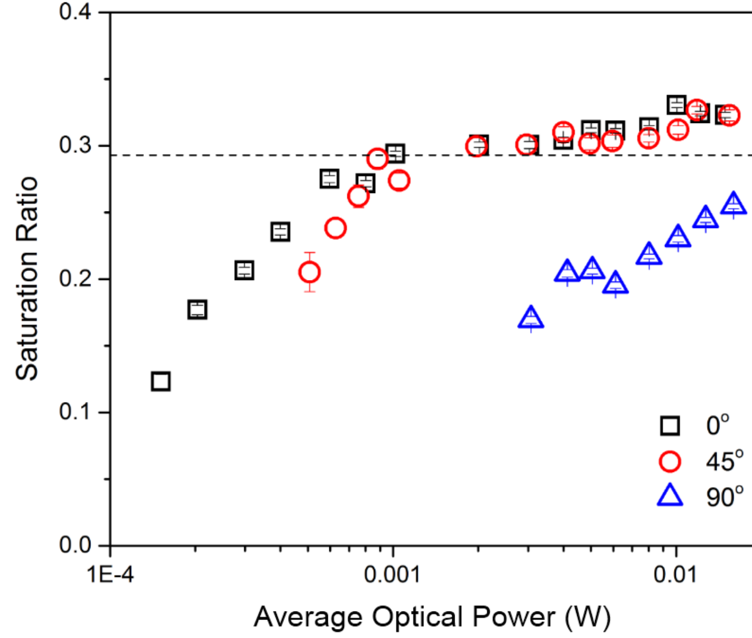

Figure 4.5: Saturation of the BP channel increases with optical power and then saturates after a certain power showing the transition from linear to nonlinear photoresponse (dashed line at $B = 0.293$). Zero degrees is set to be along the x-axis of the crystal.

information, we can solve for B:

$$B = \frac{2\beta\sqrt{P} - \beta\sqrt{2P}}{2\beta\sqrt{P}} = 1 - \frac{\sqrt{2P}}{2\sqrt{P}} = 1 - \frac{1}{\sqrt{2}} = 0.293 \tag{4.3}$$

This means that for $I_{PC} \propto \sqrt{P}$, $B = 0.293$ regardless of the input power. If we record $I_{PC}(\tau)$ for varying optical powers and fit equation 4.1 to each trace like in figure 4.3c, we can plot B verses incident optical power. Looking at figure 4.5, we actually see the saturation ratio first increase with power and then saturate as we would expect. This makes sense because the optical power is expected to be linear with the number of carriers for low power levels. Here we can more clearly see that transition with the saturation ratio. We also see that the non-linear saturation occurs at different powers for different polarizations of light. This is likely due to

the difference in optical absorption between the armchair and zigzag directions.

We also observed that the carrier lifetime varied with applied bias. Increasing the source-drain bias creates a large field in the channel and sweeps photo-excited carriers to the contacts more quickly. This is known as the transit time and can be derived from the drift velocity. If we consider the time it takes for a carrier that is excited in the center of the channel by a photon to drift to the contacts, we can write the following relation:

$$\tau_{tr} = \frac{l}{2v_d} = \frac{l}{2\mu E} \tag{4.4}$$

where τ_{tr} is the transit time, $l/2$ is half the channel width, and $v_d = \mu E$ is the drift velocity. With an applied bias on the channel V_b, the electric field inside the channel is $E \approx V_b/l$, so τ_{tr} can be written as:

$$\tau_{tr} = \frac{l^2}{2\mu V_b} \tag{4.5}$$

At very low applied bias voltages, the photo-carriers will be excited and recombine before being collected at the contacts since there is very little electric field in the channel. This is known as the recombination time τ_r. Conversely, at very large bias voltages, various scattering mechanisms and interfacial transfer times will dominate and the lifetime will saturate at τ_s. These various contributions can be included in the total carrier lifetime τ which is related to τ_{tr}, τ_r, and τ_s in the following way [40]:

$$\tau^{-1} = (\tau_s + \tau_{tr})^{-1} + \tau_r^{-1} = (\tau_s + \frac{l^2}{2\mu V_b})^{-1} + \tau_r^{-1} \tag{4.6}$$

The experimental results are shown in figure 4.6a with a fit to equation 4.6. $\tau_s = 60\,\text{ps}$ and $\tau_r = 310\,\text{ps}$ gave the best fit to the data ($\mu \approx 1000\,\text{cm}^2/\text{V}\cdot\text{s}$). Unfortunately, in 2D materials the electric field does not penetrate far into the

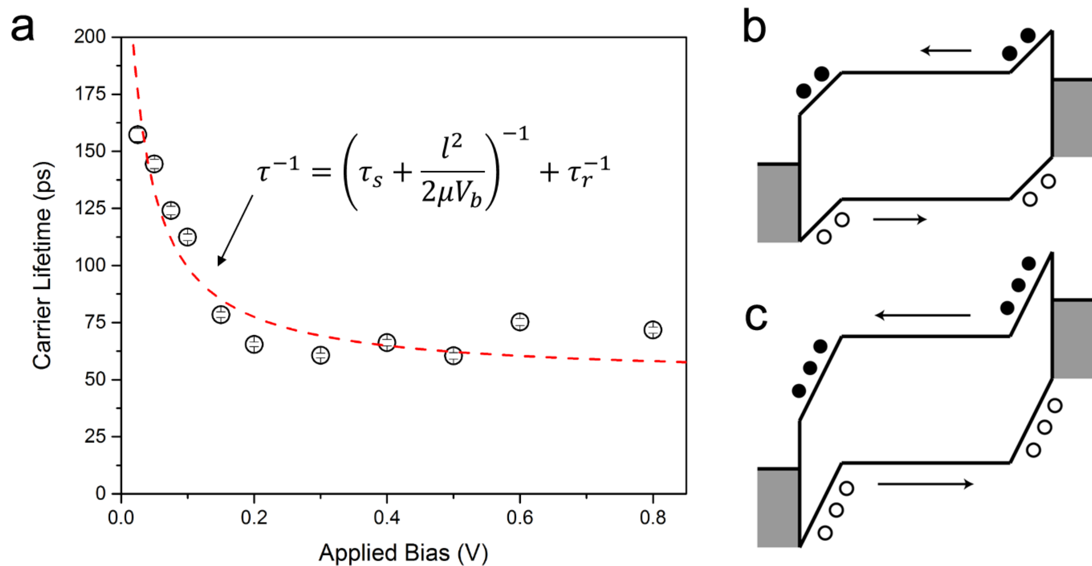

Figure 4.6: Bias dependent carrier lifetime in a BP photodetector. (a) Plot of carrier lifetime (parameter τ_0 in equation 4.1) verses applied bias. Increasing the bias voltage sweeps out photo-excited carriers to the contacts more quickly, decreasing the carrier lifetime. Illustration of band diagram for the case of (b) low and (c) high applied bias. Most of the voltage drop occurs across the Schottky barrier in these devices.

channel due to screening effects as illustrated in figure 4.6b and c. Despite this, we can already see a minimum carrier lifetime of 60 ps here which corresponds to a frequency response of over 7 GHz. This can be potentially overcome by using graphene to electrically contact above and below the BP so that the field is vertical rather than in-plane. This has been successfully demonstrated in MoS_2 and WSe_2 heterostructures [40].

4.5 Third-harmonic generation in black phosphorus thin films

While investigating the non-linear photoresponse of BP, we observed green light emission at high pump powers (figure 4.7). This is due to third-harmonic generation arising from BP's nonlinear optical response which has remained relatively unexplored to date compared to other 2D materials. For example, MoS_2 [134–136], WSe_2 [137, 138], and hBN [135], all with non-centrosymmetric lattice structures, have shown strong second-order nonlinear optical effects, such as second-harmonic generation (SHG). SHG in these materials has shown strong enhancement at the exciton resonances [137], can be electrically tuned by a local back gate [138], and has been utilized for optically probing the crystal orientation [134] and thickness [135, 136].

Additionally, third-order optical nonlinearity such as third-harmonic generation (THG) has been observed to be strong in graphene [139–142], as well as in MoS_2 thin films [142–144]. In terms of nonlinear optics in BP, its centrosymmetric crystalline structure only permits third-order nonlinearity but its strong anisotropy and layer dependent band structure should lead to very intriguing nonlinear optical effects. Research to date, however, has been primarily limited to the saturable absorption effect in BP, studied with z-scan [145, 146] and ultrafast pump-probe [147] techniques for liquid exfoliated BP suspensions and utilized for application in mode-locked lasers [148–152]. The intrinsic optical nonlinearity of crystalline BP has not been experimentally investigated.

In the rest of this chapter, we investigate BP's optical nonlinearity by measuring both the polarization and thickness dependence of THG in multilayer BP samples. We find that the THG in BP is strong and highly dependent on both

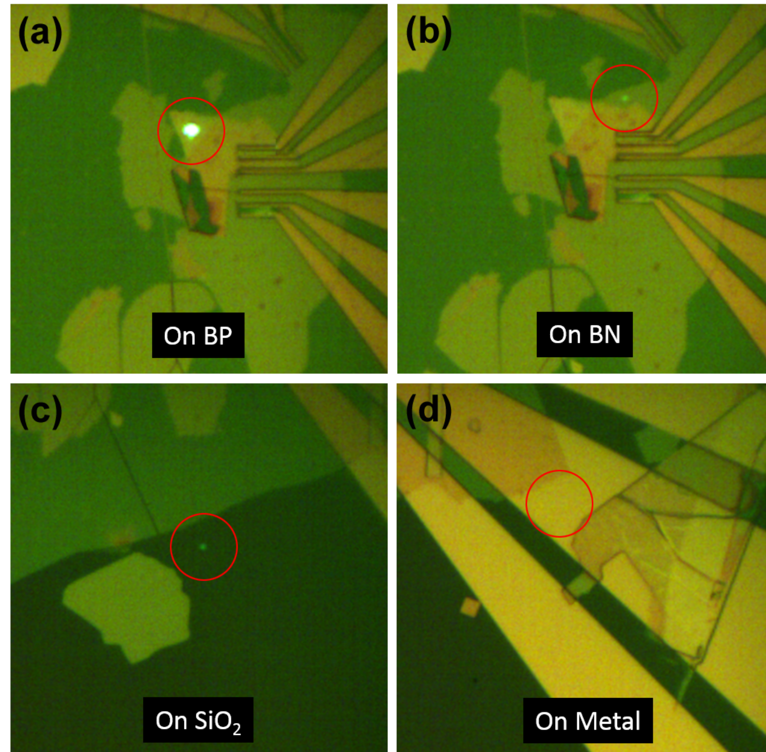

Figure 4.7: Third-harmonic generation observed from the BP device of the previous section using an ultrafast pump laser. (a) THG emission from BP flake. (b) Weak THG from region with BN. Emission is likely from the SiO_2/Si interface below BN as seen in (c). (c) Weak THG from SiO_2/Si region. (d) No signal observed from gold contact pads.

the polarization of the incident light and the number of layers under investigation. From our measurements, BP's third-order nonlinear susceptibility (*i.e.* $\chi^{(3)}$) is determined and used to characterize ultrafast pulses of the pump laser.

4.6 Theory of Third-Harmonic Generation in Thin Films

It is well known that the polarization of a linear material (*i.e.* the dipole moment per unit volume) is related to the electric field by the following equation:

$$\widetilde{P}(t) = \epsilon_0 \chi^{(1)} \widetilde{\mathbf{E}}(t) \tag{4.7}$$

where $\chi^{(1)}$ is a constant of proportionality known as the linear susceptibility and is material dependent. For large electric fields, it is possible for the material to respond nonlinearly with the incident optical power and equation 4.7 can be expanded in a power series:

$$\begin{aligned}\widetilde{P}(t) &= \epsilon_0 \left[\chi^{(1)} \widetilde{\mathbf{E}}(t) + \chi^{(2)} \widetilde{\mathbf{E}}^2(t) + \chi^{(3)} \widetilde{\mathbf{E}}^3(t) + ...\right] \\ &\equiv \widetilde{P}^{(1)}(t) + \widetilde{P}^{(2)}(t) + \widetilde{P}^{(3)}(t) + ...\end{aligned} \tag{4.8}$$

where $\chi^{(2)}$ and $\chi^{(3)}$ are the second- and third-order susceptibilities respectively. While equations 4.7 and 4.8 assume $\widetilde{P}(t)$ and $\widetilde{\mathbf{E}}(t)$ to be scalar quantities, in general they are not and $\chi^{(n)}$ is therefore a tensor of rank $n+1$. Additionally, in general $\chi^{(n)}$ is a function of frequency which has also been ignored in these equations for simplicity. As a consequence of equation 4.8, photons of multiple frequencies can mix to create photons of a different frequency. For example, SHG occurs when two photons mix in a media with $\chi^{(2)}$ to generate a single photon at twice the frequency of the original photons. Since the photon energy is equal to $\hbar\omega$, energy is conserved in this process. THG operates in the same way, except with three photons instead of two. Figure 4.8 illustrates this process using energy diagrams. It is worth mentioning that SHG can only occur in non-centrosymmetric materials (BP is centrosymmetric) whereas THG is possible in all materials. For more on the origin of THG in a centrosymmetric material, see Appendix C.

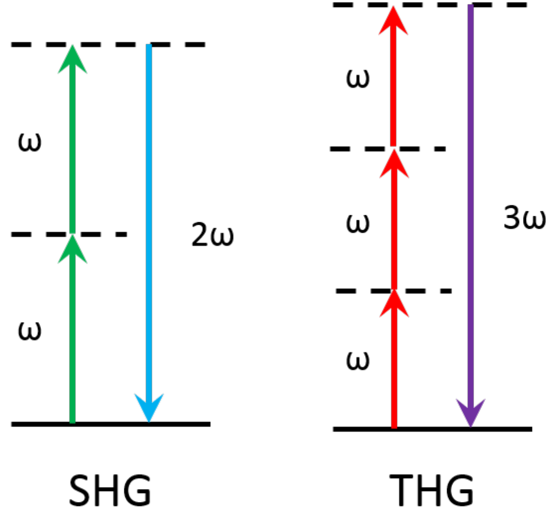

Figure 4.8: Energy diagram illustrating second- and third-harmonic generation in materials.

4.7 Derivation of third-harmonic generation in a lossy medium

If we consider Maxwell's equations in a medium, we have the following relations:

$$\nabla \cdot \widetilde{\mathbf{D}} = 0 \tag{4.9}$$

$$\nabla \cdot \widetilde{\mathbf{B}} = 0 \tag{4.10}$$

$$\nabla \times \widetilde{\mathbf{E}} = -\frac{\partial \widetilde{\mathbf{B}}}{\partial t} \tag{4.11}$$

$$\nabla \times \widetilde{\mathbf{H}} = \frac{\partial \widetilde{\mathbf{D}}}{\partial t} \tag{4.12}$$

where we have assumed no free charges and no free currents (*i.e.* $\rho = 0$ and $\widetilde{\mathbf{J}} = 0$). For the case of nonmagnetic materials, we know that $\widetilde{\mathbf{B}} = \mu_0 \widetilde{\mathbf{H}}$ and $\widetilde{\mathbf{D}} = \epsilon_0 \widetilde{\mathbf{E}} + \widetilde{\mathbf{P}}$. We can solve for the wave equation by taking the curl of both sides

of equation 4.11:

$$\nabla \times \nabla \times \widetilde{\mathbf{E}} = -\frac{\partial}{\partial t}(\nabla \times \widetilde{\mathbf{B}}) = -\mu_0 \frac{\partial}{\partial t}(\nabla \times \widetilde{\mathbf{H}}) = -\mu_0 \frac{\partial^2 \widetilde{\mathbf{D}}}{\partial t^2} \tag{4.13}$$

For the case of a nonlinear material, $\widetilde{\mathbf{D}}$ will have both linear and nonlinear terms. It is therefore convenient to separate $\widetilde{\mathbf{D}}$ into both its linear and nonlinear components:

$$\widetilde{\mathbf{D}} = \widetilde{\mathbf{D}}^{(1)} + \widetilde{\mathbf{P}}^{\mathrm{NL}} \tag{4.14}$$

where $\widetilde{\mathbf{D}}^{(1)} = \epsilon_0 \widetilde{\mathbf{E}} + \widetilde{\mathbf{P}}^{(1)} = \epsilon_0 \epsilon^{(1)} \widetilde{\mathbf{E}}$. $\epsilon^{(1)}$ is the linear dielectric constant that will, in general, depend on the frequency of the excitation field $\widetilde{\mathbf{E}}$. It is worth noting that $\epsilon^{(1)}$ is also generally a tensor and must be treated as such. However, when the material is isotropic or when the polarization of $\widetilde{\mathbf{E}}$ is an eigenvector of $\epsilon^{(1)}$ (our case), we can consider $\epsilon^{(1)}$ to be a scalar. We can also use the relationship $\nabla \times \nabla \times \widetilde{\mathbf{E}} = \nabla(\nabla \cdot \widetilde{\mathbf{E}}) - \nabla^2 \widetilde{\mathbf{E}}$ to simplify 4.13. For the case of plane-wave excitation, $\nabla \cdot \widetilde{\mathbf{E}} = 0$, so we can write the nonlinear wave equation as follows [153]:

$$\begin{aligned} \nabla^2 \widetilde{\mathbf{E}} &= \mu_0 \frac{\partial^2 \widetilde{\mathbf{D}}^{(1)}}{\partial t^2} + \mu_0 \frac{\partial^2 \widetilde{\mathbf{P}}^{\mathrm{NL}}}{\partial t^2} \\ \nabla^2 \widetilde{\mathbf{E}} - \frac{1}{\epsilon_0 c^2} \frac{\partial^2 \widetilde{\mathbf{D}}^{(1)}}{\partial t^2} &= \frac{1}{\epsilon_0 c^2} \frac{\partial^2 \widetilde{\mathbf{P}}^{\mathrm{NL}}}{\partial t^2} \end{aligned}$$

where $c = 1/\sqrt{\epsilon_0 \mu_0}$.

Solutions to the nonlinear wave equation will be a sum of plane waves of the form:

$$\begin{aligned} \widetilde{\mathbf{E}}(\mathbf{r}, t) &= \sum_q \widetilde{\mathbf{E}}_q(\mathbf{r}) e^{-i\omega_q t} \\ \widetilde{\mathbf{P}}^{\mathrm{NL}}(\mathbf{r}, t) &= \sum_q \widetilde{\mathbf{P}}_q^{\mathrm{NL}}(\mathbf{r}) e^{-i\omega_q t} \end{aligned}$$

substituting this in to the wave equation, we get the following:

$$\nabla^2 \widetilde{\mathbf{E}}_q(\mathbf{r}) + \frac{\omega_q^2}{c^2} \epsilon^{(1)}(\omega_q) \widetilde{\mathbf{E}}_q(\mathbf{r}) = -\frac{\omega_q^2}{\epsilon_0 c^2} \widetilde{\mathbf{P}}_q^{\mathrm{NL}}(\mathbf{r}) \tag{4.15}$$

since the wave equation must be satisfied independently for each frequency component ω_q. For the case of normal incidence light polarized along an eigenvector of $\epsilon^{(1)}$, we can write the incident field and nonlinear polarization in scalar form:

$$E_q(z) = A_q e^{ik_q z} + c.c., \quad P_q^{\mathrm{NL}}(z) = \epsilon_0 \chi^{(3)} A_j A_k A_l e^{i(k_j+k_k+k_l)z} + c.c. \tag{4.16}$$

where $k_q^2 = \frac{\omega_q^2}{c^2}\epsilon^{(1)}(\omega_q) = \frac{\omega_q^2}{c^2}\widetilde{n}_3^2$. For the case of THG, we label $j = k = l = 1$ to be the fundamental frequency and $q = 3$ to be the third-harmonic. In order to avoid a trivial solution, we allow A_q to be a slowly varying function of z. Substituting this into equation 4.15, we get the following:

$$\left[\frac{d^2 A_3}{dz^2} + 2ik_3\frac{dA_3}{dz} - k_3^2 A_3 + \frac{\omega_3^2}{c^2}\widetilde{n}_3^2 A_3\right] e^{ik_3 z} = -\frac{\omega_3^2}{c^2}\chi^{(3)} A_1^3 e^{3ik_1 z} \tag{4.17}$$

where an analogous result is found for the complex conjugate. Because $k_3^2 = \frac{\omega_3^2}{c^2}\widetilde{n}_3^2$, the third and fourth terms on the left cancel. If we assume that the amplitude of the third-harmonic field varies slowly compared to the wavelength (the "slowly varying amplitude approximation"), we can state the following:

$$\left|\frac{d^2 A_3}{dz^2}\right| \ll \left|k_3 \frac{dA_3}{dz}\right|$$

and ignore the second spatial derivative in equation 4.17. Let us now consider the case where we have absorption of the THG signal (*i.e.* $\widetilde{n}_3 = n_3 + i\kappa$). Rearranging, we now have:

$$\frac{dA_3}{dz} = \frac{3i\omega_1}{2(n_3 + i\kappa)c}\chi^{(3)} A_1^3 e^{i(\Delta k + i\alpha)z} \tag{4.18}$$

where $\Delta k \equiv \frac{6\pi}{\lambda_1}(n_1 \pm n_3)$ is the phase mismatch between the fundamental and forward ($-$) / backward ($+$) propagating third-harmonic and $\alpha = \frac{2\pi\kappa}{\lambda_3}$. We can find an analogous coupled equation for $\frac{dA_1}{dz}$, but we assume the fundamental is relatively unperturbed by our thin flake and follows a regular plane wave solution. We can integrate this expression and find the amplitude of A_3 at some distance

L. We assume that A_1 (the amplitude of the fundamental) is not a function of z (*i.e.* the pump is not depleted). The integral and result are as follows for the forward propagating wave:

$$\int_{A_3(0)}^{A_3(L)} dE_3 = \frac{3i\omega_1}{2(n_3 + i\kappa)c}\chi^{(3)} A_1^3 \int_0^L e^{i(\Delta k + i\alpha)z} dz$$
$$A_3(L) = \frac{3i\omega_1 L}{2(n_3 + i\kappa)c}\chi^{(3)} A_1^3 \left(\frac{e^{i(\Delta k + i\alpha)L} - 1}{i(\Delta k + i\alpha)L}\right)$$

where we have naturally assumed that there is no initial third-harmonic signal present ($A_3(0) = 0$). We can use the equation $I_q(z) = 2\epsilon_0 c n_i |E_q(z)|^2$ (since A_q is half the total amplitude of $E_q(z)$) to find the relationship between the fundamental and third-harmonic intensities:

$$I_3(L) = \frac{9\omega_1^2 L^2}{16|\widetilde{n}_3| n_1^3 \epsilon_0^2 c^4} |\chi^{(3)}|^2 I_1^3 \left|\frac{e^{i(\Delta k + i\alpha)L} - 1}{i(\Delta k + i\alpha)L}\right|^2 e^{-2\alpha L} \tag{4.19}$$

Expanding the part that depends on $\Delta k L$ gives us:

$$\left|\frac{e^{i(\Delta k + i\alpha)L} - 1}{i(\Delta k + i\alpha)L}\right|^2 = \frac{e^{-2\alpha L} - 2\cos(\Delta k L)e^{-\alpha L} + 1}{\alpha^2 L^2 + \Delta k^2 L^2}$$
$$\lim_{\alpha \to 0} \left|\frac{e^{i(\Delta k + i\alpha)L} - 1}{i(\Delta k + i\alpha)L}\right|^2 = \text{sinc}^2\left(\frac{\Delta k L}{2}\right)$$

where we recover the original sinc^2 function in the case of no loss [153]. As long as $L \ll L_{coh} = \pi/\Delta k$, $\text{sinc}^2(\Delta k L/2) \approx 1$ and we can drop this term for forward propagating waves. This is a reasonable assumption for our case where the maximum sample thickness was around 80 nm. From literature, we also estimate that the real part of the refractive index of BP is ($n_1 \approx 3.2, n_3 \approx 3.5$) at the fundamental and third-harmonic wavelengths [50, 154], so the phase-mismatch $\Delta k L$ can be safely ignored. For backward propagating waves, however, $\Delta k = \frac{6\pi}{\lambda_1}(n_1 + n_3)$, leading to a coherence length $L_{coh} = \pi/\Delta k \approx 40$ nm which does affect our results and must be considered. The third-harmonic intensity is therefore:

$$I_3 = \frac{9\omega_1^2 L^2}{16|\widetilde{n}_3| n_1^3 \epsilon_0^2 c^4} |\chi^{(3)}|^2 I_1^3 \left(\frac{e^{-2\alpha L} - 2\cos(\Delta k L)e^{-\alpha L} + 1}{\alpha^2 L^2 + \Delta k^2 L^2}\right) e^{-2\alpha L} \tag{4.20}$$

As one can see from equation 4.20, the intensity of the THG has a cubic dependence on the intensity of the fundamental. This, combined with a spectrum of the emitted light, is a straight-forward way of determining whether the observed signal is THG or something else. In our measurements, we show that both the wavelength of the emitted light and the power dependence agree with the theory we have derived here. It is important to note that when calculating $|\chi^{(3)}|$, the peak intensity of the fundamental and THG must be considered, rather than the average intensity measured by a power meter. The peak intensity can be calculated by taking into account the repetition rate (f_{rep}), pulse width, and spot size of the beam. We assume that the fundamental and THG pulses are Gaussian in both space and time:

$$I(r,t) = I_0 e^{-4\ln 2 (r/W)^2} e^{-4\ln 2 (t/\tau)^2} \tag{4.21}$$

where W and τ are the full width half maximum beam diameter and pulse width respectively. Integrating $I(r,t)$ over time and space gives:

$$\begin{aligned} P_{\text{avg}} &= f_{\text{rep}} \int_{-\infty}^{\infty} I(r,t) dr dt = I_0 f_{\text{rep}} \int_{-\infty}^{\infty} e^{-4\ln 2 (x^2+y^2)/W^2} dx dy \int_{-\infty}^{\infty} e^{-4\ln 2 (t/\tau)^2} dt \\ &= I_0 f_{\text{rep}} \frac{\pi W^2}{4\ln 2} \sqrt{\frac{\pi \tau^2}{4 \ln 2}} = I_0 f_{\text{rep}} W^2 \tau \left[\frac{\pi}{4\ln 2}\right]^{3/2} \end{aligned}$$

We can therefore put equation 4.20 in terms of the measured average power of both the fundamental and third-harmonic:

$$P_3 = \frac{9\omega_1^2 L^2}{16|\widetilde{n}_3| n_1^3 \epsilon_0^2 c^4} |\chi^{(3)}|^2 \frac{P_1^3}{f_{\text{rep}}^2 W^4 \tau^2 \left[\frac{\pi}{4\ln 2}\right]^3} \left(\frac{e^{-2\alpha L} - 2\cos(\Delta k L) e^{-\alpha L} + 1}{\alpha^2 L^2 + \Delta k^2 L^2} \right) e^{-2\alpha L} \tag{4.22}$$

4.8 Sample Preparation and Experimental Setup

To prepare our samples, we used Scotch tape to exfoliate single-crystal BP onto glass slides covered with polydimethylsiloxane (PDMS). It was found that thin flakes with much larger areas could be exfoliated onto PDMS compared to a rigid substrate. Once on the PDMS, suitable BP flakes with multiple layers were identified under an optical microscope and transferred onto silicon substrates coated with 300 nm of thermally grown SiO_2. After transferring the BP, the substrates were immediately placed in an atomic layer deposition (ALD) chamber and coated with 20 nm Al_2O_3 grown at 180 °C for passivation to prevent oxidation of the material.

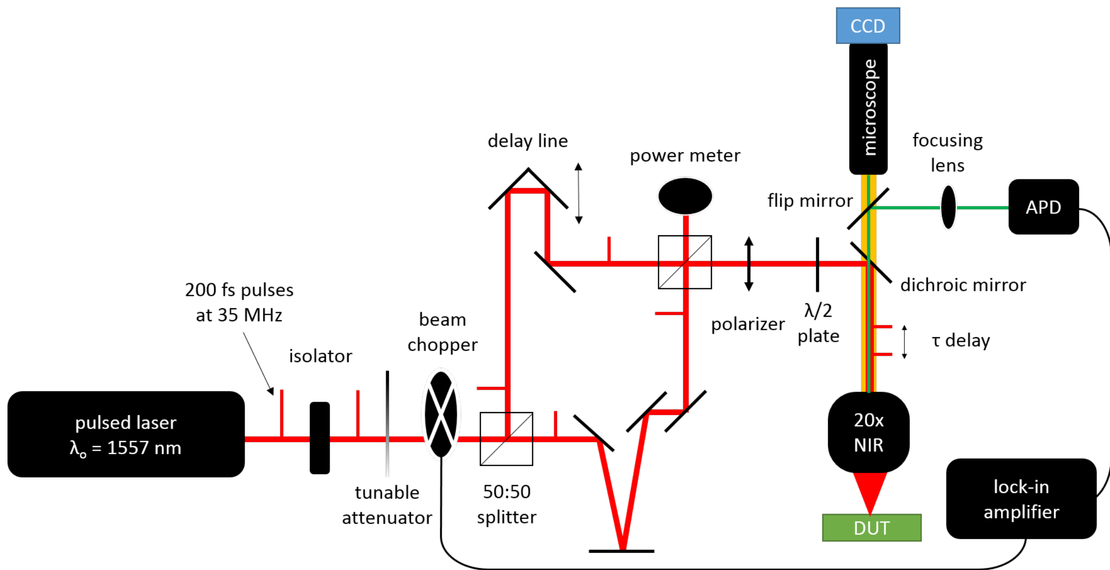

Figure 4.9: Experimental setup used to measure THG in BP. The avalanche photodetector (APD) was replaced with a spectrometer to measure the wavelength of the emitted light. The optical delay line was only used during autocorrelation measurements.

A femtosecond, near-IR fiber laser with a spectrum centered at 1557 nm (photon energy ~0.8 eV) and repetition rate of 35 MHz was used as the pump (200 fs

pulse width and ~4 kW peak power at the sample) to probe the THG response of our samples. Light from the laser was focused onto the sample *via* a near-IR 20× objective (Mitutoyo MPlan NIR, 0.4 NA) with a minimum spot diameter of 6.2 µm as defined by the knife-edge width (the distance between 10% and 90% of the total power). A short-pass dichroic filter (Thorlabs DMSP1000) was used to reflect the fundamental frequency of the pump light toward the sample, while passing the third harmonic. The filtered light was focused onto either a CCD camera, spectrometer, or avalanche photodetector (APD) depending on the measurement. An Ocean Optics "USB4000-UV-VIS" spectrometer was used to measure the wavelength of the emitted light. A simple bi-convex lens with a 7.5 cm focal length was used to focus the THG emitted light onto either the multimode fiber of the spectrometer or active area of the APD. An optical chopper (SR540) and lock-in amplifier (SR830) were used to enhance the SNR of the THG power measured by the APD. For autocorrelation measurements, an optical delay line (Aerotech PRO115) was used to vary the time delay between two pulses. The complete experimental setup can be seen in Figure 4.9.

4.9 Results

Figure 4.10 shows the BP flakes used for THG characterization with the crystal orientation denoted in the lower right-hand side (x- and y-axis indicate the armchair and zigzag directions, respectively). It was first confirmed that the polarization that maximized the photocurrent (light polarized along the x-axis of the BP flake) also maximized the THG using the device in Figure 4.7. Once this was confirmed, the crystal orientation of subsequent flakes were determined by polarization-dependent THG. Figure 4.11a shows a typical spectrum of the third

harmonic measured with a visible spectrometer. As expected, the peak response of the THG signal (519 nm) is exactly one third of the fundamental wavelength of the pump laser (1557 nm). The inset in Figure 4.11a shows the THG emission captured by the CCD camera during a measurement. Further confirmation of THG can be seen in Figure 4.11b, which plots the pump power dependence of the THG power with a power law fit to the experimental data. The fit shows a nearly cubic dependence as expected from equation 4.22.

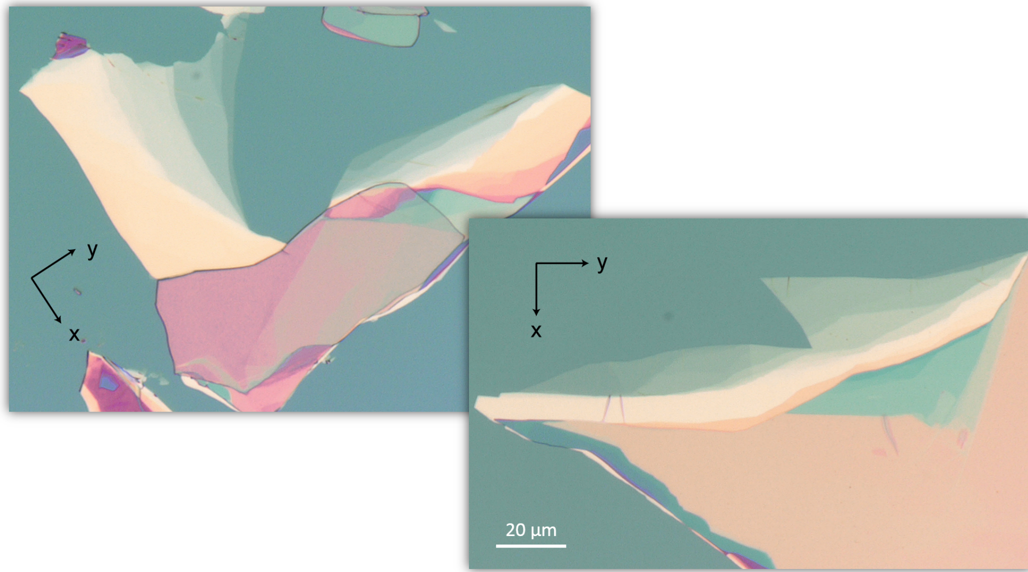

Figure 4.10: Optical images of BP exfoliated onto onto 300 nm SiO_2/Si substrates using a scotch tape and PDMS transfer method. BP was passivated with 20 nm Al_2O_3 to prevent oxidation.

Since the linear optical response of BP shows strong anisotropy with the incident light's polarization [50,54,129], it can be expected that the nonlinear response would show similar anisotropy. The blue triangles in Figure 4.12a show the angular dependence of the THG emission as a function of incident polarization relative

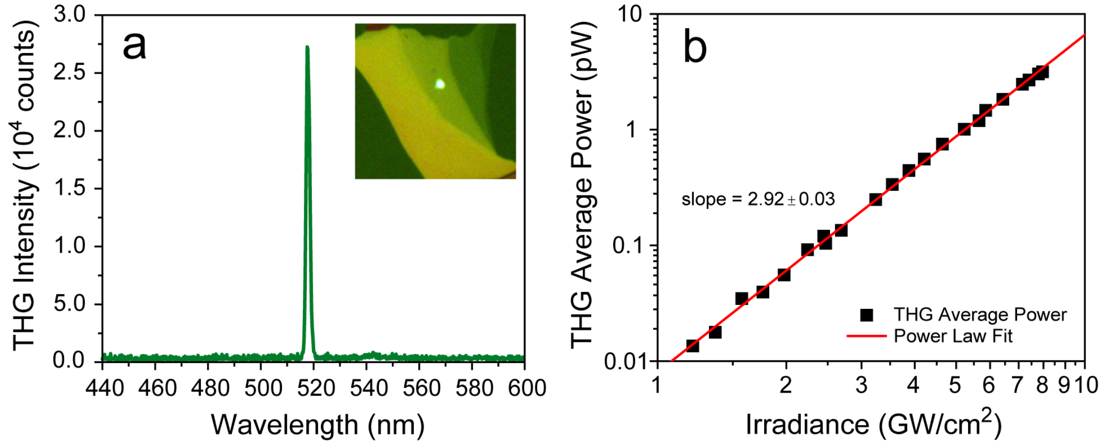

Figure 4.11: Third harmonic generation (THG) in multilayer BP. (a) Spectrum of third-harmonic emission centered at 519 nm. Inset: Image of THG captured with CCD. (b) Power dependence of THG measured using an avalanche photodetector. A fit to the data shows an approximately cubic dependence on the fundamental input power.

to the x-axis (armchair direction) of the crystal. The minimum in the THG corresponds to an incident polarization aligned along the y-axis (zigzag direction) of the crystal. This was verified by photocurrent measurements on other BP flakes with a similar thickness. The polarization angle that minimized the photocurrent (as seen in Yuan et al. [42]) also minimized the emitted THG power. To extract the polarization dependence of the THG emission, an analyzer was placed in front of the APD and fixed at either 0 or 90 degrees while a near-IR, half-wave plate was rotated in 5-degree steps to change the linear polarization of the pump laser. The black and red data points in Figures 4.12a and b correspond to the measured intensity of the $x-$ and y-polarized light, respectively.

BP has an orthorhombic crystal structure and is in the space group Cmca [155]. Knowing this, we can write the contracted third-order nonlinear susceptibility

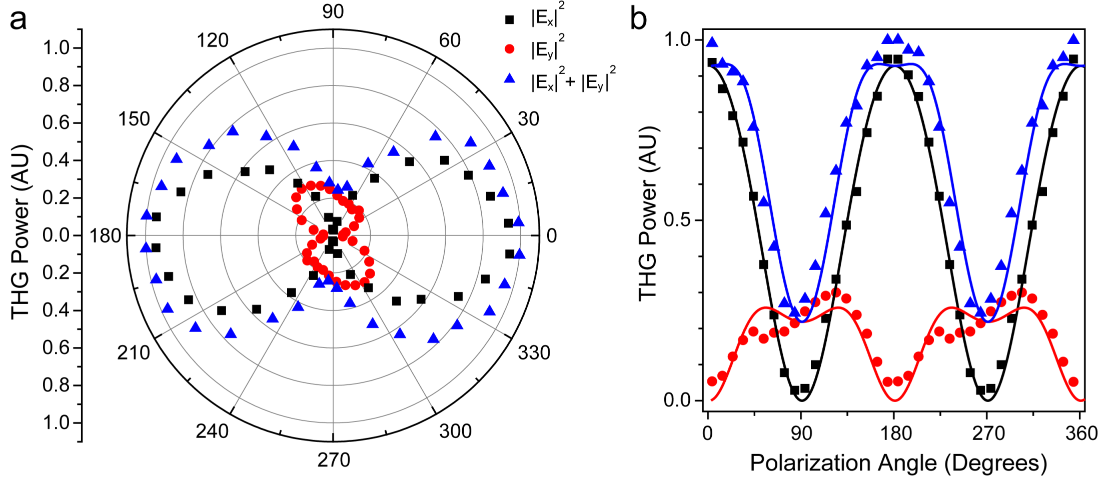

Figure 4.12: Anisotropic THG in BP. (a) Polar plot of normalized THG average power verses polarization angle. x-axis is set to be 0 degrees. (b) Same data as in (a) with theoretical fits using equation 4.26 to the intensity polarized in the x (black squares) and y (red dots) directions. Blue triangles correspond to the total intensity.

tensor for an orthorhombic crystal exhibiting THG as follows [156]:

$$\begin{bmatrix} \chi_{11} & 0 & 0 & 0 & 0 & \chi_{16} & 0 & \chi_{18} & 0 & 0 \\ 0 & \chi_{22} & 0 & \chi_{24} & 0 & 0 & 0 & 0 & \chi_{29} & 0 \\ 0 & 0 & \chi_{33} & 0 & \chi_{35} & 0 & \chi_{37} & 0 & 0 & 0 \end{bmatrix} \tag{4.23}$$

where the first subscript "1, 2, 3" refer to "x, y, z" respectively and the second subscript signifies the following:

jkl	xxx	yyy	zzz	yzz	yyz	xzz	xxz	xyy	xxy	xyz
m	1	2	3	4	5	6	7	8	9	0

The effective third-order susceptibility is contracted using the following equation:

$$\chi^{(3)}_{\text{eff},i} = \mathbf{e}_i \cdot [\chi^{(3)}_{im}] \cdot [\mathbf{e}_m] \tag{4.24}$$

where $\mathbf{e}_i$ is the unit vector in the $i = x, y$, or z direction and $[\mathbf{e}_m]$ is defined as follows:

$$[\mathbf{e}_m] = \begin{cases} L_{xxx} \\ L_{yyy} \\ L_{zzz} \\ L_{yzz} + L_{zyz} + L_{zzy} \\ L_{yyz} + L_{yzy} + L_{zyy} \\ L_{xzz} + L_{zxz} + L_{zzx} \\ L_{xxz} + L_{xzx} + L_{zxx} \\ L_{xyy} + L_{yxy} + L_{yyx} \\ L_{xxy} + L_{xyx} + L_{yxx} \\ L_{xyz} + L_{xzy} + L_{yxz} + L_{yzx} + L_{zxy} + L_{zyx} \end{cases}$$

$$L_{uvw} = \mathbf{e}_u(\omega_1)\mathbf{e}_v(\omega_1)\mathbf{e}_w(\omega_1)$$

Since we are only exciting in the x-y plane in our configuration, the electric field can be written as follows:

$$\widetilde{\mathbf{E}} = E_1(\hat{\mathbf{x}}\cos(\theta) + \hat{\mathbf{y}}\sin(\theta)), \quad \mathbf{e}_x = \hat{\mathbf{x}}\cos(\theta), \quad \mathbf{e}_y = \hat{\mathbf{y}}\sin(\theta) \tag{4.25}$$

so we can write $[\mathbf{e}_m]$ as follows:

$$[\mathbf{e}_m] = [\cos^3(\theta),\ \sin^3(\theta),\ 0,\ 0,\ 0,\ 0,\ 0,\ 3\cos(\theta)\sin^2(\theta),\ 3\cos^2(\theta)\sin(\theta),\ 0]$$

When we substitute this into equation 4.24, we are left with only four non-zero matrix elements $(\chi_{11}, \chi_{22}, \chi_{18}, \chi_{29})$, which determine the THG in BP. Because the

third-harmonic electric field is proportional to the nonlinear susceptibility and we can write the THG output intensity as follows:

$$\begin{aligned} |E_x|^2 &\propto \left|\chi_{11} E_1^3 \cos^3(\theta) + 3\chi_{18} E_1^3 \cos(\theta)\sin^2(\theta)\right|^2 \\ |E_y|^2 &\propto \left|\chi_{22} E_1^3 \sin^3(\theta) + 3\chi_{29} E_1^3 \sin(\theta)\cos^2(\theta)\right|^2 \end{aligned} \tag{4.26}$$

where θ is the polarization angle relative to the x-axis of the crystal and E_1 is the magnitude of the fundamental electric field. The solid lines in Figure 4.12b are fits to the measured intensity in the x and y directions using the relationships in Equation 4.26. One can see good agreement with the overall fit, excluding some asymmetry in the $|E_y|^2$ data. This asymmetry is likely caused by some residual polarization dependence in the transmission of the dichroic mirror that we were not able to account for during the measurement.

To further characterize the nature of THG in BP, we recorded the power of the THG signal as a function of position by scanning the sample in an x-y grid of 500 nm increments. This allowed us to create a two-dimensional map of the THG power as can be seen in Figure 4.13b. We also used atomic force microscopy (AFM) to measure the topography of the various layers present in the same region (Figure 4.13a). A few wrinkles can be seen in the AFM image that are due to the PDMS transfer process. Interestingly, the two larger wrinkles at the top of the flake can also be seen in the THG map of Figure 4.13b. Modulation in the optical properties of wrinkled BP has recently been studied where the strain due to wrinkles strongly modifies the band structure and therefore the optical properties of BP [157].

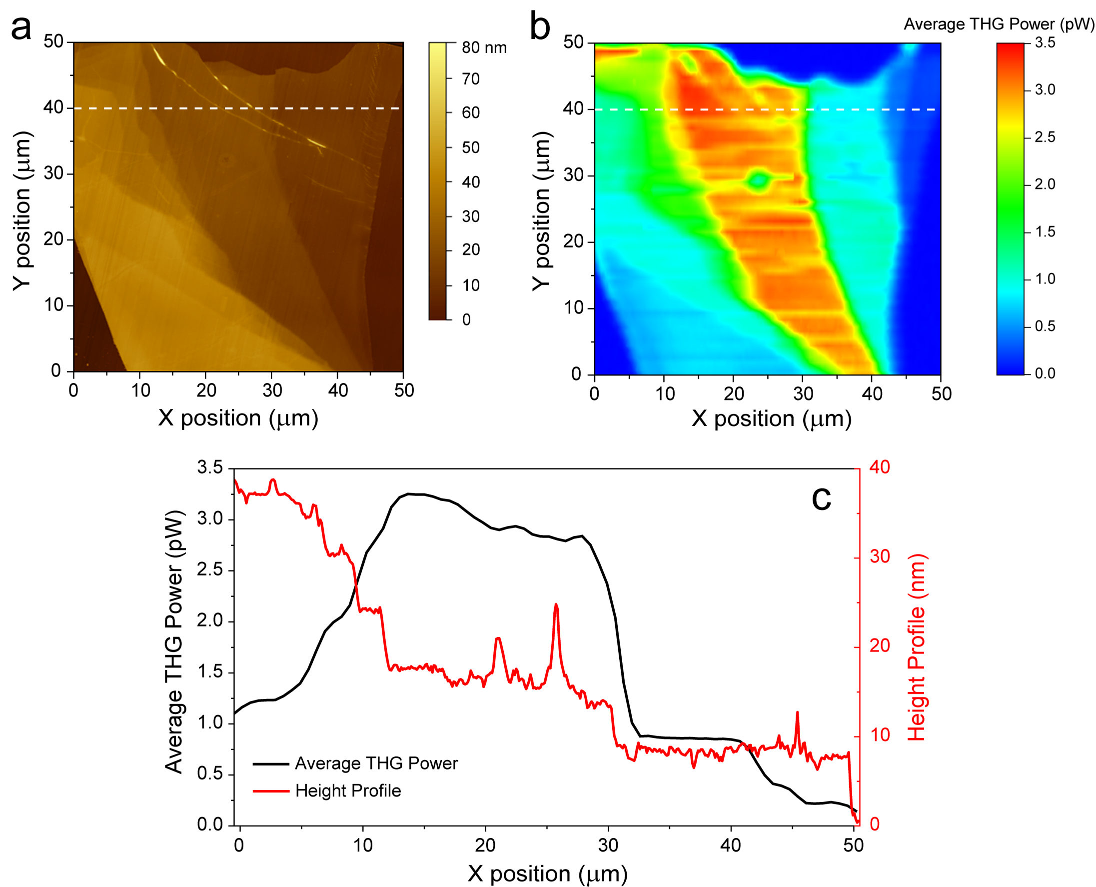

Figure 4.13: (a) AFM height profile of flake from Figure 4.11 containing many layers of various thicknesses. (b) Position dependent THG signal measured by scanning the position of the beam relative to the sample. Different thicknesses can be resolved via contrast in the THG signal. (c) Profiles of both the height and THG power extracted from the white cut-lines shown in (a) and (b). THG can show higher contrast than AFM for flake thicknesses less than 15 nm.

Figure 4.13c shows the cut-lines for both the topography and THG images denoted by the white lines in Figures 4.13a and b. One can see that the THG varies significantly as a function of position, but is relatively constant for a fixed flake thickness. Additionally, for thicknesses less than 15 nm, there is much higher contrast between various thicknesses in the THG image compared to the AFM image. We attribute this significant change in the THG power to be partially due to interference of the fundamental and third-harmonic with the substrate, but largely due to the phase-mismatch between the pump and THG and absorption of the third-harmonic signal by the BP layers.

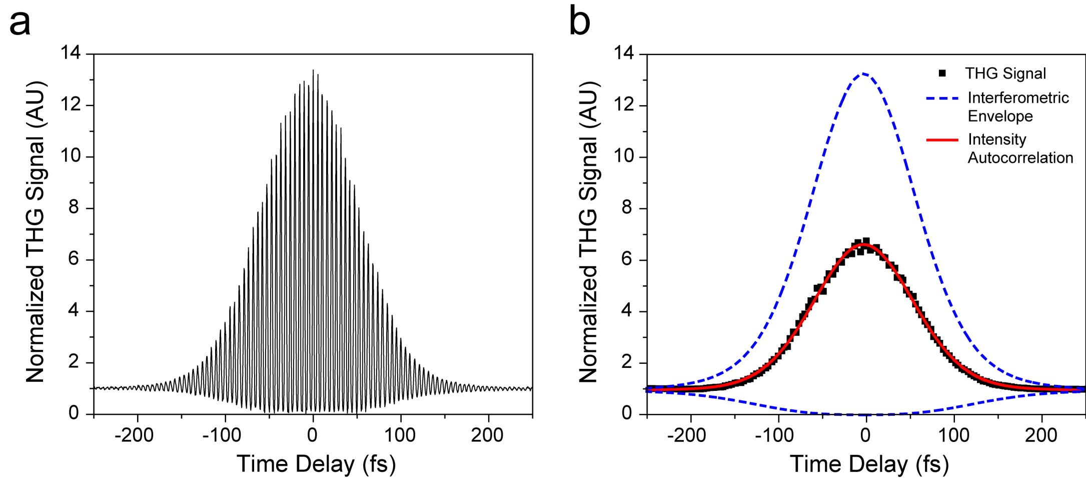

Figure 4.14: Autocorrelation measurement using THG from BP. (a) Third-harmonic interferometric autocorrelation of the THG emission from BP. (b) The intensity autocorrelation of the THG emission. Theoretical fit to data (red line) using a 155 fs hyperbolic sech^2 pulse. Dashed blue lines show the theoretical interferometric autocorrelation envelope.

In a final experiment, we measured the temporal pulse width of our laser by recording the interferometric and intensity autocorrelation using the THG signal from BP. The output pulse of the ultrafast laser was split into two using a 50:50

beam splitter and one pulse was delayed relative to the other using a linear stage. The two pulses were then recombined on a second beam splitter and focused onto the sample. The experimental setup can be seen in Figure 4.9. The THG interferometric autocorrelation signal can be written as [158]:

$$I^{(3\omega)}(\tau) = \int \left|\{A(t)\cos(\omega t) + A(t-\tau)\cos[\omega(t-\tau)]\}^3\right|^2 dt \qquad (4.27)$$

In this case, $E(t) = A(t)\cos(\omega t)$ is the electric field of the ultrafast pulse, with amplitude $A(t)$ and angular frequency ω. The interferometric autocorrelation from the THG signal (shown in Figure 4.14a) was measured using the slowest speed of the linear stage and a short integration time on the lock-in amplifier. In order to measure the intensity autocorrelation, which averages out the cosine terms in Equation 4.27 and is easier to fit numerically, we increased the integration time of the lock-in amplifier. The resulting data and fit using a 155 fs sech^2 pulse (red line) can be seen in Figure 4.14b with the theoretical interferometric autocorrelation envelope included as dashed blue lines. For the ideal case, we would expect to see an extinction ratio of 32:1 in the THG interferometric autocorrelation. However, we see that the extinction ratio is 14:1 which indicates a less than perfect power balance or spacial overlap between the pump and probe beams. This could also explain the discrepancy between the measured pulse width of 155 fs and the manufacturer's specification of ∼200 fs.

4.10 Discussion

By measuring the average THG power at different positions from Figure 4.13b and relating it to the height from AFM data in Figure 4.13a, the THG power as a function of thickness can be extracted. Figure 4.15 plots the average THG power verses BP thickness. This thickness dependence can be primarily understood by

two competing mechanisms. The first is a quadratic increase in the third-harmonic signal with thickness that is proportional to the number of layers squared. This makes sense for our flakes in the range of 6–15 nm where the thickness is less than the coherence length ($L^B_{coh} = \frac{\lambda}{6(n_1+n_3)} \approx 40\,\text{nm}$ and $L^F_{coh} = \frac{\lambda}{6(n_1-n_3)} \approx 870\,\text{nm}$). As the thickness increases, however, the strong absorption of BP at visible wavelengths contributes to significant loss as the third-harmonic signal propagates back through the flake. This can be observed in the exponential decay of the signal at thicknesses greater than 15 nm. Fitting the experimental data with an exponential decay, we estimate the imaginary part of the refractive index to be $k \approx 2.5i$. In order to account for absorption of the third-harmonic signal and interference effects of both the fundamental and third-harmonic signal, we performed FDTD simulations using Lumerical Solutions and compared the simulation results with our experimental measurements. As can be seen from figure 4.15a, there is good agreement between the experimental and simulation results. However, at small BP thicknesses ($< 10\,\text{nm}$), the simulation shows the same trend as the experiment, but the absolute values deviate as the flake thickness decreases. One possible explanation is that the exfoliation, transfer, and Al_2O_3 growth negatively affect the first few layers which accounts for a larger fraction of the total flake for thinner flakes, thus reducing the THG yield. Further studies using a glovebox and van der Waals passivation could shed light on this discrepancy.

In order to intuitively understand the general trend in figure 4.15a, we plot the thickness dependent portion of the analytical solution for THG we obtained by solving nonlinear Maxwells equations (see equation 4.20):

$$I_3(d) = A(\omega)|\chi^{(3)}|^2 I_1^3 \left(\frac{e^{-2\alpha d} - 2\cos(\Delta k d)e^{-\alpha d} + 1}{\alpha^2 + \Delta k^2} \right) e^{-2\alpha d} \tag{4.28}$$

where d is the thickness of the BP flake, α is the absorption coefficient of the THG signal, and $A(\omega)$ is a scaling factor which includes physical constants and

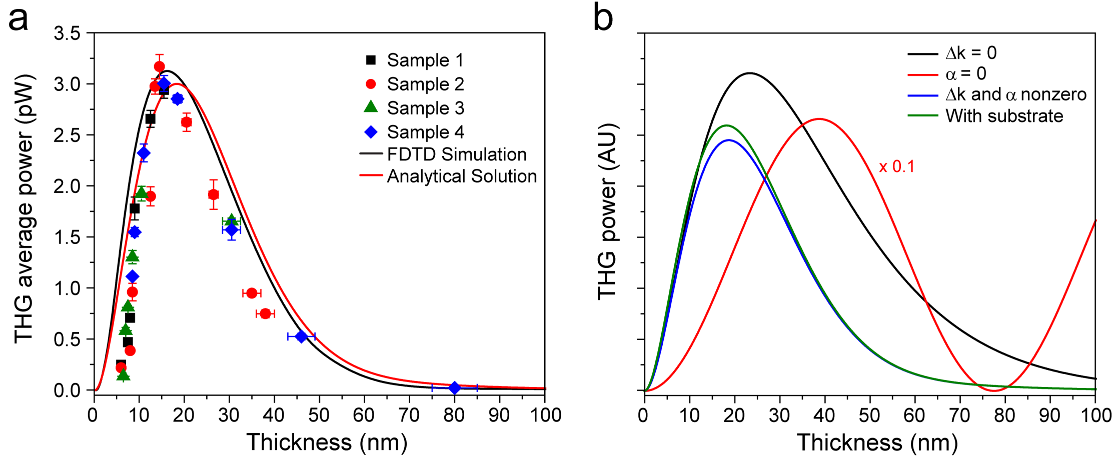

Figure 4.15: Thickness dependent THG in BP. (a) THG average power plotted verses thickness. Data was extracted from the AFM and THG map of four BP flakes. The solid line corresponds to full FDTD simulation where $\chi^{(3)}$ was assumed to be constant and the thickness of the BP layer was varied on a 300 nm SiO_2/Si substrate. (b) Analytical model of THG in BP showing the contributions of optical absorption, phase mismatch, and reflection from substrate.

the refractive indices at ω and 3ω. The results of this analytical model can be seen in 4.15b where we compare the various effects that optical absorption, phase mismatch, and reflection from substrate have on the general shape of the curve. We note that although this analytical solution does not consider the absorption and interference of the fundamental pump, simply taking into account the phase mismatch and the absorption of the third-harmonic is enough to describe the general trend we observe in the data. The full FDTD simulations we performed in figure 4.15a account for these secondary effects.

It is possible to extract the magnitude of $\chi^{(3)}$ at the peak response (14.5 nm thick) using the result for a thin bulk sample with loss we derived previously in equation 4.22. Taking into account the average power, repetition rate, and spot size of the ultrafast laser (30 mW, 35 MHz, and 5.7 µm diameter at FWHM) and the refractive index of BP ($n_1 \approx 3.2 + 0.2i, n_3 \approx 3.5 + 2.5i$) [50, 154], we estimate

the magnitude of $\chi^{(3)}$ to be $1.4 \times 10^{-19}\,\mathrm{m^2/V^2}$. Table 4.1 compares our results with THG in other 2D materials.

Material	# Layers	$\chi^{(3)}$ $\mathrm{m^2/V^2}$	λ_1 (nm)	Reference
BP	29	1.4×10^{-19}	1557	this work
MoS_2	1	2.9×10^{-19}	1560	[142]
MoS_2	>7	$\sim 10^{-19}$	1758	[143]
MoS_2	1 to 7	3.9×10^{-15}	1560	[144]
GaSe	9 to 14	1.7×10^{-16}	1560	[159]
Graphene	1	$\sim 10^{-16}$	1720	[140]
Graphene	1	4×10^{-15}	1550	[141]
Graphene	1	1.5×10^{-19}	1560	[142]
Graphene	1 and 2	$\sim 10^{-19}$	789	[139]

Table 4.1: Reported values of $\chi^{(3)}$ for various 2D materials.

Table 4.1 compares our results to the experimentally measured values of $\chi^{(3)}$ in other 2D materials reported in the literature. Something directly evident from table 4.1 is the wide range of reported results for $\chi^{(3)}$ in graphene. This also impacts the estimated $\chi^{(3)}$ for other materials where the authors directly compare the magnitude of THG in MoS_2 and GaSe with a graphene flake on the same substrate and scale $\chi^{(3)}$ accordingly. One explanation is the effect the substrate has on the magnitude of the THG signal observed [160]. Constructive interference of the fundamental pump due to reflections from the substrate can lead to significant enhancements in the power at the graphene layer and lead to overestimates of $\chi^{(3)}$ since the THG signal is proportional to P_1^3. In our FDTD simulations, we found that using $\chi^{(3)} = 10^{-19}\,\mathrm{m^2/V^2}$ gave a very comparable THG power for the same pulse energy that we used in our experiments so we believe our estimate of $\chi^{(3)} = 1.4 \times 10^{-19}\,\mathrm{m^2/V^2}$ to be close to the actual value. Another explanation, as pointed out in [142], is a likely miscalculation in the original estimation of graphene's $\chi^{(3)}$

by Hendry *et al.* [161], which leads to a corrected value of $\sim 10^{-19}\,\mathrm{m}^2/\mathrm{V}^2$ [162].

Our estimate of $\chi^{(3)}$ is typical for other bulk materials that exhibit a strong third-order optical response [153]. It is indeed rather surprising that the magnitude of $\chi^{(3)}$ is comparable to other materials when the excitation energy used is so far above the bandgap. While our initial results are promising, it will be extremely interesting in future works to characterize $\chi^{(3)}$ near the band edge in BP of different thicknesses, which will require a pump photon energy in the mid-IR regime that is not available in our measurement system.

4.11 Conclusion

In conclusion, we have observed nonlinear photoresponse and THG in BP thin films using an ultrafast near-IR laser. We found that a BP photodetector encapsulated by BN could have intrinsic response times on the order of 7 GHz. We also found that the third-order response is highly anisotropic with incident polarization. Additionally, the THG signal showed a strong layer dependence which was limited beyond 15 nm due to strong absorption by BP. Our study shows that multilayer BP has a fast response time and strong nonlinear response comparable with other 2D materials and could show promise for applications in telecommunications and mid-infrared nonlinear optics.

Chapter 5

Concluding Remarks

5.1 Summary

In chapter 1, we have presented a comprehensive review of the current state of waveguide integrated graphene and BP photodetectors and modulators and have presented our research in the context of the broader community.

In chapter 2, we demonstrated the first device to achieve both photo detection and optical modulation using a single geometry by integrating a graphene FET on a silicon waveguide. We also used an integrated MZI to precisely measure the absorption due to graphene and extracted the internal quantum efficiency of our device. Finally, we demonstrated that the device can be operated in both modes simultaneously, potentially leading to novel applications.

In chapter 3, we demonstrated the first waveguide-integrated BP photodetector which demonstrated superior dark current compared to graphene photodetectors. Through use of an integrated MZI, we measure internal quantum efficiencies exceeding 50%. Our device also showed an f_{3dB} six orders of magnitude higher than any other BP photodetector at the time. Through the use of a top gate and

frequency dependent measurements, we found that two independent photocurrent mechanisms were at play in our device.

In chapter 4, we use ultrafast measurement techniques to measure the intrinsic physical properties of BP. An ultrafast pump-probe technique is used to resolve the intrinsic photodetection speed of a BN-BP-BN van der Waal heterostructure. An ultrafast pump is also used to measure the third-order nonlinearity of BP for the first time. Polarization and thickness dependent studies are presented and $\chi^{(3)}$ is experimentally determined.

5.2 Future directions for 2D optoelectronics

There is a bright future for 2D optoelectronics and many novel applications beyond photodetection and modulation have proposed. For example, recent work on TMDC lasers show great promise for the potential of integrated light sources on a photonic circuit [163, 164]. It was recently shown that through the Purcell effect arising from strong interaction between WSe_2 and a PCC, an ultralow threshold laser could be achieved on-chip [163]. While this laser was pumped optically through normal incident light and emission was out-of-plane, it could be possible to have a fully integrated light source that is pumped electrically through use of van der Waals heterostructures and coupled to a waveguide using more sophisticated photonic circuit designs.

Another application is integrated quantum optics using 2D materials on a silicon photonics platform. Theoretical calculations have suggested that TMDCs integrated on a silicon nitride PCC with a modest quality factor ($Q \sim 10^5$–10^6) could allow optical bistability and single-photon blockade devices at low optical powers [165]. This exploits the strong second-order optical nonlinearity observed

in TMDCs [135, 136] which is also electrically tunable [138]. Additionally, this strong second-order susceptibility could potentially be used for parametric down-conversion by integrating TMDCs onto a photonics platform for applications requiring on-chip quantum entanglement such as quantum encryption.

Recent experimental results with various 2D materials have shown further promise for the field of quantum optics. Optically pumped single quantum emitters have been observed in both WSe_2 [166,167] and BN [168]. These single quantum emitters are spatially localized by crystal defects and have linewidths much sharper than their delocalized exciton counterparts. Strong photon anti-bunching is observed as well, confirming single photon emission. Electrically pumped single quantum emitters have also been demonstrated in WSe_2 using vertical van der Waals heterostructures [169, 170]. In both devices, a monolayer of WSe_2 is sandwiched by two few-layer BN flakes and contacted with graphene top and bottom electrodes. This forms a quantum well band structure where electrons tunnel from the graphene electrodes through the BN barriers and radiatively recombine at localized defects in WSe_2, emitting a single photon. While these devices have yet to be integrated on a photonic platform, the path to integration is relatively straight forward and could be used to create on-chip quantum emitters.

A few other potential directions could be the use of van der Waals heterostructures for optical amplification or the generation of mid-IR light using BP. The first case involves transferring a $MoSe_2$ / WSe_2 heterostructure onto a waveguide and creating gain through electrical or optical pumping. Rivera *et al.* demonstrated that due to the type II band alignment between $MoSe_2$ and WSe_2, long-lived inter-layer excitons could exist with a lifetime of 1.8 ns [171]. This is much longer than the expected intra-layer exciton lifetime in the same materials and achieving population inversion could be easier in this system than an isolated monolayer.

More thorough studies of the radiative and non-radiative recombination dynamics of these inter-layer excitons will reveal whether or not optical gain is possible. The second case involves creating a mid-IR LED with BP if non-radiative recombination rates can be reduced. This is especially attractive since the bandgap is layer dependent and emission is expected to be linearly polarized [172].

While the field of integrated optoelectronics with 2D materials is still in its infancy, significant progress has been made toward a fully on-chip optical network. Already high performance photodetectors, modulators, and optical sources have been experimentally demonstrated and further improvements can be expected as more is discovered about this unique family of materials. Next steps involve developing new growth techniques and ways to scale the manufacture of van der Waals heterostructures. This knowledge will enable further optimization of these devices and the potential for novel applications in the near future.

References

[1] Urino, Y.; Nakamura, T.; and Arakawa, Y. "Silicon Optical Interposers for High-Density Optical Interconnects." In L. Pavesi and D.J. Lockwood (editors), "Silicon Photonics III Syst. Appl.", pp. 1–39. Springer Science, 2016. ISBN 978-3-642-10503-6.

[2] Bergman, K.; Shalf, J.; and Hausken, T. "Optical Interconnects and Extreme Computing." *Opt. Photonics News*, *27*, 4: p. 32, apr 2016.

[3] Harrod, W. "A journey to exascale computing." In "Proc. - 2012 SC Companion High Perform. Comput. Netw. Storage Anal. SCC 2012," pp. 1702–1730. IEEE, nov 2012.

[4] "Micron Techology, Inc. - All About HMC."

[5] Cheung, S.; Su, T.; Okamoto, K.; and Yoo, S.J.B. "Ultra-Compact Silicon Photonic 512 512 25 GHz Arrayed Waveguide Grating Router." *IEEE J. Sel. Top. Quantum Electron.*, *20*, 4: pp. 310–316, jul 2014.

[6] Leuthold, J.; Koos, C.; and Freude, W. "Nonlinear silicon photonics." *Nat. Photonics*, *4*, 8: pp. 535–544, aug 2010.

[7] Tsybeskov, L.; Lockwood, D.; and Ichikawa, M. "Silicon Photonics: CMOS Going Optical [Scanning the Issue]." *Proc. IEEE*, *97*, 7: pp. 1161–1165, jul 2009.

[8] Bolkhovityanov, Y.B. and Pchelyakov, O. "GaAs epitaxy on Si substrates: modern status of research and engineering." *Phys. - Uspekhi*, *51*, 5: pp. 437 – 456, may 2008.

[9] Michel, J.; Liu, J.; and Kimerling, L.C. "High-performance Ge-on-Si photodetectors." *Nat. Photonics*, *4*, 8: pp. 527–534, 2010.

[10] Wang, L.; Meric, I.; Huang, P.Y.; Gao, Q.; Gao, Y.; Tran, H.; Taniguchi, T.; Watanabe, K.; Campos, L.M.; Muller, D.A.; Guo, J.; Kim, P.; Hone, J.; Shepard, K.L.; and Dean, C.R. "One-Dimensional Electrical Contact to a Two-Dimensional Material." *Science (80-.).*, *342*, 6158: pp. 614–617, nov 2013.

[11] Nair, R.R.; Blake, P.; Grigorenko, A.N.; Novoselov, K.S.; Booth, T.J.; Stauber, T.; Peres, N.M.R.; and Geim, A.K. "Fine structure constant defines visual transparency of graphene." *Science*, *320*, 5881: p. 1308, jun 2008.

[12] Mak, K.F.; Ju, L.; Wang, F.; and Heinz, T.F. "Optical spectroscopy of graphene: From the far infrared to the ultraviolet.", 2012.

[13] Li, H.; Anugrah, Y.; Koester, S.J.; and Li, M. "Optical absorption in graphene integrated on silicon waveguides." *Appl. Phys. Lett.*, *101*, 11: p. 111110, sep 2012.

[14] Das, S.; Zhang, W.; Demarteau, M.; Hoffmann, A.; Dubey, M.; and Roelofs, A. "Tunable Transport Gap in Phosphorene." *Nano Lett.*, *14*, 10: pp. 5733–5739, oct 2014.

[15] Rudenko, A.N.; Yuan, S.; and Katsnelson, M.I. "Toward a realistic description of multilayer black phosphorus: From G W approximation to large-scale tight-binding simulations." *Phys. Rev. B*, *92*, 8: p. 085419, aug 2015.

[16] Mak, K.F.; He, K.; Shan, J.; and Heinz, T.F. "Control of valley polarization in monolayer MoS2 by optical helicity." *Nat. Nanotechnol.*, *7*, 8: pp. 494–8, aug 2012.

[17] Zeng, H.; Dai, J.; Yao, W.; Xiao, D.; and Cui, X. "Valley polarization in MoS2 monolayers by optical pumping." *Nat. Nanotechnol.*, *7*, 8: pp. 490–3, aug 2012.

[18] Aivazian, G.; Gong, Z.; Jones, A.M.; Chu, R.L.; Yan, J.; Mandrus, D.G.; Zhang, C.; Cobden, D.; Yao, W.; and Xu, X. "Magnetic control of valley pseudospin in monolayer WSe2." *Nat. Phys.*, *advance on*, jan 2015.

[19] Zhang, Y.J.; Oka, T.; Suzuki, R.; Ye, J.T.; and Iwasa, Y. "Electrically Switchable Chiral Light-Emitting Transistor." *Science (80-.).*, *344*, 6185: pp. 725–728, may 2014.

[20] Wang, F.; Zhang, Y.; Tian, C.; Girit, C.; Zettl, A.; Crommie, M.; and Shen, Y.R. "Gate-Variable Optical Transitions in Graphene." *Science (80-.).*, *320*, 5873: pp. 206–209, apr 2008.

[21] Kuzmenko, A.B.; van Heumen, E.; Carbone, F.; and van der Marel, D. "Universal Optical Conductance of Graphite." *Phys. Rev. Lett.*, *100*, 11: p. 117401, mar 2008.

[22] Engel, M.; Steiner, M.; Lombardo, A.; Ferrari, A.C.; Löhneysen, H.v.; Avouris, P.; and Krupke, R. "Lightmatter interaction in a microcavity-controlled graphene transistor." *Nat. Commun.*, *3*: p. 906, jun 2012.

[23] Furchi, M.; Urich, A.; Pospischil, A.; Lilley, G.; Unterrainer, K.; Detz, H.; Klang, P.; Andrews, A.M.; Schrenk, W.; Strasser, G.; and Mueller, T. "Microcavity-Integrated Graphene Photodetector." *Nano Lett.*, *12*, 6: pp. 2773–2777, jun 2012.

[24] Koppens, F.H.L.; Mueller, T.; Avouris, P.; Ferrari, A.C.; Vitiello, M.S.; and Polini, M. "Photodetectors based on graphene, other two-dimensional materials and hybrid systems." *Nat. Nanotechnol.*, *9*, 10: pp. 780–793, oct 2014.

[25] Xia, F.; Mueller, T.; Lin, Y.m.; Valdes-Garcia, A.; and Avouris, P. "Ultrafast graphene photodetector." *Nat. Nanotechnol.*, *4*, 12: pp. 839–843, dec 2009.

[26] Mueller, T.; Xia, F.; and Avouris, P. "Graphene photodetectors for high-speed optical communications." *Nat. Photonics*, *4*, 5: pp. 297–301, mar 2010.

[27] Gan, X.; Shiue, R.J.; Gao, Y.; Meric, I.; Heinz, T.F.; Shepard, K.; Hone, J.; Assefa, S.; and Englund, D. "Chip-integrated ultrafast graphene photodetector with high responsivity." *Nat. Photonics*, *7*, 11: pp. 883–887, sep 2013.

[28] Wang, X.; Cheng, Z.; Xu, K.; Tsang, H.K.; and Xu, J.B. "High-responsivity graphene/silicon-heterostructure waveguide photodetectors." *Nat. Photonics*, *advance on*, sep 2013.

[29] Pospischil, A.; Humer, M.; Furchi, M.M.; Bachmann, D.; Guider, R.; Fromherz, T.; and Mueller, T. "CMOS-compatible graphene photodetector covering all optical communication bands." *Nat. Photonics*, *7*, 11: pp. 892–896, sep 2013.

[30] Shiue, R.J.; Gao, Y.; Wang, Y.; Peng, C.; Robertson, A.D.; Efetov, D.K.; Assefa, S.; Koppens, F.H.L.; Hone, J.; and Englund, D. "High-Responsivity Graphene-Boron Nitride Photodetector and Autocorrelator in a Silicon Photonic Integrated Circuit." *Nano Lett.*, *15*, 11: pp. 7288–7293, nov 2015.

[31] Youngblood, N.; Anugrah, Y.; Ma, R.; Koester, S.J.; and Li, M. "Multifunctional Graphene Optical Modulator and Photodetector Integrated on Silicon Waveguides." *Nano Lett.*, *14*, 5: pp. 2741–2746, may 2014.

[32] Zhou, H.; Gu, T.; McMillan, J.F.; Yu, M.; Lo, G.; Kwong, D.L.; Feng, G.; Zhou, S.; and Wong, C.W. "Enhanced photoresponsivity in graphene-silicon slow-light photonic crystal waveguides." *Appl. Phys. Lett.*, *108*, 11: p. 111106, mar 2016.

[33] Shiue, R.J.; Gan, X.; Gao, Y.; Li, L.; Yao, X.; Szep, A.; Walker, D.; Hone, J.; and Englund, D. "Enhanced photodetection in graphene-integrated photonic crystal cavity." *Appl. Phys. Lett.*, *103*, 24: p. 241109, 2013.

[34] Urich, A.; Unterrainer, K.; and Mueller, T. "Intrinsic response time of graphene photodetectors." *Nano Lett.*, *11*, 7: pp. 2804–2808, jul 2011.

[35] Sun, D.; Aivazian, G.; Jones, A.M.; Ross, J.S.; Yao, W.; Cobden, D.; and Xu, X. "Ultrafast hot-carrier-dominated photocurrent in graphene." *Nat. Nanotechnol.*, *7*, 2: pp. 114–8, feb 2012.

[36] Schall, D.; Neumaier, D.; Mohsin, M.; Chmielak, B.; Bolten, J.; Porschatis, C.; Prinzen, A.; Matheisen, C.; Kuebart, W.; Junginger, B.; Templ, W.; Giesecke, A.L.; and Kurz, H. "50 GBit/s Photodetectors Based on Wafer-Scale Graphene for Integrated Silicon Photonic Communication Systems." *ACS Photonics*, *1*, 9: pp. 781–784, sep 2014.

[37] Dean, C.R.; Young, a.F.; Meric, I.; Lee, C.; Wang, L.; Sorgenfrei, S.; Watanabe, K.; Taniguchi, T.; Kim, P.; Shepard, K.L.; and Hone, J. "Boron nitride substrates for high-quality graphene electronics." *Nat. Nanotechnol.*, *5*, 10: pp. 722–726, 2010.

[38] Furchi, M.M.; Polyushkin, D.K.; Pospischil, A.; and Mueller, T. "Mechanisms of Photoconductivity in Atomically Thin MoS2." *Nano Lett.*, *14*: pp. 6165–6170, 2014.

[39] Castellanos-Gomez, A. "Black Phosphorus: Narrow Gap, Wide Applications." *J. Phys. Chem. Lett.*, *6*, 21: pp. 4280–4291, nov 2015.

[40] Massicotte, M.; Schmidt, P.; Vialla, F.; Schädler, K.G.; Reserbat-Plantey, A.; Watanabe, K.; Taniguchi, T.; Tielrooij, K.J.; and Koppens, F.H.L. "Picosecond photoresponse in van der Waals heterostructures." *Nat. Nanotechnol.*, *11*, 1: pp. 42–46, oct 2015.

[41] Buscema, M.; Groenendijk, D.J.; Blanter, S.I.; Steele, G.A.; van der Zant, H.S.J.; and Castellanos-Gomez, A. "Fast and Broadband Photoresponse of

Few-Layer Black Phosphorus Field-Effect Transistors." *Nano Lett.*, *14*, 6: pp. 3347–3352, jun 2014.

[42] Yuan, H.; Liu, X.; Afshinmanesh, F.; Li, W.; Xu, G.; Sun, J.; Lian, B.; Curto, A.G.; Ye, G.; Hikita, Y.; Shen, Z.; Zhang, S.C.; Chen, X.; Brongersma, M.; Hwang, H.Y.; and Cui, Y. "Polarization-sensitive broadband photodetector using a black phosphorus vertical p-n junction." *Nat. Nanotechnol.*, *10*, 8: pp. 707–13, aug 2015.

[43] Youngblood, N.; Chen, C.; Koester, S.J.; and Li, M. "Waveguide-integrated black phosphorus photodetector with high responsivity and low dark current." *Nat. Photonics*, *9*, April: pp. 249–252, 2015.

[44] Doganov, R.A.; O'Farrell, E.C.T.; Koenig, S.P.; Yeo, Y.; Ziletti, A.; Carvalho, A.; Campbell, D.K.; Coker, D.F.; Watanabe, K.; Taniguchi, T.; Neto, A.H.C.; and Özyilmaz, B. "Transport properties of pristine few-layer black phosphorus by van der Waals passivation in an inert atmosphere." *Nat. Commun.*, *6*: p. 6647, jan 2015.

[45] Li, L.; Yu, Y.; Ye, G.J.; Ge, Q.; Ou, X.; Wu, H.; Feng, D.; Chen, X.H.; and Zhang, Y. "Black phosphorus field-effect transistors." *Nat. Nanotechnol.*, *9*, 5: pp. 372–377, mar 2014.

[46] Guo, Q.; Pospischil, A.; Bhuiyan, M.; Jiang, H.; Tian, H.; Farmer, D.; Deng, B.; Li, C.; Han, S.J.J.; Wang, H.; Xia, Q.; Ma, T.P.P.; Mueller, T.; and Xia, F. "Black Phosphorus Mid-Infrared Photodetectors with High Gain." *Nano Lett.*, *16*, 7: pp. 4648–4655, jun 2016.

[47] Buscema, M.; Groenendijk, D.J.; Steele, G.A.; van der Zant, H.S.; and Castellanos-Gomez, A. "Photovoltaic effect in few-layer black phosphorus

PN junctions defined by local electrostatic gating." *Nat. Commun.*, *5*: p. 4651, aug 2014.

[48] Low, T.; Engel, M.; Steiner, M.; and Avouris, P. "Origin of photoresponse in black phosphorus phototransistors." *Phys. Rev. B*, *90*, 8: p. 081408, aug 2014.

[49] Engel, M.; Steiner, M.; and Avouris, P. "Black Phosphorus Photodetector for Multispectral, High-Resolution Imaging." *Nano Lett.*, *14*, 11: pp. 6414–6417, nov 2014.

[50] Low, T.; Rodin, A.S.; Carvalho, A.; Jiang, Y.; Wang, H.; Xia, F.; and Castro Neto, A.H. "Tunable optical properties of multilayer black phosphorus thin films." *Phys. Rev. B*, *90*, 7: p. 075434, aug 2014.

[51] Liu, B.; Köpf, M.; Abbas, A.N.; Wang, X.; Guo, Q.; Jia, Y.; Xia, F.; Weihrich, R.; Bachhuber, F.; Pielnhofer, F.; Wang, H.; Dhall, R.; Cronin, S.B.; Ge, M.; Fang, X.; Nilges, T.; and Zhou, C. "Black Arsenic-Phosphorus: Layered Anisotropic Infrared Semiconductors with Highly Tunable Compositions and Properties." *Adv. Mater.*, *27*, 30: pp. 4423–4429, aug 2015.

[52] Chen, X.; Wu, Y.; Wu, Z.; Han, Y.; Xu, S.; Wang, L.; Ye, W.; Han, T.; He, Y.; Cai, Y.; and Wang, N. "High-quality sandwiched black phosphorus heterostructure and its quantum oscillations." *Nat. Commun.*, *6*: p. 7315, 2015.

[53] Akahama, Y.; Endo, S.; and Narita, S.i. "Electrical Properties of Black Phosphorus Single Crystals.", 1983.

[54] Xia, F.; Wang, H.; and Jia, Y. "Rediscovering black phosphorus as an anisotropic layered material for optoelectronics and electronics." *Nat. Commun.*, *5*: p. 4458, jul 2014.

[55] Fei, R.; Faghaninia, A.; Soklaski, R.; Yan, J.A.; Lo, C.; and Yang, L. "Enhanced Thermoelectric Efficiency via Orthogonal Electrical and Thermal Conductances in Phosphorene.", 2014.

[56] Qin, G.Z.; Yan, Q.B.; Qin, Z.Z.; Yue, S.Y.; Hu, M.; and Su, G. "Anisotropic intrinsic lattice thermal conductivity of phosphorene from first principles." *Phys. Chem. Chem. Phys.*, *17*, 7: pp. 4854–4858, 2015.

[57] Luo, Z.; Maassen, J.; Deng, Y.; Du, Y.; Garrelts, R.P.; Lundstrom, M.S.; Ye, P.D.; and Xu, X. "Anisotropic in-plane thermal conductivity observed in few-layer black phosphorus." *Nat. Commun.*, *6*: p. 8572, oct 2015.

[58] Assefa, S.; Xia, F.; Bedell, S.W.; Zhang, Y.; Topuria, T.; Rice, P.M.; and Vlasov, Y.A. "CMOS-integrated high-speed MSM germanium waveguide photodetector." *Opt. Express*, *18*, 5: p. 4986, mar 2010.

[59] Favron, A.; Gaufrès, E.; Fossard, F.; Phaneuf-L'Heureux, A.L.; Tang, N.Y.W.; Lévesque, P.L.; Loiseau, A.; Leonelli, R.; Francoeur, S.; and Martel, R. "Photooxidation and quantum confinement effects in exfoliated black phosphorus." *Nat. Mater.*, *14*, 8: pp. 826–832, may 2015.

[60] Wood, J.D.; Wells, S.A.; Jariwala, D.; Chen, K.S.; Cho, E.; Sangwan, V.K.; Liu, X.; Lauhon, L.J.; Marks, T.J.; and Hersam, M.C. "Effective passivation of exfoliated black phosphorus transistors against ambient degradation." *Nano Lett.*, *14*, 12: pp. 6964–6970, 2014.

[61] Das, A.; Pisana, S.; Chakraborty, B.; Piscanec, S.; Saha, S.K.; Waghmare, U.V.; Novoselov, K.S.; Krishnamurthy, H.R.; Geim, A.K.; Ferrari, A.C.; and Sood, A.K. "Monitoring dopants by Raman scattering in an electrochemically top-gated graphene transistor." *Nat. Nanotechnol.*, *3*, 4: pp. 210–5, apr 2008.

[62] Liu, M.; Yin, X.; Ulin-Avila, E.; Geng, B.; Zentgraf, T.; Ju, L.; Wang, F.; and Zhang, X. "A graphene-based broadband optical modulator." *Nature*, *474*, 7349: pp. 64–7, jun 2011.

[63] Koester, S.J. and Li, M. "High-speed waveguide-coupled graphene-on-graphene optical modulators." *Appl. Phys. Lett.*, *100*, 17: p. 171107, apr 2012.

[64] Liu, M.; Yin, X.; and Zhang, X. "Double-layer graphene optical modulator." *Nano Lett.*, *12*, 3: pp. 1482–5, mar 2012.

[65] Mohsin, M.; Schall, D.; Otto, M.; Noculak, A.; Neumaier, D.; and Kurz, H. "Graphene based low insertion loss electro-absorption modulator on SOI waveguide." *Opt. Express*, *22*, 12: p. 15292, jun 2014.

[66] Hu, Y.; Pantouvaki, M.; Van Campenhout, J.; Brems, S.; Asselberghs, I.; Huyghebaert, C.; Absil, P.; and Van Thourhout, D. "Broadband 10 Gb/s operation of graphene electro-absorption modulator on silicon." *Laser Photon. Rev.*, *10*, 2: pp. 307–316, mar 2016.

[67] Koester, S.J.; Li, H.; and Li, M. "Switching energy limits of waveguide-coupled graphene-on-graphene optical modulators." *Opt. Express*, *20*, 18: pp. 20330–41, aug 2012.

[68] Gan, X.; Shiue, R.J.; Gao, Y.; Mak, K.F.; Yao, X.; Li, L.; Szep, A.; Walker, D.; Hone, J.; Heinz, T.F.; and Englund, D. "High-contrast electrooptic modulation of a photonic crystal nanocavity by electrical gating of graphene." *Nano Lett.*, *13*, 2: pp. 691–696, feb 2013.

[69] Majumdar, A.; Kim, J.; Vuckovic, J.; and Wang, F. "Electrical control of silicon photonic crystal cavity by graphene." *Nano Lett.*, *13*, 2: pp. 515–518, feb 2013.

[70] Gao, Y.; Shiue, R.J.; Gan, X.; Li, L.; Peng, C.; Meric, I.; Wang, L.; Szep, A.; Walker, D.; Hone, J.; and Englund, D. "High-speed electro-optic modulator integrated with graphene-boron nitride heterostructure and photonic crystal nanocavity." *Nano Lett.*, *15*, 3: pp. 2001–5, mar 2015.

[71] Qiu, C.; Gao, W.; Vajtai, R.; Ajayan, P.M.; Kono, J.; and Xu, Q. "Efficient Modulation of 1.55 μm Radiation with Gated Graphene on a Silicon Microring Resonator." *Nano Lett.*, *14*, 12: pp. 6811–6815, dec 2014.

[72] Ding, Y.; Zhu, X.; Xiao, S.; Hu, H.; Frandsen, L.H.; Mortensen, N.A.; and Yvind, K. "Effective Electro-Optical Modulation with High Extinction Ratio by a Graphene-Silicon Microring Resonator." *Nano Lett.*, *15*, 7: pp. 4393–400, jul 2015.

[73] Phare, C.T.; Daniel Lee, Y.H.; Cardenas, J.; and Lipson, M. "Graphene electro-optic modulator with 30GHz bandwidth." *Nat. Photonics*, *9*, 8: pp. 511–514, jul 2015.

[74] Yu, L.; Dai, D.; and He, S. "Graphene-based transparent flexible heat conductor for thermally tuning nanophotonic integrated devices." *Appl. Phys. Lett.*, *105*, 25: p. 251104, dec 2014.

[75] Balandin, A.A.; Ghosh, S.; Bao, W.; Calizo, I.; Teweldebrhan, D.; Miao, F.; and Lau, C.N. "Superior Thermal Conductivity of Single-Layer Graphene." *Nano Lett.*, *8*, 3: pp. 902–907, mar 2008.

[76] Gan, S.; Cheng, C.; Zhan, Y.; Huang, B.; Gan, X.; Li, S.; Lin, S.; Li, X.; Zhao, J.; Chen, H.; and Bao, Q. "A highly efficient thermo-optic microring modulator assisted by graphene." *Nanoscale*, *7*, 47: pp. 20249–20255, 2015.

[77] Lin, C.; Grassi, R.; Low, T.; and Helmy, A.S. "Multilayer Black Phosphorus as a Versatile Mid-Infrared Electro-optic Material." *Nano Lett.*, *16*, 3: pp. 1683–9, mar 2016.

[78] Whitney, W.S.; Sherrott, M.C.; Jariwala, D.; Lin, W.H.; Bechtel, H.A.; Rossman, G.R.; and Atwater, H.A. "Field Effect Optoelectronic Modulation of Quantum-Confined Carriers in Black Phosphorus.", aug 2016.

[79] Freitag, M.; Low, T.; Xia, F.; and Avouris, P. "Photoconductivity of biased graphene." *Nat. Photonics*, *7*, 1: pp. 53–59, dec 2012.

[80] Kittel, C. "Introduction to solid state physics." *Solid State Phys.*, p. 703, 2005.

[81] Song, J.C.W.; Rudner, M.S.; Marcus, C.M.; and Levitov, L.S. "Hot carrier transport and photocurrent response in graphene." *Nano Lett.*, *11*, 11: pp. 4688–4692, 2011.

[82] Cutler, M. and Mott, N.F. "Observation of anderson localization in an electron gas." *Phys. Rev.*, *181*, 3: pp. 1336–1340, 1969.

[83] Xu, X.; Gabor, N.M.; Alden, J.S.; van der Zande, A.M.; and McEuen, P.L. "Photo-Thermoelectric Effect at a Graphene Interface Junction." *Nano Lett.*, *10*, 2: pp. 562–566, feb 2010.

[84] Tielrooij, K.J.; Song, J.C.W.; Jensen, S.A.; Centeno, A.; Pesquera, A.; Zurutuza Elorza, A.; Bonn, M.; Levitov, L.S.; and Koppens, F.H.L. "Photoexcitation cascade and multiple hot-carrier generation in graphene." *Nat. Phys.*, *9*, 4: pp. 248–252, feb 2013.

[85] Gabor, N.M.; Song, J.C.W.; Ma, Q.; Nair, N.L.; Taychatanapat, T.; Watanabe, K.; Taniguchi, T.; Levitov, L.S.; and Jarillo-Herrero, P. "Hot carrier-assisted intrinsic photoresponse in graphene." *Science*, *334*, 6056: pp. 648–52, nov 2011.

[86] Lin, H.C.; Ye, P.D.; and Wilk, G.D. "Leakage current and breakdown electric-field studies on ultrathin atomic-layer-deposited Al2O3 on GaAs." *Appl. Phys. Lett.*, *87*, 18: pp. 1–3, 2005.

[87] Fang, T.; Konar, A.; Xing, H.; and Jena, D. "Carrier statistics and quantum capacitance of graphene sheets and ribbons." *Appl. Phys. Lett.*, *91*, 9, 2007.

[88] Gusynin, V.P.; Sharapov, S.G.; and Carbotte, J.P. "On the universal ac optical background in graphene." *New J. Phys.*, *11*, 9: p. 095013, sep 2009.

[89] Reed, G.T.; Mashanovich, G.; Gardes, F.Y.; and Thomson, D.J. "Silicon optical modulators." *Nat. Photonics*, *4*, 8: pp. 518–526, jul 2010.

[90] Koester, S.J.; Schaub, J.D.; Dehlinger, G.; and Chu, J.O. "Germanium-on-SOI Infrared Detectors for Integrated Photonic Applications." *IEEE J. Sel. Top. Quantum Electron.*, *12*, 6: pp. 1489–1502, nov 2006.

[91] Assefa, S.; Xia, F.; and Vlasov, Y.A. “Reinventing germanium avalanche photodetector for nanophotonic on-chip optical interconnects.” *Nature*, *464*, 7285: pp. 80–4, mar 2010.

[92] Soref, R. and Bennett, B. “Electrooptical effects in silicon.” *IEEE J. Quantum Electron.*, *23*, 1: pp. 123–129, jan 1987.

[93] Xu, Q.; Schmidt, B.; Pradhan, S.; and Lipson, M. “Micrometre-scale silicon electro-optic modulator.” *Nature*, *435*, 7040: pp. 325–7, may 2005.

[94] Bonaccorso, F.; Sun, Z.; Hasan, T.; and Ferrari, A.C. “Graphene photonics and optoelectronics.” *Nat. Photonics*, *4*, 9: pp. 611–622, sep 2010.

[95] Avouris, P. “Graphene: Electronic and Photonic Properties and Devices.” *Nano Lett.*, *10*, 11: pp. 4285–4294, nov 2010.

[96] Kim, K.; Choi, J.Y.; Kim, T.; Cho, S.H.; and Chung, H.J. “A role for graphene in silicon-based semiconductor devices.” *Nature*, *479*, 7373: pp. 338–44, nov 2011.

[97] Bao, Q.; Zhang, H.; Wang, B.; Ni, Z.; Lim, C.H.Y.X.; Wang, Y.; Tang, D.Y.; and Loh, K.P. “Broadband graphene polarizer.” *Nat. Photonics*, *5*, 7: pp. 411–415, may 2011.

[98] Bao, Q.; Zhang, H.; Wang, Y.; Ni, Z.; Yan, Y.; Shen, Z.X.; Loh, K.P.; and Tang, D.Y. “Atomic-Layer Graphene as a Saturable Absorber for Ultrafast Pulsed Lasers.” *Adv. Funct. Mater.*, *19*, 19: pp. 3077–3083, oct 2009.

[99] Sun, Z.; Hasan, T.; Torrisi, F.; Popa, D.; Privitera, G.; Wang, F.; Bonaccorso, F.; Basko, D.M.; and Ferrari, A.C. “Graphene mode-locked ultrafast laser.” *ACS Nano*, *4*, 2: pp. 803–10, feb 2010.

[100] Giovannetti, G.; Khomyakov, P.A.; Brocks, G.; Karpan, V.M.; van den Brink, J.; and Kelly, P.J. "Doping Graphene with Metal Contacts." *Phys. Rev. Lett.*, *101*, 2: p. 026803, jul 2008.

[101] Lee, E.J.H.; Balasubramanian, K.; Weitz, R.T.; Burghard, M.; and Kern, K. "Contact and edge effects in graphene devices." *Nat. Nanotechnol.*, *3*, 8: pp. 486–90, aug 2008.

[102] Xia, F.; Mueller, T.; Golizadeh-Mojarad, R.; Freitag, M.; Lin, Y.m.; Tsang, J.; Perebeinos, V.; and Avouris, P. "Photocurrent imaging and efficient photon detection in a graphene transistor." *Nano Lett.*, *9*, 3: pp. 1039–44, mar 2009.

[103] Xia, F.; Perebeinos, V.; Lin, Y.m.; Wu, Y.; and Avouris, P. "The origins and limits of metal-graphene junction resistance." *Nat. Nanotechnol.*, *6*, 3: pp. 179–84, mar 2011.

[104] Li, Z.Q.; Henriksen, E.A.; Jiang, Z.; Hao, Z.; Martin, M.C.; Kim, P.; Stormer, H.L.; and Basov, D.N. "Dirac charge dynamics in graphene by infrared spectroscopy." *Nat. Phys.*, *4*, 7: pp. 532–535, jun 2008.

[105] Scharf, B.; Perebeinos, V.; Fabian, J.; and Avouris, P. "Effects of optical and surface polar phonons on the optical conductivity of doped graphene." *Phys. Rev. B*, *87*, 3: p. 035414, jan 2013.

[106] Yao, X. and Maleki, L. "Optoelectronic oscillator for photonic systems." *IEEE J. Quantum Electron.*, *32*, 7: pp. 1141–1149, jul 1996.

[107] Wang, Q.H.; Kalantar-Zadeh, K.; Kis, A.; Coleman, J.N.; and Strano, M.S. "Electronics and optoelectronics of two-dimensional transition metal dichalcogenides." *Nat. Nanotechnol.*, *7*, 11: pp. 699–712, nov 2012.

[108] Mak, K.F.; Lee, C.; Hone, J.; Shan, J.; and Heinz, T.F. "Atomically Thin MoS2: A New Direct-Gap Semiconductor." *Phys. Rev. Lett.*, *105*, 13: p. 136805, sep 2010.

[109] Ellis, J.K.; Lucero, M.J.; and Scuseria, G.E. "The indirect to direct band gap transition in multilayered MoS2 as predicted by screened hybrid density functional theory." *Appl. Phys. Lett.*, *99*, 26: p. 261908, 2011.

[110] Lopez-Sanchez, O.; Lembke, D.; Kayci, M.; Radenovic, A.; and Kis, A. "Ultrasensitive photodetectors based on monolayer MoS2." *Nat. Nanotechnol.*, *8*, 7: pp. 497–501, jun 2013.

[111] Liu, H.; Neal, A.T.; Zhu, Z.; Luo, Z.; Xu, X.; Tománek, D.; and Ye, P.D. "Phosphorene: An Unexplored 2D Semiconductor with a High Hole Mobility." *ACS Nano*, *8*, 4: pp. 4033–4041, apr 2014.

[112] Takao, Y.; Asahina, H.; and Morita, A. "Electronic Structure of Black Phosphorus in Tight Binding Approach." *J. Phys. Soc. Japan*, *105*, 1-3: pp. 3362–3369, may 1981.

[113] Wang, H.; Wang, X.; Xia, F.; Wang, L.; Jiang, H.; Xia, Q.; Chin, M.L.; Dubey, M.; and Han, S.j. "Black Phosphorus Radio-Frequency Transistors." *Nano Lett.*, *14*, 11: pp. 6424–6429, nov 2014.

[114] Li, H.; Anugrah, Y.; Koester, S.J.; and Li, M. "Optical absorption in graphene integrated on silicon waveguides." *Appl. Phys. Lett.*, *101*, 11: p. 111110, sep 2012.

[115] Gan, X.; Gao, Y.; Fai Mak, K.; Yao, X.; Shiue, R.J.; van der Zande, A.; Trusheim, M.E.; Hatami, F.; Heinz, T.F.; Hone, J.; and Englund, D. "Controlling the spontaneous emission rate of monolayer MoS2 in a photonic crystal nanocavity." *Appl. Phys. Lett.*, *103*, 18: p. 181119, 2013.

[116] Wu, S.; Buckley, S.; Jones, A.M.; Ross, J.S.; Ghimire, N.J.; Yan, J.; Mandrus, D.G.; Yao, W.; Hatami, F.; Vučković, J.; Majumdar, A.; and Xu, X. "Control of two-dimensional excitonic light emission via photonic crystal." *2D Mater.*, *1*, 1: p. 011001, apr 2014.

[117] Han, L.; Neal, A.T.; Mengwei, S.; Yuchen, D.; and Ye, P.D. "The Effect of Dielectric Capping on Few-Layer Phosphorene Transistors: Tuning the Schottky Barrier Heights." *IEEE Electron Device Lett.*, *35*, 7: pp. 795–797, jul 2014.

[118] Asahina, H. and Morita, A. "Band structure and optical properties of black phosphorus." *J. Phys. C Solid State Phys.*, *17*, 11: p. 1839, 1984.

[119] Feng, D.; Liao, S.; Dong, P.; Feng, N.N.; Liang, H.; Zheng, D.; Kung, C.C.; Fong, J.; Shafiiha, R.; Cunningham, J.; Krishnamoorthy, A.V.; and Asghari, M. "High-speed Ge photodetector monolithically integrated with large cross-section silicon-on-insulator waveguide." *Appl. Phys. Lett.*, *95*, 26: p. 261105, 2009.

[120] Hong, T.; Chamlagain, B.; Lin, W.; Chuang, H.J.; Pan, M.; Zhou, Z.; and Xu, Y.Q. "Polarized photocurrent response in black phosphorus field-effect transistors." *Nanoscale*, *6*, 15: p. 8978, jun 2014.

[121] Chi On Chui; Okyay, A.; and Saraswat, K. "Effective dark current suppression with asymmetric MSM photodetectors in Group IV semiconductors." *IEEE Photonics Technol. Lett.*, *15*, 11: pp. 1585–1587, nov 2003.

[122] Slack, G.A. "Thermal Conductivity of Elements with Complex Lattices: B, P, S." *Phys. Rev.*, *139*, 2A: pp. A507–A515, jul 1965.

[123] Pernice, W.H.P.; Li, M.; and Tang, H.X. "Gigahertz photothermal effect in silicon waveguides." *Appl. Phys. Lett.*, *93*, 21: p. 213106, 2008.

[124] Deng, Y.; Luo, Z.; Conrad, N.J.; Liu, H.; Gong, Y.; Najmaei, S.; Ajayan, P.M.; Lou, J.; Xu, X.; and Ye, P.D. "Black PhosphorusMonolayer MoS 2 van der Waals Heterojunction pn Diode." *ACS Nano*, *8*, 8: pp. 8292–8299, aug 2014.

[125] Wang, X.; Jones, A.M.; Seyler, K.L.; Tran, V.; Jia, Y.; Zhao, H.; Wang, H.; Yang, L.; Xu, X.; and Xia, F. "Highly anisotropic and robust excitons in monolayer black phosphorus." *Nat. Nanotechnol.*, *10*, 6: pp. 517–521, apr 2015.

[126] Britnell, L.; Ribeiro, R.M.; Eckmann, A.; Jalil, R.; Belle, B.D.; Mishchenko, A.; Kim, Y.J.; Gorbachev, R.V.; Georgiou, T.; Morozov, S.V.; Grigorenko, A.N.; Geim, A.K.; Casiraghi, C.; Neto, A.H.C.; and Novoselov, K.S. "Strong Light-Matter Interactions in Heterostructures of Atomically Thin Films." *Science (80-.).*, *340*, 6138: pp. 1311–1314, jun 2013.

[127] Geim, A.K. and Grigorieva, I.V. "Van der Waals heterostructures." *Nature*, *499*, 7459: pp. 419–425, jul 2013.

[128] Levendorf, M.P.; Kim, C.J.; Brown, L.; Huang, P.Y.; Havener, R.W.; Muller, D.A.; and Park, J. "Graphene and boron nitride lateral heterostructures for atomically thin circuitry." *Nature*, *488*, 7413: pp. 627–632, aug 2012.

[129] Qiao, J.; Kong, X.; Hu, Z.X.; Yang, F.; and Ji, W. "High-mobility transport anisotropy and linear dichroism in few-layer black phosphorus." *Nat. Commun.*, *5*: p. 4475, jan 2014.

[130] Xia, F.; Wang, H.; Xiao, D.; Dubey, M.; and Ramasubramaniam, A. "Two-dimensional material nanophotonics." *Nat. Photonics*, *8*, 12: pp. 899–907, nov 2014.

[131] Tran, V.; Soklaski, R.; Liang, Y.; and Yang, L. "Layer-controlled band gap and anisotropic excitons in few-layer black phosphorus." *Phys. Rev. B*, *89*, 23: p. 235319, jun 2014.

[132] Kim, J.; Baik, S.S.; Ryu, S.H.; Sohn, Y.; Park, S.; Park, B.G.; Denlinger, J.; Yi, Y.; Choi, H.J.; and Kim, K.S. "Observation of tunable band gap and anisotropic Dirac semimetal state in black phosphorus." *Science*, *349*, 6249: pp. 723–6, aug 2015.

[133] Graham, M.W.; Shi, S.F.; Ralph, D.C.; Park, J.; and McEuen, P.L. "Photocurrent measurements of supercollision cooling in graphene." *Nat. Phys.*, *9*, 2: pp. 103–108, 2013.

[134] Yin, X.; Ye, Z.; Chenet, D.A.; Ye, Y.; O'Brien, K.; Hone, J.C.; and Zhang, X. "Edge nonlinear optics on a MoS2 atomic monolayer." *Science*, *344*, 6183: pp. 488–90, may 2014.

[135] Li, Y.; Rao, Y.; Mak, K.F.; You, Y.; Wang, S.; Dean, C.R.; and Heinz, T.F. "Probing symmetry properties of few-layer MoS2 and h-BN by optical second-harmonic generation." *Nano Lett.*, *13*, 7: pp. 3329–33, jul 2013.

[136] Malard, L.M.; Alencar, T.V.; Barboza, A.P.M.; Mak, K.F.; and de Paula, A.M. "Observation of intense second harmonic generation from MoS2 atomic crystals." *Phys. Rev. B*, *87*, 20: p. 201401, may 2013.

[137] Wang, G.; Marie, X.; Gerber, I.; Amand, T.; Lagarde, D.; Bouet, L.; Vidal, M.; Balocchi, A.; and Urbaszek, B. "Giant enhancement of the optical second-harmonic emission of WSe(2) monolayers by laser excitation at exciton resonances." *Phys. Rev. Lett.*, *114*, 9: p. 097403, mar 2015.

[138] Seyler, K.L.; Schaibley, J.R.; Gong, P.; Rivera, P.; Jones, A.M.; Wu, S.; Yan, J.; Mandrus, D.G.; Yao, W.; and Xu, X. "Electrical control of second-harmonic generation in a WSe2 monolayer transistor." *Nat. Nanotechnol.*, *10*, 5: pp. 407–11, may 2015.

[139] Hong, S.Y.; Dadap, J.I.; Petrone, N.; Yeh, P.C.; Hone, J.; and Osgood, R.M. "Optical Third-Harmonic Generation in Graphene." *Phys. Rev. X*, *3*, 2: p. 021014, jun 2013.

[140] Kumar, N.; Kumar, J.; Gerstenkorn, C.; Wang, R.; Chiu, H.Y.; Smirl, A.L.; and Zhao, H. "Third harmonic generation in graphene and few-layer graphite films." *Phys. Rev. B*, *87*, 12: p. 121406, mar 2013.

[141] Säynätjoki, A.; Karvonen, L.; Riikonen, J.; Kim, W.; Mehravar, S.; Norwood, R.A.; Peyghambarian, N.; Lipsanen, H.; and Kieu, K. "Rapid large-area multiphoton microscopy for characterization of graphene." *ACS Nano*, *7*, 10: pp. 8441–8446, 2013.

[142] Woodward, R.I.; Murray, R.T.; Phelan, C.F.; de Oliveira, R.E.P.; Runcorn, T.H.; Kelleher, E.J.R.; Li, S.; de Oliveira, E.C.; Fechine, G.J.M.; Eda, G.; and de Matos, C.J.S. "Characterization of the second- and third-order nonlinear optical susceptibilities of monolayer MoS2 using multiphoton microscopy.", jun 2016.

[143] Wang, R.; Chien, H.C.; Kumar, J.; Kumar, N.; Chiu, H.Y.; and Zhao, H. "Third-harmonic generation in ultrathin films of MoS2." *ACS Appl. Mater. Interfaces*, *6*, 1: pp. 314–8, jan 2014.

[144] Säynätjoki, A.; Karvonen, L.; Rostami, H.; Autere, A.; Mehravar, S.; Lombardo, A.; Norwood, R.A.; Hasan, T.; Peyghambarian, N.; Lipsanen, H.; Kieu, K.; Ferrari, A.C.; Polini, M.; and Sun, Z. "Ultra-strong nonlinear optical processes and trigonal warping in MoS2 layers.", aug 2016.

[145] Lu, S.B.; Miao, L.L.; Guo, Z.N.; Qi, X.; Zhao, C.J.; Zhang, H.; Wen, S.C.; Tang, D.Y.; and Fan, D.Y. "Broadband nonlinear optical response in multi-layer black phosphorus: an emerging infrared and mid-infrared optical material." *Opt. Express*, *23*, 9: pp. 11183–94, may 2015.

[146] Zhang, F.; Wu, Z.; Wang, Z.; Wang, D.; Wang, S.; and Xu, X. "Strong optical limiting behavior discovered in black phosphorus." *RSC Adv.*, *6*, 24: pp. 20027–20033, 2016.

[147] Wang, Y.; Huang, G.; Mu, H.; Lin, S.; Chen, J.; Xiao, S.; Bao, Q.; and He, J. "Ultrafast recovery time and broadband saturable absorption properties of black phosphorus suspension." *Appl. Phys. Lett.*, *107*, 9: p. 091905, aug 2015.

[148] Luo, Z.C.; Liu, M.; Guo, Z.N.; Jiang, X.F.; Luo, A.P.; Zhao, C.J.; Yu, X.F.; Xu, W.C.; and Zhang, H. "Microfiber-based few-layer black phosphorus saturable absorber for ultra-fast fiber laser." *Opt. Express*, *23*, 15: p. 20030, jul 2015.

[149] Sotor, J.; Sobon, G.; Macherzynski, W.; Paletko, P.; and Abramski, K.M. "Black phosphorus saturable absorber for ultrashort pulse generation." *Appl. Phys. Lett.*, *107*, 5: p. 051108, aug 2015.

[150] Mu, H.; Lin, S.; Wang, Z.; Xiao, S.; Li, P.; Chen, Y.; Zhang, H.; Bao, H.; Lau, S.P.; Pan, C.; Fan, D.; and Bao, Q. "Black Phosphorus-Polymer Composites for Pulsed Lasers." *Adv. Opt. Mater.*, *3*, 10: pp. 1447–1453, oct 2015.

[151] Chen, Y.; Jiang, G.; Chen, S.; Guo, Z.; Yu, X.; Zhao, C.; Zhang, H.; Bao, Q.; Wen, S.; Tang, D.; and Fan, D. "Mechanically exfoliated black phosphorus as a new saturable absorber for both Q-switching and Mode-locking laser operation." *Opt. Express*, *23*, 10: pp. 12823–33, may 2015.

[152] Lu, D.; Pan, Z.; Zhang, R.; Xu, T.; Yang, R.; Yang, B.; Liu, Z.; Yu, H.; Zhang, H.; and Wang, J. "Passively Q-switched ytterbium-doped ScBO 3 laser with black phosphorus saturable absorber." *Opt. Eng.*, *55*, 8: p. 081312, feb 2016.

[153] Boyd, R.W. *Nonlinear Optics, Third Edition.* Academic Press, Burlington, Mass., 3rd ed., 2008.

[154] Mao, N.; Tang, J.; Xie, L.; Wu, J.; Han, B.; Lin, J.; Deng, S.; Ji, W.; Xu, H.; Liu, K.; Tong, L.; and Zhang, J. "Optical Anisotropy of Black Phosphorus in the Visible Regime." *J. Am. Chem. Soc.*, *138*, 1: pp. 300–5, jan 2016.

[155] Brown, A. and Rundqvist, S. "Refinement of the crystal structure of black phosphorus." *Acta Crystallogr.*, *19*, 4: pp. 684–685, oct 1965.

[156] Yang, X.L. and Xie, S.W. "Expression of third-order effective nonlinear susceptibility for third-harmonic generation in crystals." *Appl. Opt.*, *34*, 27: pp. 6130–5, sep 1995.

[157] Quereda, J.; San-Jose, P.; Parente, V.; Vaquero-Garzon, L.; Molina-Mendoza, A.J.; Agraït, N.; Rubio-Bollinger, G.; Guinea, F.; Roldán, R.; and Castellanos-Gomez, A. "Strong Modulation of Optical Properties in Black Phosphorus through Strain-Engineered Rippling." *Nano Lett.*, *16*, 5: pp. 2931–2937, may 2016.

[158] Meshulach, D.; Barad, Y.; and Silberberg, Y. "Measurement of ultrashort optical pulses by third-harmonic generation." *J. Opt. Soc. Am. B*, *14*, 8: p. 2122, aug 1997.

[159] Karvonen, L.; Säynätjoki, A.; Mehravar, S.; Rodriguez, R.D.; Hartmann, S.; Zahn, D.R.T.; Honkanen, S.; Norwood, R.A.; Peyghambarian, N.; Kieu, K.; Lipsanen, H.; and Riikonen, J. "Investigation of Second- and Third-Harmonic Generation in Few-Layer Gallium Selenide by Multiphoton Microscopy." *Sci. Rep.*, *5*: p. 10334, may 2015.

[160] Savostianova, N.A. and Mikhailov, S.A. "Giant enhancement of the third harmonic in graphene integrated in a layered structure." *Appl. Phys. Lett.*, *107*, 18, 2015.

[161] Hendry, E.; Hale, P.J.; Moger, J.; Savchenko, A.K.; and Mikhailov, S.A. "Coherent nonlinear optical response of graphene." *Phys. Rev. Lett.*, *105*, 9, 2010.

[162] Cheng, J.L.; Vermeulen, N.; and Sipe, J.E. "Third order optical nonlinearity of graphene." *New J. Phys.*, *16*, 2014.

[163] Wu, S.; Buckley, S.; Schaibley, J.R.; Feng, L.; Yan, J.; Mandrus, D.G.; Hatami, F.; Yao, W.; Vuckovic, J.; Majumdar, A.; and Xu, X. "Monolayer semiconductor nanocavity lasers with ultralow thresholds." *Nature*, *520*, 7545: pp. 1–8, mar 2015.

[164] Ye, Y.; Wong, Z.J.; Lu, X.; Ni, X.; Zhu, H.; Chen, X.; Wang, Y.; and Zhang, X. "Monolayer excitonic laser." *Nat. Photonics*, *9*, October: pp. 733–737, oct 2015.

[165] Majumdar, A.; Dodson, C.M.; Fryett, T.K.; Zhan, A.; Buckley, S.; and Gerace, D. "Hybrid 2D Material Nanophotonics: A Scalable Platform for Low-Power Nonlinear and Quantum Optics." *ACS Photonics*, *2*, 8: pp. 1160–1166, aug 2015.

[166] He, Y.M.; Clark, G.; Schaibley, J.R.; He, Y.; Chen, M.C.; Wei, Y.J.; Ding, X.; Zhang, Q.; Yao, W.; Xu, X.; Lu, C.Y.; and Pan, J.W. "Single quantum emitters in monolayer semiconductors." *Nat. Nanotechnol.*, *10*, 6: pp. 497–502, may 2015.

[167] Tonndorf, P.; Schmidt, R.; Schneider, R.; Kern, J.; Buscema, M.; Steele, G.A.; Castellanos-Gomez, A.; van der Zant, H.S.J.; Michaelis de Vasconcellos, S.; and Bratschitsch, R. "Single-photon emission from localized excitons in an atomically thin semiconductor." *Optica*, *2*, 4: p. 347, apr 2015.

[168] Tran, T.T.; Bray, K.; Ford, M.J.; Toth, M.; and Aharonovich, I. "Quantum emission from hexagonal boron nitride monolayers." *Nat. Nanotechnol.*, *11*, 1: pp. 37–41, oct 2015.

[169] Clark, G.; Schaibley, J.R.; Ross, J.; Taniguchi, T.; Watanabe, K.; Hendrickson, J.R.; Mou, S.; Yao, W.; and Xu, X. "Single Defect Light-Emitting Diode in a van der Waals Heterostructure." *Nano Lett.*, *16*, 6: pp. 3944–3948, jun 2016.

[170] Schwarz, S.; Kozikov, A.; Withers, F.; Maguire, J.K.; Foster, A.P.; Dufferwiel, S.; and Hague, L. "Electrically pumped single-defect light emitters in WSe2." *arXiv*, p. 1605.01921, may 2016.

[171] Rivera, P.; Schaibley, J.R.; Jones, A.M.; Ross, J.S.; Wu, S.; Aivazian, G.; Klement, P.; Seyler, K.; Clark, G.; Ghimire, N.J.; Yan, J.; Mandrus, D.G.; Yao, W.; and Xu, X. "Observation of long-lived interlayer excitons in monolayer MoSe2WSe2 heterostructures." *Nat. Commun.*, *6*: p. 6242, feb 2015.

[172] Wang, X.; Jones, A.M.; Seyler, K.L.; Tran, V.; Jia, Y.; Zhao, H.; Wang, H.; Yang, L.; Xu, X.; and Xia, F. "Highly anisotropic and robust excitons in monolayer black phosphorus." *Nat. Nanotechnol.*, *10*, 6: pp. 517–21, jun 2015.

[173] Jackson, J.D. *Classical Electrodynamics.* John Wiley & Sons, Inc., Hoboken, NJ, third ed., 1999.

Appendix A

Fabrication Techniques

A.1 Waveguide planarization

Initially, our group was using FOX 25, a spin-on dielectric from Dow Corning, to planarize waveguides for graphene transfer. This technique involved spinning and annealing 3 layers of FOX 25 to create a relatively smooth oxide cladding layer 1 µm above the waveguides and then using a diluted BOE etch to thin the oxide to tens of nm above the waveguide. This process was very difficult to control, time consuming, and usually resulted in devices that were both over- and under-etched on the same chip leaving only a few devices with the desired cladding layer thickness. Since the remaining oxide thickness across the surface of the 1 cm × 1 cm sample could vary by as much as 100 nm, a new method was developed to replace the FOX planarization technique.

The new process requires the photonics layer to be written using a resist that has good etch resistance, but is easily removed such as ma-N or ZEP. In figure A.1a, the photonics layer is written using ma-N 2403 spun at 2000 RPM. After etching (figure A.1b), the resist is not removed, but used as the lift-off pattern

for the dielectric layer. Oxide is evaporated using an electron beam evaporator to a thickness slightly greater than the height of the waveguides. After the oxide is evaporated on the resist-covered waveguides (figure A.1c), the sample is left to soak in acetone overnight to soften the resist. Physical abrasion using a cotton swab and acetone is used to remove the remaining resist/oxide layer and the sample is further cleaned using an ultrasonic bath (figure A.1d). The sample is then annealed in an oxygen rich environment using Rapid Thermal Annealing (RTA). The oxide layer shrinks in thickness (by about 17%) during the annealing process which is accounted for during the initial deposition. After annealing (figure A.1e), an optional oxide layer can be deposited using ALD (figure A.1f).

This new method for planarizing waveguides allows very precise control over the thickness of the oxide cladding and is very uniform over the entire area of the sample. Table A.1 provides the recipe used to anneal both FOX 25 and evaporated oxide using RTA.

Step	Command	Time (sec)	Temp (°C)	Flow	Gas
1	Idle	20	0	30	N_2
2	Idle	10	0	15	N_2
3	Ramp	20	500	5	O_2
4	Hold	10	500	5	O_2
5	Ramp	13	1150	5	O_2
6	Hold	60	1150	5	O_2
7	Ramp	30	20	5	O_2
8	Idle	10	0	5	O_2
9	Idle	30	0	15	N_2
10	Idle	120	0	30	N_2
11	Stop	0	0	0	0

Table A.1: Recipe used to anneal evaporated oxide and FOX 25 spin-on dielectric

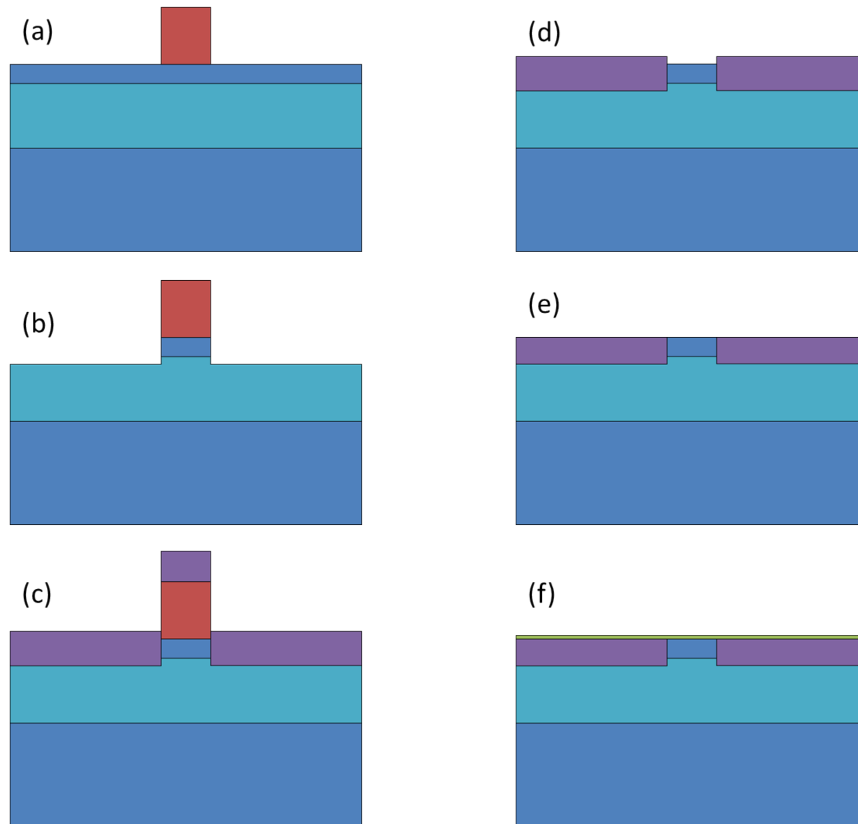

Figure A.1: Process flow for planarizing waveguides with oxide. The waveguides are defined with ebeam lithography (a) and etched using the Bosch method (b). An oxide planarizing layer is evaporated (c) and removed from the waveguides with acetone and physical abrasion (d). The planarizing layer is then annealed in an oxygen rich environment using an RTA (e). An optional oxide spacing layer can be deposited using ALD (f).

A.2 CVD graphene transfer with PMMA

Another fabrication advance involved improving the graphene transfer recipe. It was found that the initial quality of the graphene film was crucial to the quality of the transferred film. PMMA residue on the surface of the transferred graphene is caused by etchant solution penetrating cracks in the graphene and hardening the support layer (PMMA in our case) on the other side. Therefore, it is important to have a continuous sheet of graphene initially. The recipe for transferring graphene can be summarized as follows:

1. Carefully cut a flat piece of graphene/copper with razor blade.
2. Spin-coat PMMA C4 at 4000 RPM for 1 minute.
3. Heat the sample at 180 °C for 5 minutes.
4. Clean the back side of the sample using the cotton swab (with or without acetone).
5. Use STS etcher and etch the graphene on the back side at 100 W and 20 SCCM of O_2 for 15 seconds.
6. Etch the copper with PMMA/graphene in ammonium persulfate for 1 to 1.5 hours.
7. Float the PMMA/graphene membrane in DI-water for 15 minutes.
8. Scoop onto the target substrate (use a needle to help align the membrane with the target substrate).
9. Dry gently with N_2 gun, carefully removing the water trapped between PMMA/graphene and substrate (blow from center toward edges).

10. Bake at 80 °C for 2 minutes, 95 °C for 3 minutes, then 180 °C for 20 minutes. This reflows the PMMA which relaxes the graphene (improving adhesion) and removes wrinkles and remaining trapped water.

11. Cool down and soak in acetone overnight.

Using this recipe and handling the graphene/copper foil very carefully, we were able to achieve high quality transfers. Figure A.2 shows a continuous and clean graphene sheet transferred onto some test structures.

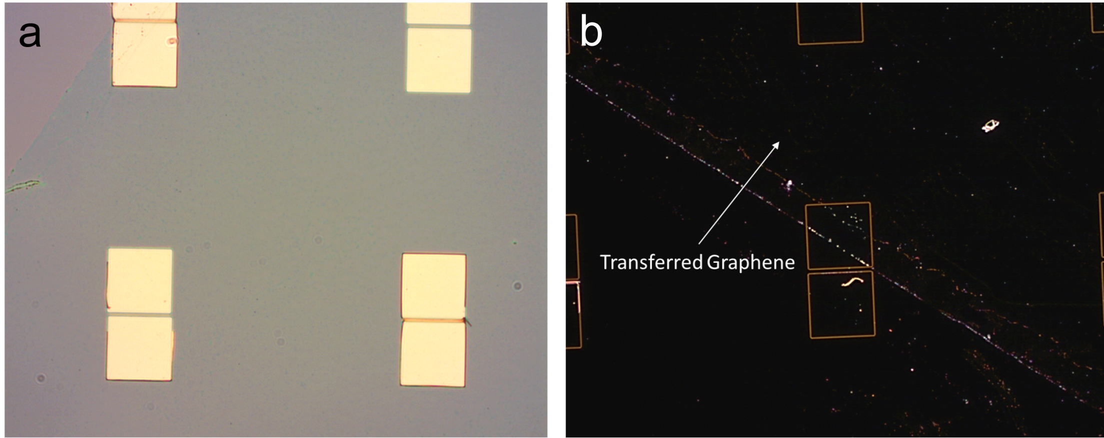

Figure A.2: (a) Microscope image of transferred graphene monolayer sheet. (b) Dark field image of transferred graphene showing minimal residue.

A.3 Aligned exfoliation of 2D materials

In this section, we will describe exfoliation using Scotch tape and two methods for aligned transfer to waveguides or other structures.

A.3.1 Scotch tape exfoliation

1. Break off a piece of 3M Scotch or Nitto tape (roughly 4 inches) and fold a small area over at both ends for easier handling.

2. Place a flake of graphene (or other 2D material) on adhesive side. We have found that the best exfoliation starts with the shiniest, largest, and most uniform crystals. The better the crystal, the larger and thinner flakes achievable.

3. Fold unused region of tape onto graphene flakes and pull apart to cleave crystal planes.

4. Repeat this process being careful not to touch regions of tape together that already have graphene on them. Doing so will reduce the size of graphene flakes and contaminate the graphene. You want the graphene to be as dense on the tape as possible to make finding useful pieces easier.

5. After tape is covered with graphene, another piece of tape can be laid across the original piece and removed for one more exfoliation. This step can be repeated many times to make extra transfer tapes.

6. Once tape is ready, lay it across an the target substrate and gently rub the tape to facilitate transfer. Remove all bubbles from the tape and make

sure to rub over the entire area at least once. Pressing too hard will leave unnecessary tape residue, so be careful!

7. For hard substrates (such as SiO_2 (290–300 nm)/Si or PMMA/PVA), slowly remove tape at a fixed angle (need to play around with this parameter) with constant speed. For soft substrates (such as PDMS on glass), remove the tape as quickly as possible to get better coverage. Be careful not to let tape touch the substrate once it is removed. Minimizing residue is key for successful transfers.

8. Search for large monolayers (a large piece might be about 50 μm along one of its lengths) with a microscope and gently scratch the closest edge of the substrate so the piece can be found at a future time. Take pictures at multiple magnifications and document the location of pieces well.

A.3.2 Wet transfer method

The wet transfer method is useful for substrates that have a rough surface and do not have good adhesion between the 2D material and the substrate. Figure A.3 gives an overview of this transfer method.

Sacrificial substrate preparation

1. Thoroughly clean silicon substrate (roughly 2×2 cm) using solvents.

2. Spin coat wafer with poly(vinyl alcohol) (PVA) solution (1.5% by weight in DI water) at 3500 RPM for 1 minute.

3. Bake at 150 °C for 1 minute. Cool before next step.

4. Spin coat wafer with PMMA (950 PMMA C4) at 2750 RPM for 1 minute.

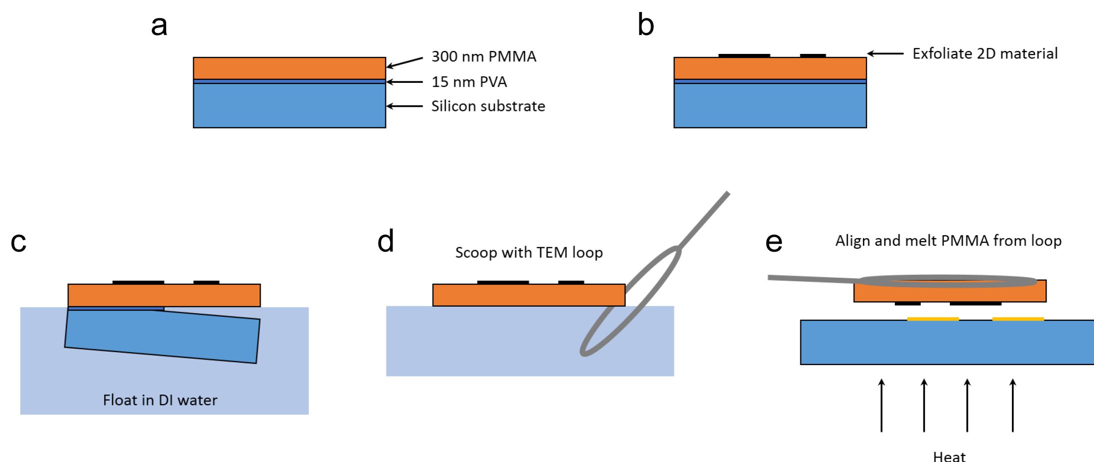

Figure A.3: Overview of wet transfer method. (a) Prepare sacrificial substrate with PVA/PMMA on silicon. (b) Exfoliate desired 2D material. (c) Float in water to dissolve PVA layer and suspend PMMA. (d) Collect PMMA from water with TEM loop. (e) Transfer 2D material onto target substrate using microscope and heat to reflow PMMA.

5. Bake at 150 °C for 5 minutes until normal incident reflection is a deep reddish-purple color. The goal is to make a layer of PMMA that looks very similar to the color of 290–300 nm SiO_2 on silicon so that monolayers of 2D materials show up clearly under a microscope.

Exfoliation and membrane suspension

1. Follow methods outlined previously to prepare tape with 2D material and exfoliate onto silicon/PVA/PMMA substrate.

2. Locate monolayers on the substrate under a microscope and at low magnification, make four small scratches in the PMMA at the edge of the field of view. These scratches will help you locate where the center of your chip should be when you break the wafer into a smaller piece. Multiple monolayers can be transferred from the main substrate as long as they are not

located too close together.

3. Cleave the main substrate into a square chip centered around the four scratches made in the PMMA. The chip should be slightly larger than the size of your TEM loop, but not too large or the PMMA membrane will fold over the loop and make transferring difficult.

4. Make a scratch around all four edges of the PMMA/chip interface so PVA is exposed.

5. Place the chip in DI water. It will float due to the PMMA membrane on top. Gently hold one corner under the surface of the water until the PVA layer begins to dissolve and the PMMA membrane starts to delaminate.

6. Wait for gravity to pull the chip away from the PMMA membrane and let the membrane float in DI water for at least 5 minutes to ensure the PVA layer has fully dissolved.

7. Scoop the PMMA membrane out of the water with the TEM loop. The best practice is to hold the loop vertically throughout the entire process. Move the membrane to the container's glass wall and lift the loop vertically. The membrane should lie flat and tight against the loop. If you are not satisfied with the membrane's position on the loop, insert the loop vertically back into the DI water to release the membrane and try again. "Deluxe perfect loop" from Electron Microscopy Sciences works very well.

8. Baking the scoop to get rid of water, otherwise the PMMA membrane will fold. (20 minutes at 90 °C)

Transferring to target substrate

1. Fix target substrate to block heater using double stick Kapton or carbon tape and use Kapton tape to attach heater to microscope stage.

2. Locate area where you want to transfer the exfoliated sample and center it under the microscope.

3. Put TEM loop on xyz translation stage and locate exfoliated sample. The loop should be at a very slight angle so that the tip will make contact with the substrate before the rest of the loop does.

4. Iteratively align destination position and sample and lower the loop until contact is made with the substrate.

5. Use a needle or sharp tweezers and carefully force the membrane around the sample to make contact to the substrate. This ensures the position of the sample will not change relative to the substrate when the PMMA is melted.

6. Heat the substrate to 160 °C to melt the PMMA membrane. Wait for the membrane to lay flat against the substrate and until all bubbles are gone.

7. Lift loop slightly from substrate, then shift in xy plane to tear the membrane from the loop. Be careful and make sure the PMMA does not rip or lift off near your sample.

8. Remove loop and cool substrate before soaking in N-Methylpyrrolidone (NMP) for 2 hours to remove remaining PMMA membrane. Sometimes an additional anneal under vaccum before removing the PMMA membrane can help remove water and improve adhesion to the substrate.

A.3.3 Dry transfer method

The dry transfer method is useful for flat substrates that have good adhesion with 2D materials and for making van der Waals heterostructures. Figure A.4 gives an overview of this transfer method.

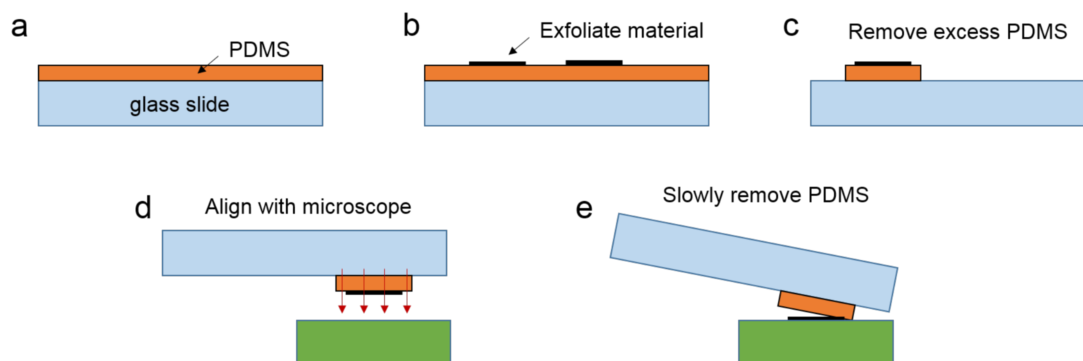

Figure A.4: Overview of dry transfer method. (a) Prepare PDMS on glass slide. (b) Exfoliate 2D material with Scotch tape. (c) Remove excess PDMS with a razor blade. (d) Align and press 2D material in contact with substrate. (e) Slowly remove PDMS to transfer 2D material.

PDMS recipe

1. Using a disposable plastic cup, combine PDMS gel and curing agent 10:1 by weight using a glass rod.

2. Place in desiccator until all bubbles are removed (more than 1 hour).

3. Use a pipette to place a drop of PDMS on clean glass slides and spread over slide using a glass rod. A few mm of PDMS is all that is needed.

4. Set aside and let dry for 48 hours. Bake on hot plate at 60 °C for 10 minutes or longer depending on the desired adhesion.

Exfoliation and transfer

1. Once the PDMS/glass slide is ready, exfoliate using Scotch tape to the PDMS. Peeling the tape from the PDMS at a slow speed will give the best results.

2. Look for desired flakes on PDMS. Remove as much PDMS surrounding the flake as possible using a razor blade. This makes transferring the flake much easier since it is difficult to make contact between the flake and substrate if the surrounding PDMS is in the way.

3. Align and press the flake into contact with the substrate using a microscope.

4. Very slowly release the PDMS stamp and release the flake onto the substrate. This step must be done while viewing through the microscope in order to make sure the transfer is successful. It can take multiple attempts to release the flake from the PDMS. Sometimes increasing the temperature of the substrate can help release the flake from the PDMS.

5. Bake the sample under vaccum at 125 °C over night and rinse with solvents.

6. Repeat this process for subsequent layers if needed.

Appendix B

Experimental Techniques

B.1 Phase Scrambler for Ultrafast Setup

This section describes how to create an inexpensive system for removing the interference artifact from an ultrafast delay line where the pump and probe have the same wavelength and polarization state.

B.1.1 Introduction

When designing an ultrafast pump-probe experimental setup, it is common either to use non-degenerate excitation (i.e. the pump and probe have different wavelengths) or, in the case of a degenerate pump and probe, to use cross polarized beams. This prevents a strong interference artifact near zero delay which will otherwise overwhelm the (usually) small signal under investigation (see figure B.1). There are special circumstances, however, in the case of degenerate pump-probe measurements, where it is undesirable to use cross polarized beams. For example, in our case we are investigating the carrier lifetime of black phosphorus which is

an anisotropic two-dimensional material. Black phosphorus has a much smaller effective mass in the x-direction than in the y-direction ($m^*_{xx} < m^*_{yy}$). This causes a much stronger optical absorption for light polarized along the x-axis of the crystal. Additionally, it has been found that regardless of the incident polarization, the photoluminescence from monolayer black phosphorus is also strongly polarized along the x-axis of the crystal. With this in mind, it is desirable to tune the polarization of the pump and probe independently to probe the lifetimes of x- and y-polarized excitons. This will inevitably lead to the interference artifact we are trying to avoid when the two beams are not polarized orthogonal to one another.

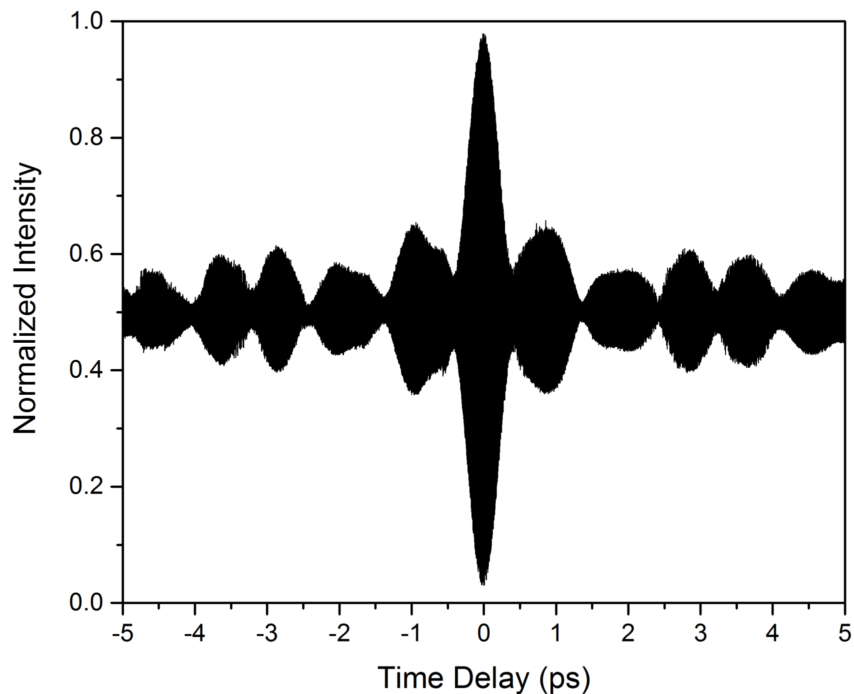

Figure B.1: Measured interference artifact (i.e. autocorrelation) at zero delay in the case of degenerate pump and probe. This interference envelope often overwhelms the desired signal.

While one solution is to simply use a non-degenerate pump-probe scheme, limitations in resources can lead one to improvise. The solution we will be discussing is to place a movable mirror in one of the arms of the interferometer while averaging the detected signal over several cycles of motion.[1] This allows us to remove the cosine term of the interference and resolve the desired signal. In the ideal case, without any additional signal, we would expect the average intensity to be $\langle I \rangle = I_0/2$ regardless of the relative position of the delay line.

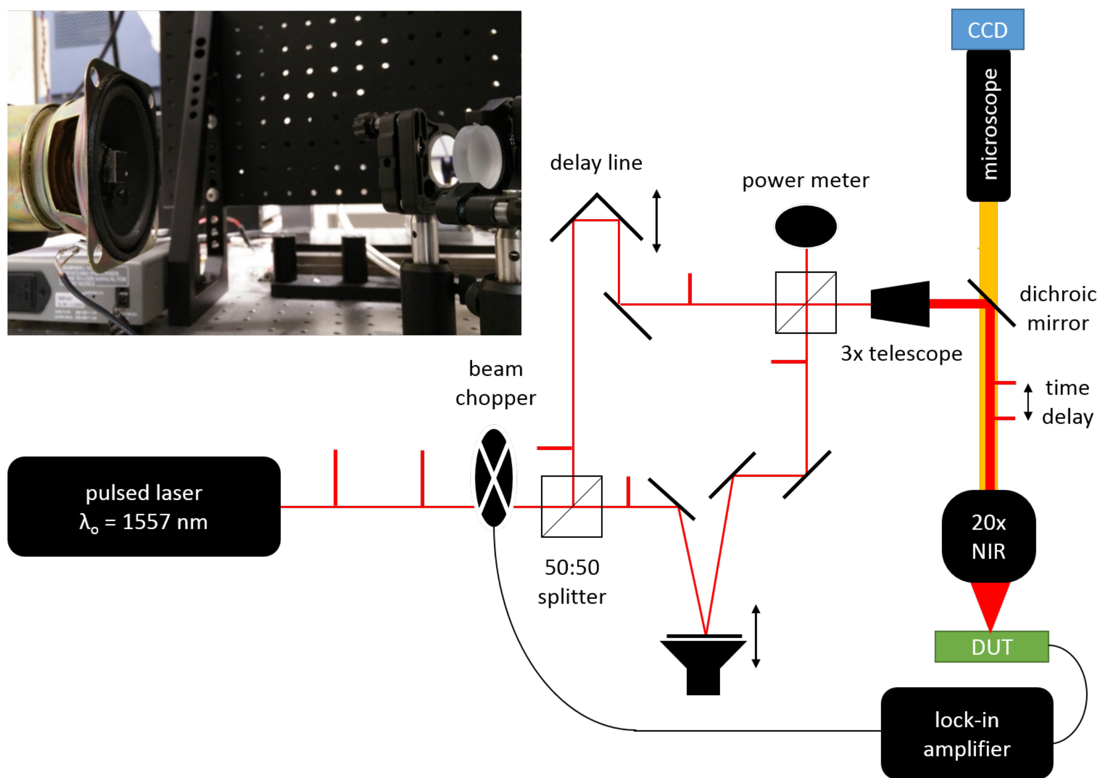

Figure B.2: Diagram of experimental setup with a picture of the mirror mounted on a speaker in the upper left. The delay line is held constant during a single measurement while the speaker is driven with an arbitrary waveform.

[1] Note: In this case, the delay line is stationary during the measurement at each time delay. A better approach, if available, is to simply move the delay line at a constant speed while increasing the integration time on the lock-in amplifier to average out the interference term.

We use a mirror glued to the cone of a computer speaker whose motion is determined by whatever custom waveform is played. This solution is both inexpensive and flexible, allowing a wide range of frequencies to be played from tens of Hz to tens of kHz. The assembled device can be seen in the upper left of figure B.2 which shows a simplified diagram of the experimental setup.

B.1.2 Theory

Now that we have a solution for removing the interference artifact, it is necessary to calculate the optimal waveform for the speaker. Three common waveforms we will consider are sine waves, triangle waves, and Gaussian noise.

Sine Wave Excitation

For the case of a Mach-Zehnder interferometer like we have in figure B.2, the intensity at the second beam splitter can be simply written as $I(x) = I_0 \cos^2(kx + \phi)$ where $k = 2\pi/\lambda$, x is relative position, and ϕ is an additional phase difference between the two arms. If we excite the speaker with a sine wave, we will cause the relative delay to follow a sine wave in time and modulate the intensity (see figure B.3a). The resulting intensity waveform will depend on the amplitude of the speaker's displacement, the frequency at which it is driven, and the relative phase difference (A, ω, and ϕ respectively). Figure B.3b shows one possible intensity waveform after modulating the speaker.

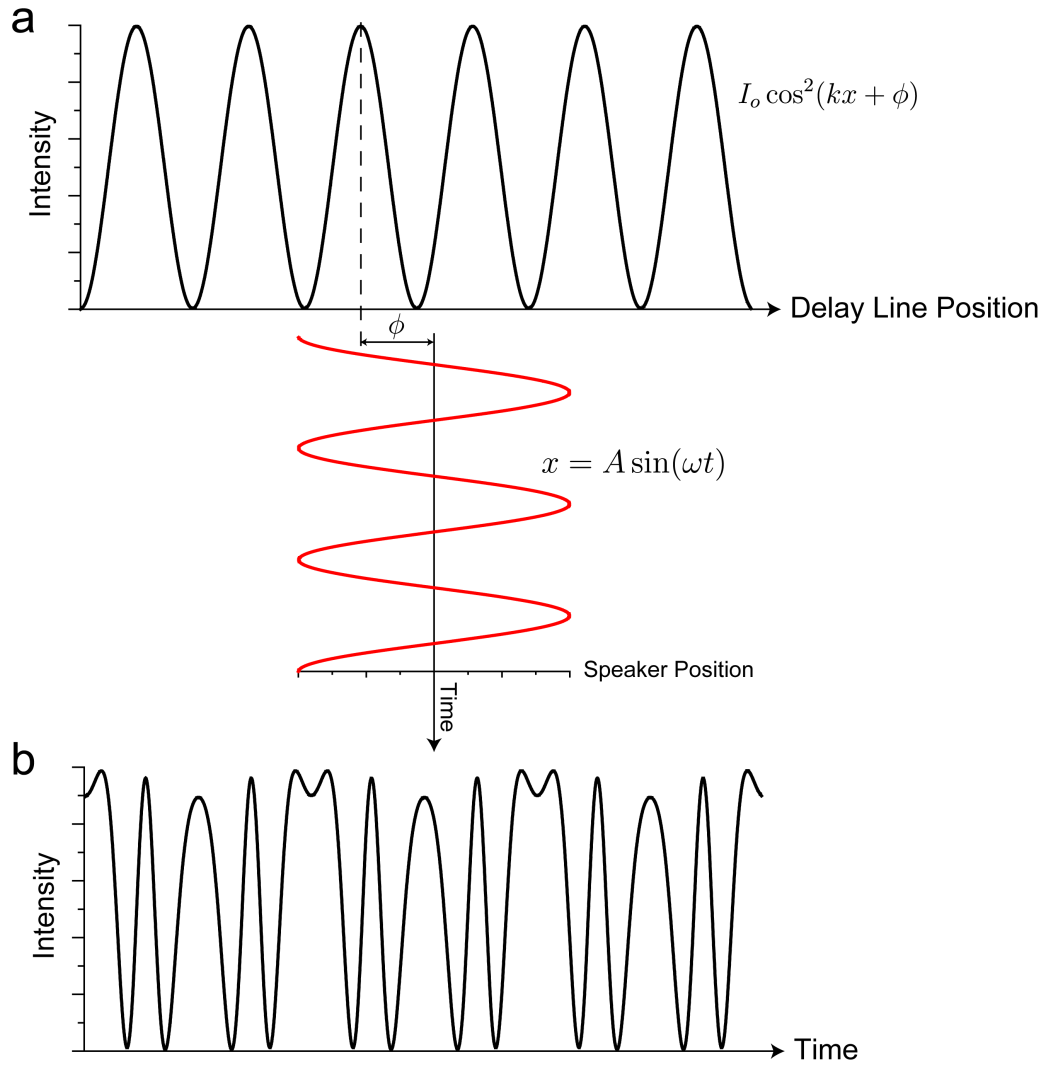

Figure B.3: (a) The black curve shows the intensity at the second beam splitter as a function of delay line position. The speaker modulates the relative path difference in time (red curve). (b) The resulting time-dependent intensity after modulating the speaker with an arbitrary amplitude and frequency.

The time-averaged intensity measured at the device is the following:

$$\langle I \rangle = \frac{1}{T} \int_0^T I_0 \cos^2[kA \sin(\omega t) + \phi] dt \tag{B.1}$$

where T is the integration time of the lock-in amplifier. Using substitution of variables ($x = A \sin(\omega t)$), the integral takes the following form:

$$\langle I \rangle = \int_{-A}^{A} \frac{I_0 \cos^2[kx + \phi]}{\pi \sqrt{A^2 - x^2}} dx \tag{B.2}$$

where we have integrated over one cycle of $x(t)$ (i.e. $T = 2\pi/\omega$). This result is equivalent to multiplying $I(x)$ by the probability density function (PDF) of the speaker waveform and integrating the result. This can be understood intuitively if we consider equation B.2 to be the time-average of $I\left(x(t)\right)$ weighted by the probability that the speaker will be at position x. For a sine wave, the speaker will spend most of the time at the extrema, so the PDF diverges at $-A$ and A. Equation B.2 depends on both A and ϕ (see figure B.2), but we do not have much control over the value of ϕ. To visualize this, we can plot $\langle I(\phi) \rangle$ for a given A. As you can see from figure B.4, only at certain values of ϕ will we get the average value $\langle I \rangle = I_0/2$.

To solve this problem, we can search for a value of A such that equation B.2 will be independent of ϕ. If we integrate equation B.2, we get the following solution:

$$\langle I \rangle = \int_{-A}^{A} \frac{I_0 \cos^2[kx + \phi]}{\pi \sqrt{A^2 - x^2}} dx = \frac{I_0}{2}(1 + J_0[2kA] \cos[2\phi]) \tag{B.3}$$

where J_0 is the Bessel function of the first kind. We can see from equation B.3 that the maximum deviation from $\langle I \rangle = I_0/2$ is when $\cos[2\phi] = \pm 1$. This solution tells us that using a sine wave to excite the speaker is not ideal since $J_0[2kA]$ converges to zero very slowly (see figure B.5). We will next investigate using a triangle wave to excite the speaker.

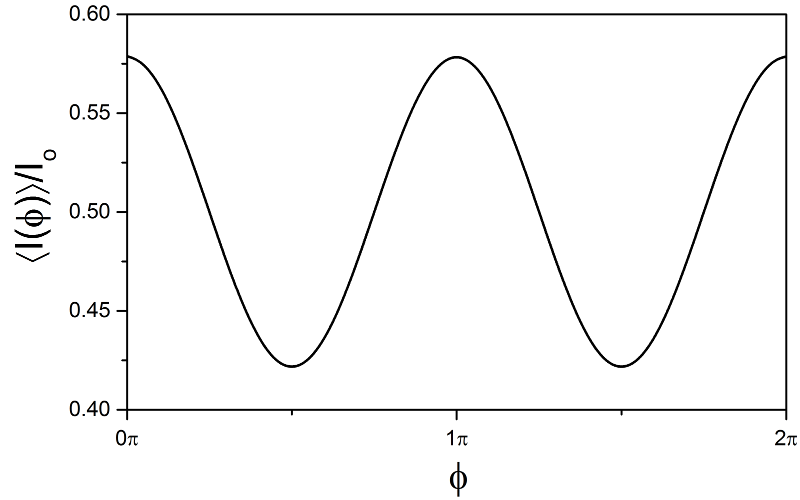

Figure B.4: Plot of $\langle I(\phi)\rangle$ for the case where $A = \lambda$. Only at certain values of ϕ does $\langle I(\phi)\rangle = I_0/2$.

Triangle Wave Excitation

A triangle wave is a better choice than a sine wave since the PDF of a triangle wave is a constant value. This means that an equal weight will be applied to all values of $\langle I\rangle$. We can define a triangle wave in the following way:

$$x(t) = \begin{cases} A\left(\frac{2\omega}{\pi}t - 1\right) & 0 \le t < \frac{\pi}{\omega} \\ A\left(3 - \frac{2\omega}{\pi}t\right) & \frac{\pi}{\omega} \le t < \frac{2\pi}{\omega} \end{cases} \tag{B.4}$$

where A is the amplitude and $2\pi/\omega$ is the period of the triangle wave. Using the same method as before, we can substitute $x(t)$ in for $I(x) = I_0\cos^2[kx + \phi]$ and take the time average. Substitution of variables gives us the following equation:

$$\langle I\rangle = \int_{-A}^{A} \frac{I_0\cos^2[kx+\phi]}{2A}dx = \frac{I_0}{2}\left(1 + \frac{\sin[2kA]}{2kA}\cos[2\phi]\right) \tag{B.5}$$

Again, the maximum deviation from $\langle I\rangle = I_0/2$ is when $\cos[2\phi] = \pm 1$. This solution is better than the one we obtained for a sine wave since $\frac{\sin[2kA]}{2kA}$ converges

to zero much faster than $J_0[2kA]$ (see figure B.5).

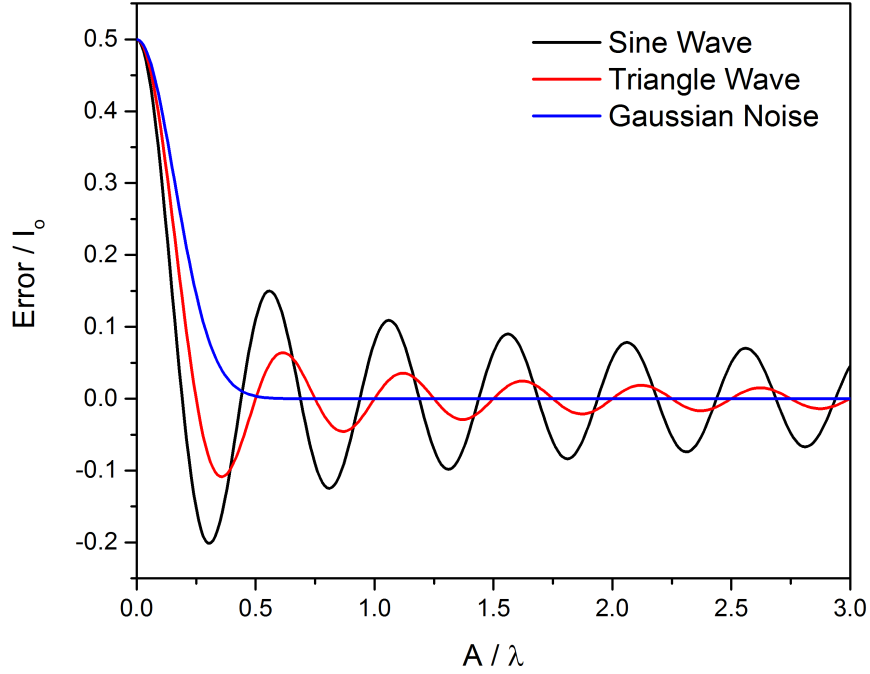

Figure B.5: Plot of the maximum error ($\langle I(\phi)\rangle - I_0/2$) for three different waveforms. A has been normalized by the wavelength of the laser.

Gaussian Noise Excitation

Finally, we look at the case where the speaker is driven using Gaussian noise. The PDF of a Gaussian noise source centered at $x = 0$ is:

$$P_G(x) = \frac{\exp[-\frac{x^2}{2A^2}]}{A\sqrt{2\pi}} \tag{B.6}$$

where A is the standard deviation. Therefore, the time-averaged intensity will be:

$$\langle I\rangle = \int_{-\infty}^{\infty} I_0 \cos^2[kx+\phi]\frac{\exp[-\frac{x^2}{2A^2}]}{A\sqrt{2\pi}}dx = \frac{I_0}{2}\left(1+\exp\left[-\frac{(2kA)^2}{2}\right]\cos[2\phi]\right) \tag{B.7}$$

We can plot $\langle I \rangle$ as a function of A for all three cases. Figure B.5 shows the maximum error ($\phi = 0$) verses A, where A has been normalized by the laser wavelength, λ.

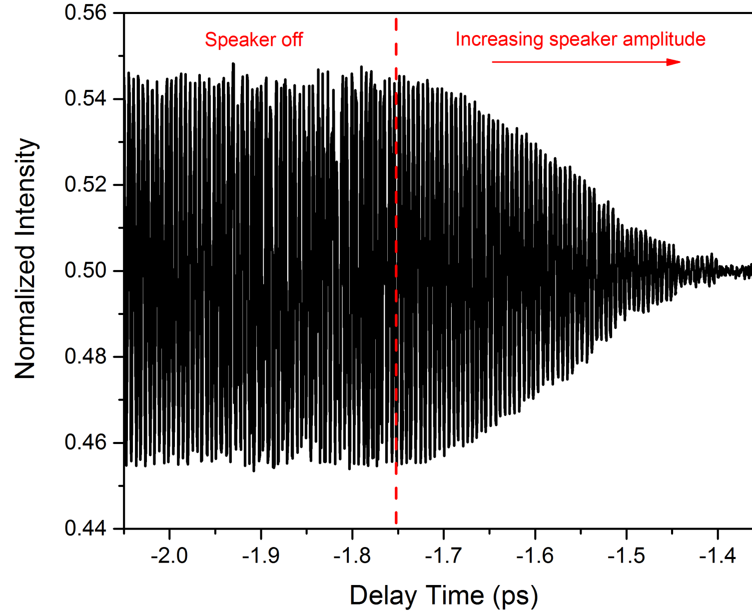

Figure B.6: Plot of interference fringes from moving the delay line at a constant speed with the speaker system off (left) and playing Gaussian noise at an increasing volume (right)

B.1.3 Results

To test the speaker system, we played Gaussian noise while slowly moving the delay line at a constant speed and measured the interference fringes. As you can see from figure B.6, fringes are clearly visible when the speaker is off and disappear as the volume is increased. The integration time for the lock-in was long enough to average over many cycles of the speaker, but short enough to resolve the fringes from the delay line movement.

B.1.4 Conclusion

We have presented a simple and inexpensive way to remove the interference artifact from an ultrafast delay line with a mirror and speaker. It was found that the ideal waveform for minimizing interference fringes is Gaussian noise. Finally, we presented experimental verification that our system functions as expected.

Appendix C

Classical Derivation of the Nonlinear Susceptibility for a Centrosymmetric Material[1]

It is possible to derive a very good approximation of the linear response of a non-metallic material using a damped, driven simple harmonic oscillator model. In this model, one uses the following equation of motion for a bound electron experiencing a driving force [173]:

$$\ddot{\widetilde{\mathbf{x}}} + 2\gamma\dot{\widetilde{\mathbf{x}}} + \omega_0^2\widetilde{\mathbf{x}} = -\frac{e\widetilde{\mathbf{E}}(t)}{m} \tag{C.1}$$

where x is the displacement of the electron, γ is a damping term, ω_0^2 is the resonance frequency of the atom, and m is the electron mass. We have taken the restoring force acting on the electron to be linear in this case:

$$\widetilde{\mathbf{F}}_{\text{restoring}} = -m\omega_0^2\widetilde{\mathbf{x}} \tag{C.2}$$

[1] **This derivation closely follows that of [153], pages 28–32.**

In order to account for the nonlinear response of the medium, we retain higher order terms in the Taylor expansion of the restoring force:

$$\widetilde{\mathbf{F}}_{\text{restoring}} = -m\omega_0^2\widetilde{\mathbf{x}} - ma\widetilde{\mathbf{x}}^2 + mb(\widetilde{\mathbf{x}}\cdot\widetilde{\mathbf{x}})\widetilde{\mathbf{x}} \tag{C.3}$$

where a and b are parameters that characterize the strength of the second- and third-order nonlinearity respectively. We can integrate the restoring force to obtain the potential energy as a function of position:

$$U(\widetilde{x}) = -\int \widetilde{F}_{\text{restoring}} d\widetilde{x} = \frac{1}{2}m\omega_0^2\widetilde{x}^2 + \frac{1}{3}ma\widetilde{x}^3 - \frac{1}{4}mb\widetilde{x}^4 \tag{C.4}$$

By definition, the potential energy is a symmetric function of position (*i.e.* $U(\widetilde{\mathbf{x}}) = U(-\widetilde{\mathbf{x}})$) for centrosymmetric materials like BP. Therefore, $a = 0$ and the equation of motion becomes:

$$\ddot{\widetilde{\mathbf{x}}} + 2\gamma\dot{\widetilde{\mathbf{x}}} + \omega_0^2\widetilde{\mathbf{x}} - mb(\widetilde{\mathbf{x}}\cdot\widetilde{\mathbf{x}})\widetilde{\mathbf{x}} = -\frac{e\widetilde{\mathbf{E}}(t)}{m} \tag{C.5}$$

We assume that the driving field has the following form:

$$\widetilde{\mathbf{E}}(t) = \mathbf{E_1}e^{-i\omega_1 t} + \mathbf{E_2}e^{-i\omega_2 t} + \mathbf{E_3}e^{-i\omega_3 t} + \text{c.c.} \tag{C.6}$$

This is the most general case for a third-order nonlinear process, but for THG $\omega_1 = \omega_2 = \omega_3$. To simplify the notation, we can rewrite equation C.6 as:

$$\widetilde{\mathbf{E}}(t) = \sum_n \mathbf{E}(\omega_n)e^{-i\omega_n t} \tag{C.7}$$

There is no general solution to equation C.5 using this driving field, but if the electron displacement is such that $b(\widetilde{\mathbf{x}}\cdot\widetilde{\mathbf{x}})\widetilde{\mathbf{x}} \ll \omega_0^2\widetilde{\mathbf{x}}$ (*i.e.* the driving field is sufficiently weak), we can use perturbation theory to solve this differential equation. $\widetilde{\mathbf{E}}(t)$ is replaced by $\lambda\widetilde{\mathbf{E}}(t)$ in equation C.5 and $\lambda \in (0, 1]$ is a parameter that characterizes

the strength of the perturbation. We now can find a solution that is a power series expansion of λ:

$$\widetilde{\mathbf{x}} = \lambda\widetilde{\mathbf{x}}^{(1)} + \lambda^2\widetilde{\mathbf{x}}^{(2)} + \lambda^3\widetilde{\mathbf{x}}^{(3)} + ... \tag{C.8}$$

If the solution is to be correct for all values of λ, each term proportional to λ^n must vanish separately. Substituting C.8 into C.5 and organizing by like terms, we get the following:

$$\ddot{\widetilde{\mathbf{x}}}^{(1)} + 2\gamma\dot{\widetilde{\mathbf{x}}}^{(1)} + \omega_0^2\widetilde{\mathbf{x}}^{(1)} = -\frac{e\widetilde{\mathbf{E}}(t)}{m} \tag{C.9}$$

$$\ddot{\widetilde{\mathbf{x}}}^{(2)} + 2\gamma\dot{\widetilde{\mathbf{x}}}^{(2)} + \omega_0^2\widetilde{\mathbf{x}}^{(2)} = 0 \tag{C.10}$$

$$\ddot{\widetilde{\mathbf{x}}}^{(3)} + 2\gamma\dot{\widetilde{\mathbf{x}}}^{(3)} + \omega_0^2\widetilde{\mathbf{x}}^{(3)} - b(\widetilde{\mathbf{x}}^{(1)} \cdot \widetilde{\mathbf{x}}^{(1)})\widetilde{\mathbf{x}}^{(1)} = 0 \tag{C.11}$$

The solution to C.9 is simply that of a damped simple harmonic oscillator with multiple resonances. We can write the solution in the following way:

$$\widetilde{\mathbf{x}}^{(1)}(t) = \sum_n \mathbf{x}^{(1)}(\omega_n)e^{-i\omega_n t} \tag{C.12}$$

where

$$\mathbf{x}^{(1)}(\omega_n) = -\frac{eE(\omega_n)/m}{D(\omega_n)} \tag{C.13}$$

We have defined $D(\omega_n)$ as $D(\omega_n) = \omega_0^2 - \omega_n^2 - 2i\omega_n\gamma$. Since the polarization is the dipole moment per volume, we can use our solution to find the linear susceptibility:

$$P^{(1)}(\omega_n) = -Nex^{(1)}(\omega_n) = \epsilon_0\chi^{(1)}(\omega_n)E(\omega_n) \tag{C.14}$$

where N is the electron number density. This assumed an isotropic material so everything is a scalar. We can solve for $\chi^{(1)}(\omega_n)$ and get the following relation:

$$\chi^{(1)}(\omega_n) = \frac{Ne^2/m}{\epsilon_0 D(\omega_n)} \tag{C.15}$$

Equation C.10 describes the second order response of our material. Here we have an equation that describes a damped, undriven simple harmonic oscillator. Because there is no driving force, the solution to C.10 is simply:

$$\mathbf{x}^{(2)} = 0 \tag{C.16}$$

This means that there is no second-order, bulk response in centrosymmetric materials and therefore, no SHG. Moving on to equation C.11, we can substitute our solution for $\widetilde{\mathbf{x}}^{(1)}(t)$ from equation C.12 into C.11:

$$\ddot{\widetilde{\mathbf{x}}}^{(3)} + 2\gamma\dot{\widetilde{\mathbf{x}}}^{(3)} + \omega_0^2\widetilde{\mathbf{x}}^{(3)} = -\sum_{mnp} \frac{be^3[\mathbf{E}(\omega_m)\cdot\mathbf{E}(\omega_n)]\mathbf{E}(\omega_p)}{m^3 D(\omega_m)D(\omega_n)D(\omega_p)} e^{-i(\omega_m+\omega_n+\omega_p)t} \tag{C.17}$$

Since we have cubed a sum of three different frequencies, we have many possible cross terms and need to sum over m, n, and p. These cross terms account for various third-order processes such as four-wave mixing, intensity dependent refractive index (*i.e.* the Kerr effect), and THG. Like before, the solution to C.17 can be written as:

$$\widetilde{\mathbf{x}}^{(3)}(t) = \sum_q \mathbf{x}^{(3)}(\omega_q)e^{-i\omega_q t} \tag{C.18}$$

where $\omega_q = \omega_m + \omega_n + \omega_p$, which is the driving frequency. If we substitute this into equation C.17, we get the following:

$$(\omega_0^2 - \omega_q^2 - 2i\omega_q\gamma)\widetilde{\mathbf{x}}^{(3)}(t) = -\sum_{mnp} \frac{be^3[\mathbf{E}(\omega_m)\cdot\mathbf{E}(\omega_n)]\mathbf{E}(\omega_p)}{m^3 D(\omega_m)D(\omega_n)D(\omega_p)} e^{-i(\omega_m+\omega_n+\omega_p)t}$$

$$D(\omega_q)\sum_q \mathbf{x}^{(3)}(\omega_q)e^{-i\omega_q t} = -\sum_{mnp} \frac{be^3[\mathbf{E}(\omega_m)\cdot\mathbf{E}(\omega_n)]\mathbf{E}(\omega_p)}{m^3 D(\omega_m)D(\omega_n)D(\omega_p)} e^{-i(\omega_m+\omega_n+\omega_p)t} \tag{C.19}$$

The only way for equation C.19 to hold true for all t is to require $\omega_q = \omega_m + \omega_n + \omega_p$. We denote this by using a contracted summation "(mnp)" and solve for $\mathbf{x}^{(3)}$:

$$\mathbf{x}^{(3)}(\omega_q) = -\sum_{(mnp)} \frac{be^3[\mathbf{E}(\omega_m)\cdot\mathbf{E}(\omega_n)]\mathbf{E}(\omega_p)}{m^3 D(\omega_m)D(\omega_n)D(\omega_p)D(\omega_q)} \tag{C.20}$$

In analogy to the linear polarization, the third-order polarization is proportional to the higher-order dipole moment $\mathbf{x}^{(3)}$:

$$\mathbf{P}^{(3)}(\omega_q) = -Ne\mathbf{x}^{(3)}(\omega_q) = \sum_{(mnp)} \frac{Nbe^4[\mathbf{E}(\omega_m) \cdot \mathbf{E}(\omega_n)]\mathbf{E}(\omega_p)}{m^3 D(\omega_m)D(\omega_n)D(\omega_p)D(\omega_q)} \tag{C.21}$$

As defined in [153], the nonlinear polarization is related to the third-order susceptibility in the following way:

$$P_i^{(3)}(\omega_q) = \epsilon_0 \sum_{jkl} \sum_{(mnp)} \chi_{ijkl}^{(3)}(\omega_q, \omega_m, \omega_n, \omega_p) E_j(\omega_m) E_k(\omega_n) E_l(\omega_p) \tag{C.22}$$

where i, j, k, and l are indices for the x, y, and z directions in a Cartesian coordinate system. If we break up equations C.20 and C.21 into individual Cartesian components, we can rewrite the dot product of $\mathbf{E}(\omega_m) \cdot \mathbf{E}(\omega_n)$ to be $\sum_{jk} E_j(\omega_m) E_k(\omega_n) \delta_{jk}$ and rewrite the equations as follows:

$$\begin{aligned}
x_l^{(3)}(\omega_q) &= -\sum_{jk} \sum_{(mnp)} \frac{be^3 E_j(\omega_m) E_k(\omega_n) E_l(\omega_p)}{m^3 D(\omega_m)D(\omega_n)D(\omega_p)D(\omega_q)} \delta_{jk} \\
P_i^{(3)}(\omega_q) &= -\sum_l Nex_l^{(3)}(\omega_q)\delta_{il} \\
P_i^{(3)}(\omega_q) &= \sum_{jkl} \sum_{(mnp)} \frac{Nbe^4 \delta_{il}\delta_{jk}}{\epsilon_0 m^3 D(\omega_m)D(\omega_n)D(\omega_p)D(\omega_q)} E_j(\omega_m) E_k(\omega_n) E_l(\omega_p)
\end{aligned}$$

By simple comparison with C.22, we can solve for $\chi_{ijkl}^{(3)}$:

$$\chi_{ijkl}^{(3)}(\omega_q, \omega_m, \omega_n, \omega_p) = \frac{Nbe^4 \delta_{il}\delta_{jk}}{\epsilon_0 m^3 D(\omega_m)D(\omega_n)D(\omega_p)D(\omega_q)} \tag{C.23}$$

Since it does not matter which order in which we define E_j, E_k, and E_l in equation C.21, we can take this six-fold degeneracy into account by dividing by six. Summing over all possible combinations of j, k, and l, we get the following:

$$\chi_{ijkl}^{(3)}(\omega_q, \omega_m, \omega_n, \omega_p) = \frac{Nbe^4[\delta_{ij}\delta_{kl} + \delta_{ik}\delta_{jl} + \delta_{il}\delta_{jk}]}{3\epsilon_0 m^3 D(\omega_m)D(\omega_n)D(\omega_p)D(\omega_q)} \tag{C.24}$$

As a final step, we can write $\chi^{(3)}$ in terms of $\chi^{(1)}$ at each of the four frequencies:

$$\chi^{(3)}_{ijkl}(\omega_q, \omega_m, \omega_n, \omega_p) = \frac{b\epsilon_0^3 m}{3N^3 e^4}[\chi^{(1)}(\omega_q)\chi^{(1)}(\omega_m)\chi^{(1)}(\omega_n)\chi^{(1)}(\omega_p)] \times [\delta_{ij}\delta_{kl} + \delta_{ik}\delta_{jl} + \delta_{il}\delta_{jk}] \tag{C.25}$$